2015

EVAPORATION-INDUCED FORMATION OF WELL-ORDERED SURFACE PATTERNS ON POLYMER FILMS

Wei Sun
University of Kentucky, andydirk1@gmail.com

STUDENT AGREEMENT:

I represent that my thesis or dissertation and abstract are my original work. Proper attribution has been given to all outside sources. I understand that I am solely responsible for obtaining any needed copyright permissions. I have obtained needed written permission statement(s) from the owner(s) of each third-party copyrighted matter to be included in my work, allowing electronic distribution (if such use is not permitted by the fair use doctrine) which will be submitted to UKnowledge as Additional File.

I hereby grant to The University of Kentucky and its agents the irrevocable, non-exclusive, and royalty-free license to archive and make accessible my work in whole or in part in all forms of media, now or hereafter known. I agree that the document mentioned above may be made available immediately for worldwide access unless an embargo applies.

I retain all other ownership rights to the copyright of my work. I also retain the right to use in future works (such as articles or books) all or part of my work. I understand that I am free to register the copyright to my work.

REVIEW, APPROVAL AND ACCEPTANCE

The document mentioned above has been reviewed and accepted by the student's advisor, on behalf of the advisory committee, and by the Director of Graduate Studies (DGS), on behalf of the program; we verify that this is the final, approved version of the student's thesis including all changes required by the advisory committee. The undersigned agree to abide by the statements above.

Wei Sun, Student

Dr. Fuqian Yang, Major Professor

Dr. Thomas Dziubla, Director of Graduate Studies

EVAPORATION-INDUCED FORMATION OF WELL-ORDERED SURFACE PATTERNS ON POLYMER FILMS

DISSERTATION

A dissertation submitted in partial fulfillment of the
Requirements for the degree of Doctor of Philosophy in the
College of Engineering
at the University of Kentucky

By
Wei Sun

Lexington, Kentucky

Director: Dr. Fuqian Yang, Professor of Materials Engineering
University of Kentucky, Lexington, Kentucky

2015

ABSTRACT OF DISSERTATION

EVAPORATION-INDUCED FORMATION OF WELL-ORDERED SURFACE PATTERNS ON POLYMER FILMS

Various techniques of fabricating surface patterns of small scales have been widely studied due to the potential applications of surface patterns in a variety of areas. It is a challenge to fabricate well-ordered surface area efficiently and economically. Evaporation-induced surface patterning is a promising approach to fabricate well-ordered surface patterns over a large area at low cost. In this study, the evaporation-induced surface patterns with controllable geometrical characteristics have been constructed. The dewetting kinetics on deformable substrate is also investigated.

Using simple templates to control the geometry and the evaporation behavior of a droplet of volatile solvent, various gradient surface patterns, such as concentric rings, multiple straight stripes formed with a straight copper wire, etc. have been constructed on PMMA films. The wavelength and amplitude are found to decreases with the decrease of the distance to the objects used in templates. There is also a nearly linear relation between the amplitude and wavelength. The effects of several experimental parameters on the geometrical characteristics of the surface structures are studied, i.e. dimensions of the template, film thickness (solution concentration), substrate temperature, etc. The wavelength and amplitude increase with the increase of the film thickness (solution concentration), with the increase of the dimension of the template. However with the increase of the substrate temperature, the wavelength increases, while the amplitude decrease. Hexagonal network in pre-cast PMMA film have been fabricated by a “breath figure” approach at low humidity and low substrate temperature. The dimensions of the hexagonal holes are dependent on the template size and film thickness.

The kinetics of the evaporative dewetting of a liquid (toluene) film on a deformable substrate (PMMA film) with the confinement of a circular copper ring is also studied. The

liquid film first dewets from the outside towards the copper ring. When a critical volume is reached, an internal contact line appears, which dewets from the center to the copper ring smoothly with a constant velocity, then switches to a “stick-slip” motion. The average velocity of the smooth motion increases with the increase of the copper ring size and film thickness.

KEYWORDS: Evaporation, Thin film, Self-assembly, Polymer, Dewetting

Wei Sun

12/09/2015

EVAPORATION-INDUCED FORMATION OF WELL-ORDERED SURFACE PATTERNS ON POLYMER FILMS

By

Wei Sun

Dr. Fuqian Yang

Director of Dissertation

Dr. Thomas Dziubla

Director of Graduate Studies

12/09/2015

Dedicated to my grandparents, parents and wife

ACKNOWLEDGEMENTS

Firstly, I would like to express my sincere gratitude to my advisor Dr. Fuqian Yang for his continuous support of my Ph.D. study and related research, for his patience, motivation, immense knowledge and friendship during my doctoral study.

Besides my advisor, I would like to thank the rest of my academic committee: Dr. Thomas John Balk, Dr. Beth Guiton and Dr. Thomas Dziubla, for their time, efforts and suggestions for my research work.

My sincere thanks also goes to Dr. Stephen M Lipka who provided me an opportunity to work in his group and who gave access to the laboratory and research facilities in the last year.

I would like to thank my instructors: Dr. Yang-Tse Cheng, Dr. Bruce J. Hinds, Dr. Richard E Eitel for their teachings and high quality scholarships.

I would like to Bruce Cole, Chelsea Hansing, and Nancy Miller for their assistant during my doctoral study.

I also would like to thank my lab mates: Guangfeng Zhao, Ming Liu, Yunfei Jia, Yuan Sun, Liping Bian and Ruiting Zhao, for their help and support on my research and life.

Last but not the least, I would like to thank my family: my parents and wife for supporting me spiritually throughout my doctoral study and my life in general.

Table of Contents

ACKNOWLEDGEMENTS iii
List of Figures viii
Chapter 1. Introduction 1
Chapter 2. Literature Review 4
2.1 Surface patterns 4
2.2 Techniques of fabrication of surface patterns 4
2.2.1 Polymer demixing 4
2.2.2 Nanoimprint 6
2.2.3 Surface wrinkling/buckling 7
2.2.4 Fracture-induced structuring (FIS) 8
2.3 Evaporation-induced surface pattern 10
2.3.1 Coffee ring 10
2.3.2 Regular coffee-ring patterns 13
2.3.3 Mechanisms for coffee ring 20
2.4 Fingering instability 23
2.5 Breath figure 24
2.5.1 Traditional “breath figure” approaches 25
2.5.2 Novel “breath figure” approaches 25
2.6 Kinetics of the dewetting of liquid film 27
2.6.1 Wetting 27

2.6.2 Dewetting 28

Chapter 3. Evaporation-induced formation of self-organized gradient concentric rings on sub-micron pre-cast PMMA films 32

3.1 Introduction 32

3.2 Dimensional analysis 34

3.3 Experimental details 35

3.4 Results 37

3.5 Summary 42

3.6 Supporting Information 48

Chapter 4. Formation of self-organized gradient stripes on pre-cast PMMA films 53

4.1 Introduction 53

4.2 Experimental details 55

4.3 Results 57

4.4 Discussions 61

4.5 Conclusion 67

Chapter 5. Self-organization of unconventional gradient concentric rings with a circular ring as template 74

5.1 Evaporating a pure solvent droplet on a pre-cast film 74

5.1.1 Introduction 74

5.1.2 Experimental section 76

5.1.3 Results and discussion 77

5.1.4 Conclusion 85

5.2 Evaporating a droplet of polymer solution on a glass substrate 91

5.2.1 Introduction.....91

5.2.2 Experimental details.....93

5.2.3 Results and discussion 94

5.2.4 Conclusion 107

Chapter 6. Formation of well-ordered finger-like structures on pre-cast thin films.....116

6.1 Introduction.....116

6.2 Experimental section.....118

6.2.1 Results and Discussions.....119

6.3 Conclusion 124

Chapter 7. Cooling-induced formation of honeycomb patterns on pre-cast PMMA films at low temperatures 130

7.1 Introduction.....130

7.2 Experimental detail 131

7.3 Results.....133

7.4 Discussion 137

7.5 Conclusion 143

Chapter 8. Dynamics of the evaporative dewetting of a volatile liquid film confined within a circular ring.....154

8.1 Introduction.....154

8.2 Experimental.....156

8.3 Results.....158

8.4 Discussion 165

8.5 Conclusion 169

Chapter 9. Summary 177

9.1 Conclusion 177

9.2 Future work 180

9.2.1 Fabrication of evaporation-induced patterns with non-volatile materials ..180

9.2.2 Development of new templates 181

9.2.3 Formation mechanisms of surface paterns 181

9.2.4 Applications of the surface patterns 181

References 183

Vita 206

List of Figures

Figure 3.1 Schematic of the evaporation of a toluene droplet via a "particle-on-film" template and the formation of gradient concentric PMMA rings on a pre-cast PMMA film 43

Figure 3.2 Optical images of the evaporation–induced surface patterns: (a) surface pattern with a particle in the drop (film thickness: 135 nm; average particle diameter: 160 ± 29μm), and (b) surface pattern without a particle in the drop (film thickness: 135 nm) 44

Figure 3.3 (a) AFM image of the concentric rings over an area of 40×40 μm2, and (b) surface profile of the concentric rings (film thickness: 135 nm; average particle diameter: 160 ± 29μm)..... 44

Figure 3.4 (a) Variation of the wavelength of smooth concentric rings with the distance to the particle center for four different particle sizes; (b) Variation of the wavelength of smooth concentric rings with the distance to the particle surface for four different particle sizes (film thickness: 135 nm) 45

Figure 3.5 Correlation between the wavelength and the amplitude of smooth concentric rings for four different particle sizes (film thickness: 135 nm)..... 46

Figure 3.6 Dependence of the slope of the amplitude verse the wavelength on the particle size (film thickness: 135 nm)..... 46

Figure 3.7 Variation of the wavelength of smooth concentric rings with the distance to the particle center for four film thicknesses (average particle diameter: 160 ± 29μm)..... 47

Figure 3.8 Correlation between the wavelength and the amplitude of smooth

concentric rings for four film thicknesses (average particle diameter: 160 ± 29μm) 47

Figure 3.9 Dependence of the slope of the amplitude verse the wavelength on film thickness (average particle diameter: 160 ± 29μm) 48

Figure 3.10 Variation of the drop radius with evaporation time during a toluene drop evaporating on a PMMA film with a particle in the drop (film thickness: 135 nm; average particle diameter: 160 ± 29μm). 49

Figure 3.11 Schematic of the external forces exerted on contact line during stick-slip motion 49

Figure 4.1 Optical images of the evaporation–induced surface patterns; (a) surface pattern formed *vis* a single copper wire, and (b) enlarged view of the surface pattern in the enclosed area in (a) (film thickness: 90 nm; diameter of the copper wire: 79 μm)..... 69

Figure 4.2 (a) An AFM image of the parallel stripes over an area of 40×40 μm^2, and (b) surface profile of the parallel stripes (film thickness: 90 nm; copper wire diameter 79 μm)..... 69

Figure 4.3 Variation of the wavelength of the smooth stripes formed *via* a single copper wire with the distance to the copper wire center for three copper wire diameters (film thickness: 90 nm)..... 70

Figure 4.4 Correlation of the spatial wavelength and the amplitude of the smooth stripes formed *via* a single copper wire for three copper wire diameters (film thickness: 90 nm) 70

Figure 4.5 Variation of the slope of amplitude verse wavelength of smooth stripes

(formed *via* a single copper wire) with film thickness for three wire diameters 71

Figure 4.6 (a) Optical images of the evaporation–induced surface patterns formed *via* two parallel copper wires (Inset: enlarged view of the pattern in the rectangular box), and (b) surface patterns far away from the copper wires (film thickness: 90 nm; diameter of the copper wire: 79 mm) 71

Figure 4.7 (a) Variation of the wavelength of smooth stripes with the distance to individual copper wire centers, and (b) correlation of the amplitude and the wavelength of the smooth stripes formed *via* two copper wires (diameter of the copper wires: 79 μm; distance between two copper wire centers: 1.7 mm; film thickness: 90 nm) 72

Figure 4.8 Variation of the slope of amplitude verse wavelength with the distance between two copper wires for three copper wires (film thickness: 90 nm)..... 72

Figure 4.9 Variation of the size of the featureless zone with the distance between two copper wire centers (film thickness: 90 nm)..... 73

Figure 5.1 Optical images of the evaporation–induced gradient concentric rings on a pre-cast PMMA film (film thickness: 140 nm; diameter of the copper ring: 1425 μm); (a) a large view of the surface pattern, (b) an enlarged view of the surface pattern in the enclosed area in (a), (c) the concentric rings outside the copper ring, and (d) the concentric rings inside the copper ring..... 86

Figure 5.2 AFM images and line scans of the concentric rings nearest to a copper ring over an area of 40×40 μm^2 (film thickness: 140 nm; diameter of the copper ring: 2360 μm); (a) the PMMA rings inside the copper ring, and (b) the PMMA rings

outside the copper ring 87
Figure 5.3 Variation of the wavelength of the gradient concentric rings with the distance to the copper ring for copper rings of different diameters (film thickness: 140 nm). “0” in the x-axis refers to the position of the copper wire, and the negative sign refers the positions outside the copper ring. 88
Figure 5.4 Correlation between the amplitude and the wavelength of the concentric rings formed via a copper ring of 2360 μm in diameter (film thickness: 140 nm) 88
Figure 5.5 Variation of the slope of the amplitude to the wavelength with the size of the copper ring (film thickness: 90 nm) 89
Figure 5.6 Variation of the wavelength with the distance to copper ring (diameter of copper ring: 1425 μm). “0” in the x-axis refers to the position of the copper wire. 89
Figure 5.7 Dependence of the slope of the amplitude to the wavelength of the gradient concentric rings on film thickness (diameter of copper ring: 1425 μm)..... 90
Figure 5.8 Variation of the size of featureless zone with the diameter of copper ring for three film thicknesses 90
Figure 5.9 Typical optical images of the concentric rings formed with a copper ring *via* the evaporation of a PMMA solution droplet (copper ring diameter: 1380 μm, solution concentration: 0.25 wt%, substrate temperature: 21 ℃). (a) a large view of the surface pattern, (b) an enlarged view of the concentric rings near the copper ring formed outside the copper ring, (c) an enlarged view of the concentric rings near the copper ring formed inside the copper ring, and (d) schematic of the

formation of the PMMA rings. 108

Figure 5.10 (a) A typical AFM image of the concentric rings formed inside a copper ring; (b) correlation between the amplitude and the wavelength of the concentric rings formed both inside and outside the copper ring (copper ring diameter: 3750 μm, solution concentration: 0.125 wt%, substrate temperature: 21 ℃) 109

Figure 5.11 Variation of wavelength with the distance to copper ring for both the concentric rings inside and outside the copper ring for different ring diameter (solution concentration: 0.125 wt%PMMA; substrate temperature: 21 ℃)....110

Figure 5.12 Variation of wavelength with the distance to copper ring for four solution concentrations (copper ring diameter: 1380 μm, substrate temperature: 21 ℃) 110

Figure 5.13 Variation of the slope of the amplitude to the wavelength with the solution concentration (substrate temperature: 21 ℃).....111

Figure 5.14 Variation of wavelength with the distance to copper ring for the concentric rings formed at different substrate temperatures (solution concentration: 0.125wt% PMMA; copper ring diameter: 1380 μm) 111

Figure 5.15 Variation of the slope of the amplitude to the wavelength with the substrate temperature (solution concentration: 0.125 wt% PMMA) 112

Figure 5.16 AFM images (5×5 μm^2) of the patterns formed in the trenches between two adjacent rings at different substrate temperatures (solution concentration: 0.125 wt% PMMA, copper ring diameter: 1380 μm): (a-c) 21℃, (d-f) 35℃, (g-i) 55℃; (j-l) patterns in the trenches between two adjacent rings *via* the

evaporation of a pure toluene droplet on a pre-cast PMMA film (film thickness: ~90 nm, copper ring diameter: 1380 μm, substrate temperature: 21 ℃). The scale bars in all the images represent 1μm.....113

Figure 5.17 Variation of the area fraction of the island patterns in the trenches between two polymer ridges with the wavelength of the concentric rings at three substrate temperatures. (solution concentration: 0.125 wt% PMMA, copper ring diameter: 1380 μm).....114

Figure 5.18 Optical images of the patterns formed by evaporating a droplet of PMMA solution in toluene on a glass slide without templates. Solution concentrations: (a) 0.1wt%, (b) 0.25 wt%, (c) 0.125wt% and (d, e) 0.063wt%. Substrate template is 21℃.....114

Figure 5.19 Optical images of the patterns formed by evaporating a droplet of PMMA solution in toluene on a glass slide without templates at different substrate temperatures: (a) 21℃, (b) 35℃ and (C) 55℃. Solution concentration is 0.125wt%. 115

Figure 6.1(a) Schematic of the experimental set-up for constructing finger-like surface patterns, and (b-d) the surface patterns formed in the regions of Ⅰ, Ⅱ and Ⅲ indicated in (a). The inset in (c) is an enlarged view of the patterns enclosed in the red box (film thickness: ca. 90 nm; tilt angle: 2.86°; droplet volume: 5μL) 125

Figure 6.2 (a) Variation of the dimensions of the outmost finger-like pattern with the droplet volume (tilt angle: 2.86°, film thickness: ca. 90nm); (b) Variation of the

dimensions of the outmost finger-like pattern with tilt angle (droplet volume: 5μL, film thickness: ca. 90nm). 126

Figure 6.3(a) Variation of the wavelength with the normalized distance to the finger tip for different droplet volumes(tilt angle: 2.86°,film thickness: ca. 90nm);(b and c) Optical images of the typical multiple arc-ridges formed along the symmetric axis for different droplet volumes of 10μL (b) and 5μL (c)(tilt angle: 2.86°, normalized distance:0.5, film thickness: ca. 90nm) 127

Figure 6.4 (a) Variation of the wavelength with normalized distance for four different tilt angles(droplet volume: 5μL, film thickness: ca. 90 nm); (b) and (c) optical images of the multiple arc-ridges formed along the symmetric axis for two tilt angles of 5.71° (b) and 2.29° (c) (droplet volume: 5μL,normalized distance:0.5) 128

Figure 6.5 Optical images of the “cross” patterns: (a) the “cross” patterns of the same length; (b) the “cross” patterns of different lengths. The inset is an enlarged view of the patterns enclosed in the red box in (b). 128

Figure 6.6 Optical images of the typical surface patterns formed on polystyrene (PS) film (tilt angle: 2.86°, film thickness: ca. 90nm). (a) along the symmetric, normalized distance: 0.25; (b) the transition zone of the arc-segment and the straight line-segment, normalized distance: 0.25. 129

Figure 7.1 (a) Schematic of the experimental setup; (b-d) surface patterns formed in the zones of 1-3 as labeled in Fig. 1a, respectively (film thickness: ~140 nm, the diameter of the copper ring is 1.45 mm, surface temperature of the film at equilibrium: 8 ºC)..... 144

Figure 7.2 Temporal evolution of the temperature of the cooling stage and the surface temperature of a pre-cast PMMA film of ~140 nm thickness 145

Figure 7.3 Surface patterns formed in zone 1 on different PMMA films; (a) ~90 nm in thickness, (b) ~140 nm in thickness and (c) ~290 nm in thickness; (d) size distribution of the holes formed on the PMMA films (surface temperature of the PMMA at equilibrium: ~8 ºC, the diameter of the copper ring is 1.45 mm). Inserted images are the Fast Fourier Transform (FFT) patterns of the corresponding surface patterns. 146

Figure 7.4 Patterns formed in zone 2 on different PMMA films; (a) ~90 nm in thickness, (b) ~140 nm in thickness and (c) ~290 nm in thickness; (d) size distribution of the holes formed on the PMMA films (surface temperature of the films at equilibrium: ~8 ºC, the diameter of the copper ring is 1.45mm). Inserted images are the FFT patterns of the corresponding surface patterns..... 147

Figure 7.5 Surface patterns formed in zone 1 on PMMA films with copper rings of different sizes (a) ~3.75 mm in diameter, (b) ~2.90 mm in diameter, and (c) ~1.45 mm in diameter; (d) size distribution of the holes formed on the PMMA films (film thickness: 290 nm, surface temperature of the PMMA at equilibrium: ~8 ºC) 148

Figure 7.6 Surface patterns formed in zone 1 on PMMA films with copper rings of different sizes (a) ~3.75 mm in diameter, (b) ~2.90 mm in diameter, and (c) ~1.45 mm in diameter; (d) size distribution of the holes formed on the PMMA films (film thickness: 290 nm, surface temperature of the films at equilibrium: ~8 ºC) 149

Figure 7.7 Surface patterns formed in zone 2 on the PMMA films of ~290 nm film thickness at four equilibrium temperatures; (a) -3.5 ºC, (b) ~1.8 ºC, (c) ~6.0 ºC and (d) ~8.0 ºC (copper ring size: 1.45 mm). 150

Figure 7.8 (a) A typical AFM image of the hexagon network formed in zone 2 on a PMMA film of ~90 nm thickness, (b) a line scan of the surface profile corresponding to the line in (a), and (c) variation of the wall height of the hexagon network with the film thickness (surface temperature of the film at equilibrium state: ~8.0 ºC)..... 151

Figure 7.9 Surface patterns formed on a PS film via the evaporation of a toluene droplet: (a) in zone 1, and (b) in zone 2 (film thickness: ~290 nm, equilibrium temperature of the film surface: ~8.0 ºC, diameter of the copper ring: 1.45 mm) 151

Figure 7.10 Schematic illustration of the formation of the breath figure template during the evaporation of a toluene droplet on a cooled PMMA film 152

Figure 7.11 (a) Size variation of the hexagonal unit with the PMMA film thickness, and (b) size variation of the hexagonal unit with the copper ring diameter (film thickness: 290 nm, surface temperature of the film at equilibrium state: ~8.0 ºC). 153

Figure 8.1 (a) Schematic of the cross section of a toluene droplet confined by a copper ring on a PMMA film; (b-c) Optical images of the evaporation–induced gradient concentric rings on a pre-cast PMMA film (film thickness: ~140 nm; diameter of the copper ring: 2560 μm); (b) a large view of the surface pattern, and (c) an enlarged view of the pattern inside the copper ring. 170

Figure 8.2(a) AFM image of the concentric rings over an area of 40×40 μm^2, and (b) surface profile of the concentric rings. (film thickness: ~90 nm; diameter of the copper ring: 2560 μm) 171

Figure 8.3(a) Variation of the size of the featureless zone with the diameter of the copper rings of three wire diameters for the patterns formed on the PMMA films of ~90 nm thickness, and (b) variation of the slope of the linear fitting of the results in (a) with the wire diameter. 172

Figure 8.4 Temporal evolution of the contact line; (a) just before the appearance of the contact line; (b) 1.60 s after the appearance of the contact line; (c) 2.40 s after the appearance of the contact line; (d) 4 s after the appearance of the contact line (the contact line reached the first "stick" state); (e) 5.80 s after the appearance of the contact line. The yellow arrow indicates the contact line (blue circle), and the red arrow indicates the smallest polymer ring (red circle). (Copper ring diameter: 1430 μm; cross-sectional diameter of the copper wire: 79 μm; film thickness: ~250 nm) 173

Figure 8.5 Temporal variation of the radius of the internal contact for four copper ring diameters (diameter of the copper wire: 79 μm; film thickness: ~90 nm). The time for the onset of the internal contact line is referred to as the reference time (0s). 173

Figure 8.6 Variation of the average receding velocity of the contact line with the diameter of copper ring for three wire diameters (film thickness: ~90 nm) ... 174

Figure 8.7 Side-view of the digital images of a toluene droplet confined by a copper ring of 3750 μm in diameter on a ~140 nm PMMA film: (a) a 15μL toluene

droplet confined by a copper ring made of a copper wire of 500 μm in diameter (t=0 s); (b) side-view of the toluene film in (a) after ~70 s, the distance from the contact to the copper wire is 550 μm; (c) a 6μL toluene droplet confined by a copper ring made of a copper wire of 102 μm in diameter (t=0 s); (d) side-view of the toluene film in (c) after ~34 s, the distance from the contact to the copper wire is 550 μm. The nominal contact angle is noted by red lines. The scale bars in all the images represent 1 mm. 174

Figure 8.8 Side-view of the digital images of a toluene droplet confined by a straight copper wire of 25 mm in length and 500 μm in diameter. The distance from the contact line to the copper wire: (a) 1875 μm; (b) 1450 μm; (c) 1180 μm and (d) 715 μm. The nominal contact angle is noted by red line. The scale bars in all the images represent 1 mm. 175

Figure 8.9 Variation of the radius of the internal contact line with time for four film thicknesses (diameter of copper wire: 79 μm; diameter of copper ring: 3750 μm). The time for the onset of the internal contact line is referred to as the reference time (0s). 175

Figure 8.10 Variation of the average receding velocity of the contact line with film thickness for four ring diameters (wire diameter: 79 μm) 176

Chapter 1. Introduction

Surface patterns refer to the structures on the surface of a bulk material or thin film. Well-ordered surface patterns, especially those of micro/nanoscales have potential applications in various areas.[1-3] The goals of fabricating the surface patterns is to enlarge the throughput, tailor the types and dimensional characteristics, reduce the engineering cost, etc. To achieve these goals, various techniques have been developed to fabricate different types of surface patterns, i.e. nanoimprint, polymer demixing, surface wrinkling/buckling, fracture-induced patterning, etc.[4-7]Although regular surface patterns have been fabricated, the techniques have various disadvantages, more or less. For example, the nanoimprint requires high-cost template, polymer demixing is limited to two or more materials and it needs the modes for regular patterns; surface wrinkling is limited in "hard-on-soft" system. It is a challenge to construct ordered surface patterns with controllable characteristics in efficient and economical approaches.

Evaporation-induced patterning is a low-cost method to fabricate surface patterns in a large area, which is mainly based on the "coffee-ring" effect.[8] When a coffee droplet is evaporated on a flat substrate, microflow would be induced from the center of the droplet to the periphery to compensate the loss of mass. The microflow would carry solute towards the contact line, leaving a "coffee ring" at the contact line. The "coffee ring" effect is common for the evaporation of a droplet of polymer solution or a nanoparticle suspension. For some specific cases, the contact line might be pinned for several times during its lifetime. As a result, multiple rings can be constructed. [9]

However the "coffee ring" patterns formed with free evaporation are usually irregular.

When a droplet is confined by some template, the geometry of the droplet as well as the evaporation process can be significantly controlled, and the patterns formed during the evaporation can be different from the case without any confinement. With the assistant of a "sphere-on-flat" template, concentric ring patterns have been constructed with different materials.[10] The concentric rings with wavelength and amplitude gradients are formed as the contact line experiences a series of "stick-lip" motions. Using other types of templates, multiple straight lines and other types of regular patterns also have been formed.[11] There are various experimental parameters determining the dimensional characteristics of the evaporation-induced patterns, i.e. solution concentration, solvent, temperature, solute, etc.

Although regular evaporation-induced patterns have been fabricated with some templates, usually one type of template can only be used to produce one type of surface patterns (i.e. circular rings or straight lines). To make other type of patterns, a new template is needed. Moreover, the template or experimental system is cost. In this work, we developed several simple and cost-saving templates, which can also be flexibly changed to other shapes for the formation of different patterns. The effects of various parameters on the patterns are systematically investigated in order to make the patterns controllable.

Dewetting is a common phenomenon in our daily life. The evaporation-induced patterns are formed as a volatile liquid film or droplet gradually dewets on a substrate. The dewetting is driven by the evaporation of the volatile solvent, which is different from the dewetting induced by thermodynamic instability. Currently, most researches on the evaporative dewetting are mainly focused on the behavior on rigid substrate, while the dewetting on deformable substrates is seldom studied. In this work, we investigated the evaporative dewetting on a deformable substrate. The study on the dewetting of the liquid

film during the formation of the evaporation-induced patterns can help to understand the formation mechanisms of surface patterns.

In this dissertation, Chapter 1 provides the brief background and motivation of the study. Chapter 2 is the literature review, covering the previous works on the techniques for the fabrications of surface patterns, evaporation-induced surface patterns and evaporative dewetting. In Chapter 3, the surface patterns formed with a "particle-on-film" template is studied. Chapter 4 focuses on the fabrication of multiple straight lines with a straight copper wire as template. Chapter 5 investigates the concentric ring patterns with unconventional gradient formed with two different strategies. In Chapter 6, a finger-like pattern with multiple sub-patterns inside is studied. Chapter 7 studies the kinetics of a volatile solvent on a deformable substrate. Chapter 8 is the summary of this dissertation and the future research opportunities.

Chapter 2. Literature Review

2.1 Surface patterns

Ordered surface structures of small scales have the potentials in various areas, including stretchable electronics[1, 12], photonics[2, 5, 13], surface adhesion[14], tissue engineering[15, 16], biosensor and biomedical devices[3, 4, 17]. Various surface structures have been constructed, such as periodic gratings [18-20], worm-like ridges[21], ring or concentric rings[9, 22-25], honeycomb[26] and etc. Also, these patterns can be made from various materials, such as glassy polymer, polymer blends, co-polymer, rubbers and nanoparticles, which lead to good compatibilities to the application environments.

2.2 Techniques of fabrication of surface patterns

2.2.1 Polymer demixing

Polymer demixing has been extensively studied in bulk polymer materials, while it also has been used to produce surface structures in surface coatings and biomaterials. The fabrication of the surface structures via polymer demixing is usually performed by spin-casting process. The patterns on thin film made by polymer demixing are greatly influenced by film thickness, composition of the binary polymer blend, solvent and thermal treatment[27, 28].

PS-PMMA is a well-known immiscible polymer blend whose demixing behavior has been widely studied. Ton-That et al.[29] found pitted patterns with typical pit size of 1.2um and depth of 30-40nm were formed on the spin-cast film, when 50-50 PS-PMMA blend

was applied. They found the pits got shallower and then became distorted after 12-14h, as the thermo-annealing process proceeded, Also an inversion of the components occurred on the surface. The main component on the surface was PMMA for the film prior to annealing due to its higher solubility in chloroform, while the surface was composed of a single PS phase after 14h annealing, because of the relatively lower surface energy of PS.

The characteristic of the substrate and the solvent also have significant influences on the formation of the surface structures induced by polymer demixing. Walheim et al.[7] used different solvents of various solubility parameters as the spin-casting solvent and found the domain of the polymer with high solubility in the selected solvent was lower than that of the polymer with low one This was because the surface tension would keep flat when both of the polymer domains were swollen with solvent, while there was more solvent in the domain of the polymer with high solubility, whose volume would be less after complete drying. The substrate had significant effect on the location of the two component. The polymer with better affinity with the substrate was more likely to locate on the lower layer.

Heterogeneous surface was produced by Dekeyser et al.[30], when the solution of PMMA was spin-coated on dissolved PS substrate. By using different solvents, different structures were formed and the surface components were also different. When chloroform which is PMMA selective was used, small islands were observed and the main surface constituent was PMMA. However the surface component was exclusively PS, when toluene was applied. The inclusion of PMMA on PS was provided by chlorobenzene and both of the components could be found on the top.

Geldhauser et al.[31] used single pulse laser to produce ordered parallel stripe-like structure with surface energy difference, which was served as a template for the polymer demixing

structuring. Due to the different affinities of the polymers in different regions of the pre-structured surface, the ordered parallel polymer structures were formed on the substrate. Minelli et al.[32] produced ordered polymer structures as well as ordered organization of nano-scale object on the micro-contact printed energy-patterned gold surface.

2.2.2 Nanoimprint

Nanoimprint which is a simple, high-throughput, and high-resolution nano-fabrication technique has received intensive attention. This technique was first invented by Chou and his co-workers [33, 34], of which the system consists three components: patterned mold, resist and substrate. The nanoimprint lithography involves two basic steps: 1) the mold with nano-patterns on the surface is impressed into the pre-cast resist, followed by removal of the mold, 2) the residual resist is removed by anisotropic etching process. During the nanoimprint, the temperature should be above the glass transition temperature of the resist, and the temperature, pressure and other parameters could be adjusted, in order to obtain high-quality patterns[33].

Depending on the curing approach of the resist, we have hot nanoimprint, UV nanoimprint and hot-UV nanoimprint[6]. For hot nanoimprint, high temperature and high pressure are required to reduce the viscosity of the resist and compensate the lack of flatness[35]. Thermoplastic polymers such as PMMA are used for the hot nanoimprint, and ideal materials should have relatively low glass transition temperature, low viscosity and enhanced mechanical strength. The choice of parameters should be decided by the thickness of the resist, the depth of the pattern and the properties of the selected polymer[36]. The UV nanoimprint is performed at room temperature, and also could be used at low pressure [37, 38]. The resist precursors are liquid films or droplets, and different resists are

applied for UV nanoimprint, including spin-coating film, coating by droplet dispensing, UV-NIL materials, reverse tone NIL and thermoplastic UV-curable materials[35].

As the development of nanoimprint, the resolution has been improved from sub-25nm[34] to sub-10nm[39, 40], and this technique has been extended to various materials on which high-quality and high throughput structures are difficult fabricated, such as ZnO thin film[41].

2.2.3 Surface wrinkling/buckling

Wrinkling and buckling are very interesting material phenomena, which are widely used to fabricate surface structures on thin film or sheet. The wrinkling or buckling are usually formed in a system composed of a soft matter with a hard skin[42]. Different approaches, such as thermal expansion mismatch, oxidation, diffusion have been developed to produce various surface wrinkling or buckling[43].

Bowden et al.[44] fabricated complex, ordered patterns on metal film based on the thermal expansion mismatch principle. They deposited a thin metal film composed of gold and titanium on thermal expanded PDMS which had been fixed on glass slide. Buckling with uniform 20-50nm occurred after the compressive stress in the metal film was relieved. When the patterned PDMS was removed from the glass slide and heated, the waves disappeared. The waves reformed with the dimensions similar to those formed before, when cooled down again. Various representative structures were observed in different region of the waved metal film. Huck et al.[45] treated some region of the PDMS with UV prior to the deposition of a metal film, and found after the cooling of PDMS, the formed waves locating in the UV-treated region were different from those formed in the region without any treatment. They studied the effect of the duration of exposure to UV on the waves, and found the wavelength of the waves increased with increasing the duration,

while the amplitude decreased. They suggested that this phenomenon might be the result of the change of Yong's modulus and thermal expansion coefficient of the PDMS.

Bowden et al.[46] also fabricated wave-like structures on the surface of PDMS based on the oxidation mechanism. The PDMS was heated and the surface was oxidized in an oxygen plasma, resulting in a thin, stiff silicate layer on the surface. When the PDMS was cooled, the waves with the wavelength ranging from 0.5 to 10 μm were formed due to the relief of the compressive stress. Domains with different patterns were also found in different region of the wave-like patterns. They also found both the wavelength and amplitude could be enlarged by increasing the temperature or increasing the oxidation time.

Zhao et al.[43] fabricated different wrinkles on SMP (shape memory polymer) PS based on the thermal expansion mismatch and shape memory effect, and studied the effect of heating temperature on the wrinkles. Pre-stretched, pre-indented and pre-compressed SMP PS were polished until the surface became flat. Using the wrinkling process as discussed above, due to different shaped histories which have been recorded by the SMP, various kinds of wrinkles were formed: labyrinth-shaped for the untreated PS, stripe-shaped for pre-stretched PS and ring-shaped for the pre-indented PS. Their results also showed significant changes of the wrinkles formed with different heating temperature.

2.2.4 Fracture-induced structuring (FIS)

Fracture- induced structuring is a cost-effective, low-cost technique to produce high throughput ordered surface structures. Pease et al.[18] reported a fracture-based peeling approach to fabricate sub-60-nm half-pitch gratings with large areas from a featureless polymer film and created nonsymmetrical gratings on both two plates with spatial wavelength ranging from 120nm to 200nm, which is solely determined by the film

thickness. They studied several factors that may influence the formation of the grating patterns including temperature, molecular weight, adhesion between film and substrate, and found three main conditions should be met in order to produce the gratings via fracture-based peeling technique: 1) the polymer film should be amorphous, 2) the temperature during peeling should below the glass transition temperature of the film, 3) there should be a good adhesion between the film and the substrate.

Lin et al.[47] used the fracture-induced gratings for the alignment of liquid crystal molecule. They produced periodic gratings on both of the plates, whose spatial wavelength is around 4 times of the film thickness. Besides the similar results to the study of Pease[18], they also found that the uniformity of the featureless film is important to the formation of the grating patterns. The non-uniform film might lead to flower-like patterns. Based on successful alignment of LC, they demonstrated that the fracture-induced grating method is low cost, and is a good alternative for alignment of LC and other molecules.

The fracture-induced structuring method has been extended to cross-linked silicone sheet which is incapable by the method developed by Pease et al.[18]. Cai and Newby[48] fabricated periodic parallel stripes by peeling a UV/ozone oxidized silicone sheet from its bonded substrate. They found the spatial wavelength of the stripes is determined by the blending strain, and the UV/ozone oxidizing time could significantly influence the regularity of the patterns.

Liang et al.[49] use a new tension-fracture method to produce a complementary set of semi-concentric surface ripples from a featureless polymer film sandwiched between two glass slides. They found the spatial wavelength is proportional to the film thickness, and the amplitude of the patterns first increases with the increasing film thickness and then

becomes independent on the film thickness.

2.3 Evaporation-induced surface pattern

Fabrication of surface patterns via the evaporation of solvent, has attracted many researchers for a long time. Various patterns, including concentric rings, gratings and islands have been produced by this technique. Recently, well-ordered and large throughput surface patterns have been produced by controlling the evaporation behavior and conditions. Meanwhile, the motions of the three-phase contact line (CL) such as "stick-slip" [9, 10, 22] and "advancing-receding" [50, 51] have been observed during the evaporation of the drop. Several mechanisms have also been proposed to explain the formation of the typical evaporation-induced patterns.

2.3.1 Coffee ring

Coffee ring is a typical self-organized pattern induced by the evaporation of solvent. When a drop of coffee on a solid substrate evaporates, a brown dense, ring-like pattern would be left along the perimeter[22, 24], which is well known as "coffee ring". The "coffee ring" effect has been observed in most of the researches concerning on the evaporation of droplet, based on which single ring-like pattern, concentric rings and other patterns have been produced along the immediate CL. The coffee rings can be composed of micro- or nano-particles, when the drop is a suspension of these substances, or the rings can be deposits of polymer when a drop of polymer solution is applied.

Deegan et al. [24] observed typical coffee rings in their study, and provided a simple calculation to support the capillary flow which is used to explain the formation of the coffee ring. They suggested that when the contact line is pinned on the substrate, the liquid evaporating from the edge could be replenished by an outward flow which would bring the

solute to the edge. As a result, a coffee ring deposition would form in the vicinity of the contact line. Their model divides the formation of the coffee ring into two steps. The initial deposition with much shorter time than the complete drying is very sensitive to the diverging flux. Near the contact line the initial mass of the ring M[52] is proportional to the volume of the wedge-shaped region of the drop. All this mass was supposed to be entrained in the ring in the time t required for a point at r_t to move to the contact line. At later time, all other mass is gradually brought to the contact line by the outward flow which has a constant rate in order to replenish the constant evaporation flux. The experimental results from a drop of polystyrene well consistent with the calculated results. They also mentioned that some effects may modify this simple theory, such as the shape of the drop, irregularities on the substrate, and thermal or concentration gradient.

The two steps for the formation of a coffee ring was confirmed by Kajiya et al. [53], who successfully visualized the change of the concentration rate during the dying of drop of fluorescent polystyrene by combining fluorescent measurement and lateral profile measurement. In the early stage, a concentrated region was created in the vicinity of the contact line, and the concentration in the center of the drop remained almost constant, which gradually decreased in the later stage due to the outward flow and became very small after the complete drying.

Deegan[22] found coffee ring-like patterns were formed after complete drying of a drop of colloidal suspension of polystyrene microspheres, and various patterns could be gained when the microspheres with different sizes were applied. Concentric rings were formed when the particle size was 0.1μm. When the volume fraction was 1% and 0.063%, well-defined concentric rings were found, while the rings from the drop of 0.063% volume

fraction were less organized and much thinner. The patterns from the drops of 0.25% and 0.13% volume fraction were interconnected rings which were formed while the contact line was moving, in contrast to the formation of separate concentric rings when the contact line was pinned.

Bi[50] produced multiring poly(2-vinylpyridine)(P2VP) deposits by drying a drop of polymer solution in a mixed solvent (2,6-lutidine+water). Adjusting the concentration of the solution or the ratio of the two components of the mixed solvent, different multiring deposits were obtained. Through recording the drying process by wide-field microscope, they observed an unconventional "advancing-receding" motion, rather than "stick-slip" motion of the contact line, which has also been observed in other studies[51, 54, 55]. The ring-like deposits were found to be formed during the advancing motion of the contact line, and the Marangoni flow was used to explain the formation of the multiring deposits and the unconventional motion of the contact line.

Most studies on the fabrication of the surface patterns by the evaporation of drop are based on the evaporation of polymer solution or particle suspension. Evaporating a drop of pure solvent on a dissolving pre-cast film is also a good strategy to fabricate surface pattern. Gonuguntla and Sharma[9] obtained various patterns by drying a pure solvent drop on pre-cast PMMA film, such as complex undulating rings composed of spaghetti-like threads along the contact line and radially fingerlike patterns. The width of the threads and the period of the fingerlike patterns could be controlled by the thickness of the pre-cast film and vapor pressure of the solvent. The "stick-slip" motion of the contact line was also observed, when concentric rings was formed.

2.3.2 Regular coffee-ring patterns

The "coffee-ring" patterns formed with free evaporation of a solution droplet are usually irregular due to the lack of control of the contact line motion. In the last ten years, "template-controlled" evaporation structuring has been developed to fabricate well-ordered surface structures. Various regular surface patterns have been fabricated by evaporating polymer solution or micro/nano-particle suspension droplets with template confinement. In general, the template, solution concentration, solutes and solvents, evaporation temperatures, etc. can significantly affect the formation and dimensional characteristics of the patterns.

2.3.2.1 Template setup

The geometrical characteristics of the "coffee-ring" patterns are dependent on the geometrical structures of templates. A "sphere-on-flat" geometry has been used to fabricate concentric rings of high regularity via the evaporation of solvent and the patterns made from various materials have been obtained, such as homopolymer[23, 56, 57], copolymer[57], polymer blend[58], semi-crystalline polymer[59], metal and metal oxide[10] and carbon nanotube[60].

The "sphere-on-flat" geometry is similar to a spherical lens on a silica surface. When a drop of polymer solution or a drop of suspension of nanoparticle is confined in the geometry, the evaporation of the solvent only occurs at the edge and highly-ordered concentric rings can be formed as a series of "stick-slip" motion of the contact line. For example, concentric rings of MEH-PPV covered a large area: the radius of the largest ring was about 4200μm and the radius of the smallest ring was 2800μm. The center-to-center wavelength and the height gradients can be clearly measured from optical microscopy

images and AFM images. For example, the concentric rings fabricated by evaporating a drop of a toluene solution with a polymer concentration of 0.075mg/ml, the wavelength was 11.5 at 3725μm and 7.6 at 3375μm. At the same distance from the center, both the wavelength and the height of the rings increased with increasing the concentration of the polymer solution. The solvent also played important role in the formation and characteristics of the patterns. The number of the rings is less for relatively fast-evaporated solvent, while wavelength and height of the rings are larger[23].

Byun et al.[61] developed a "wedge-on-flat" template and constructed a series of straight stripes patterns parallel to the contact line. The width, thickness and wavelength of the straight stripes increase with the increase of the distance to the center of the wedge lens. Taking advantage of the patterned chemical selective surface, copolymer was self-assembled into regular patterns of multiple scales.

Li et al.[62] developed a "flow-enabled self-assembly" strategy to fabricate parallel stripes of PS-b-P4VP micelle. A droplet of polymer solution was dried between two nearly parallel-flat silicon plates. The lower substrate was moved by a programmed linear translational stage, and the top substrate was stationary. The lower substrate was in a "stop and move" mode, and the stripes were formed mainly during the "stop" stage. The width and wavelength of the stripes increase with the increase of the "stop time". A transition of the monolayer to coexisting of monolayer/bilayer occurred for the stop time of 1.5s-2s.

Xiao et al.[63] immersed a coverslip inclinedly into a suspension of multi-walled carbon nanotube. As the solvent gradually evaporated, the contact line moved from the top to the bottom in a "stick-slip" mode, resulting in parallel stripes with width and wavelength. Both

the wavelength and width of the stripes increases from the top to the bottom due to the increase of concentration. Various experimental parameters, such as tilt angle, concentration and temperature, determine the dimensional characteristics of the patterns.

A roll-based evaporation-induced patterning has been developed to fabricate parallel stripes in a large area. [64, 65] A cylinder roller and a flat substrate sandwich a solution droplet. With slow movement of the roller, the contact line moves in a "stick-slip" motion, leading to a series of straight stripes which cover a larger area. The width, wavelength and height of the stripes depend on the roller speed and the solution concentration.

2.3.2.2 Non-volatile solute

Surface patterns can be formed from various materials. Li et al. [61] developed a "cylindrical-on-flat" template to fabricate parallel stripes. A droplet of DNA solution was confined between a cylindrical lens and a flat PDMS substrate. The DNA stripes were perpendicular to the contact line, which is different from the patterns formed with similar template. 2D DNA arrays were produced by a transfer printing. Similar results were also reported with the "sphere-on-flat" template. Spoke patterns of DNA were constructed in a relatively large scale. The spokes are along the direction of the contact line motion, which is significantly different from the conventional coffee ring patterns perpendicular to the direction of the contact line motion. The patterns were found to be significantly dependent on the pH value and the temperature. For the solution with a relatively low pH value ~5.8-6.4, the patterns are spoke patterns. The concentric ring patterns are formed for higher pH value ~7.1. This transition of the pattern is related to the denaturation of the DNA molecule. The transition may also occur with the decrease of the evaporation temperature.

Byun et al.[58] fabricated ordered PMMA/PS blend rings by drying a drop of PMMA/PS blend solution confined in a "sphere-on-flat" geometry. After removing the PS phase with selective solvent cyclohexane, trench-pit or randomly distributed pits appeared. They found the molecular weight greatly affected the phase-separated structures. For PS-112K/PMMA-133K blend, a trench was formed in the middle of the blend ring; for PS-112K/PMMA-534K blend, only randomly distributed pits were formed. This might be due to the high viscosity of the blend with higher molecular weight which inhibits the diffusion of the PS phase.

Hong et al.[57] fabricated gradient concentric rings composed of homopolymer PS, homopolymer PMMA and PMMA-b-PS, respectively, by using "sphere-on-flat". They found the homo-PS rings are punch-hole or fingering structures which are different from the well-organized homo-PMMA rings. This is because of the unfavorable interfacial interaction between PS and silicon. The gradient multirings of PMMA-b-PS showed different structures from both of the homo-PS rings and homo-PMMA rings. The fingering structure of the PMMA-b-PS rings was the result of the competition of the favorable interaction between PMMA and silicon and unfavorable interaction between PS and silicon.

Semi-crystalline polymer was also used to form concentric rings by Byun et al. [59]. After complete drying of a drop restricted in a "sphere-on-flat" geometry, well-ordered concentric rings were formed when PEO-600K was used. The formation of the fiber-like structures on the rings was revealed by AFM images, which never appeared on the amorphous polymer rings. For PEO-100K, the rings were not ordered due to small depinning force. The fiber-like structures on the rings transformed to spiral structures after thermal annealing. A high supercooling of PEO generated more depletion zones than a low

supercooling.

The well-ordered surface patterns induced by evaporation-induced approach can be used as templates to fabricate patterns of other materials. Hong et al.[10] used ordered polymer concentric rings as template to fabricate metal and metal oxide rings. They made gradient concentric rings of PMMA on Al or TiO_2 coated silicon substrate by evaporating a drop of PMMA solution confined in the "sphere-on-flat" geometry. The "bare" regions of the Al and TiO_2 was removed by 20wt% potassium hydroxide (KOH) DI water solution for 2min and 5vol% hydrofluoric acid (HF) DI water solution for less than 1min, respectively. Gradient Al and TiO_2 rings were obtained after rinsing off the PMMA by acetone. The concentric ring-like pattern was also used as template to fabricate ordered carbon nanotube patterns[60]. After complete drying of the drop of a carbon nanotube suspension on the patterned surface and the removal of the polymer template by selective solvent, gradient carbon nanotube rings were formed.

2.3.2.3 Solution concentration

The concentration of a polymer solution or suspension of particles plays an important role in the formation and characteristics of the "coffee-ring" patterns.

Yabu and Shimomura[66] fabricated parallel straight stripes by evaporating a droplet of a polymer solution sandwiched between two glass slides. With the computer-controlled motion of a glass slide, the contact line experienced "stick-slip" motion, leading to a series of parallel stripe patterns. Increasing of the solution concentration caused the patterns from dotted lines to perfect straight lines and finally to ladder-like patterns. The distance between two adjacent stripes are found to decreases with the increase of the solution concentration.

Zhang et al.[67] fabricated "coffee-ring" patterns of silver nanoparticles via an inkjet

printing process. The width and height of the straight silver stripes increase with the increase of the concentration of the suspension of the silver nanoparticles. For a low concentration, there were some breakpoints on the stripes, while for a high concentration, the transparency becomes low.

Gradient curve patterns were fabricated by evaporating a suspension of virus particle controlled by two parallel glass plates.[68] At low concentration (0.01-0.07 mg/ml), stripes of monolayer were formed with the width of the stripes linearly increasing with increasing the concentration. At higher TMV concentrations (0.1mg/mL-0.7mg/mL), TMV stripes of multilayer were formed with the height and width of the stripes increasing with the increase of the concentration. When the TMV Concentration was higher than 0.7mg/mL, a continuous TMV film (multilayers) was formed on the glass surface; no clear stripe pattern could be observed

Finger-like structures can usually be found along with the coffee rings when forming surface structures via the evaporation of drop [9, 66, 69]. Yabu and Shimomura[66] used a computer-controlled apparatus to fabricate well-ordered polymer patterns. A ladder pattern was produced, and the ridge of the ladder was considered as a series of interconnected finger-like structures. The solutal Marangoni convection was attributed to the formation of the finger-like structures. Local condensation of the polymer reduced local surface tension of the solution, leading to solution to the region with high concentration. The formed fingers remained on the substrate due to high viscosity. Periodic finger-like structures formed along with the coffee ring were due to the fluctuation of the surface tension at the contact line. The solution flowed from the thinner regions to the thicker regions where the fingers were formed[9].

2.3.2.4 Solvent

Solvent plays very important role in our "template-on-film" system. The solubility of polymer in the solvent and the vapor pressure of the solvent significantly influence the characteristics of the surface patterns. The pre-cast film could be softened or even dissolved by the solvent, the thickness of the softened layer not only depends on the film thickness, but also depends on the solubility of the polymer in the solvent. A better solvent can produce a thicker-softened layer which is flowable. For pre-cast films which are composed of polymer blend, the situation is more complex. The location of the different components in the surface pattern and the surface pattern itself can be altered by different solvents [7, 58] due to the different affinities. The vapor pressure which greatly influences the evaporation rate can affect the motion of the contact line.

2.3.2.5 Temperature

The property of polymer film, evaporation rate, solubility and viscosity of the softened layer are temperature-dependent. Uchiyama et al.[20] prepared a silica-poly (vinylpyrrolidone) (PVP) hybrid film via a temperature-controlled dip-coating process and studied the temperature effect on the formation of the stripe patterns. Parallel stripes perpendicular to the withdrawal direction were formed when the coating temperature was above 40 ℃. Both the height and width of the periodic stripes increased with the increasing coating temperature. They suggested that the formation of the stripes were caused by an upward capillary flow at the meniscus region near the contact line, as the solvent evaporated. The increase of the width and height was attributed to the thermal-assisted motion of the contact line and hydrolysis and condensation. They also found the width and the height of the pattern increased with decreasing withdrawal speed[70]. A solvent with

lower evaporation rate could suppress the capillary flow, leading to a smooth surface.

. Soltman and Subramanian[71] studied inkjet-printed PEDOT/PSS patterns at different temperatures. At high temperature, separated beads aligned as a line. At low temperature, continuous stripes with periodic overflow was observed. At intermediate temperature, uniform beads were formed. Evaporating a droplet of polymer solution on a substrate with different temperatures caused a transition of a spherical-cap geometry to a valley geometry the temperature increased.

2.3.3 Mechanisms for coffee ring

2.3.3.1 Capillary flow toward the contact line for mass balance

When a contact line is pinned or cannot move enough to compensate the mass loss from evaporation, a radially outward capillary flow or stress would help to replenish this mass loss in order to balance local mass. [22, 72] This flow or stress brings solute to the perimeter, which would then deposit in the vicinity of the contact line.

This mechanism has been used to explain the formation of their patterns. Deegan et al.[24], as discussed above, provided a simple two steps theory to explain the formation of coffee rings based on the capillary flow mechanism. They constructed simple relations among the evaporative flux, radius of the drop, time, mass of the solute, contact angle and distance from the center for two stages: initial evaporation and later evaporation and found good agreement between the calculated results and the experimental results.

Adachi et al.[51] derived a relation between the outward capillary flow and the motion of the contact line by formulating a mathematical modal including the surface tension, friction, flux of the evaporation and other parameters. They found the contact line oscillated and the concentric rings were formed as a result of the competition between the friction and the

surface tension.

The formation of the gradient concentric rings based on the “sphere-on-flat” geometry was also explained with the mass conservation. When the droplet is confined in the “sphere-on-flat” geometry, the evaporation only happened at the edge, so the Marangoni flow is suppressed[23]. The concentric rings are formed with the repeated “stick-slip” motion of the contact line which is the result of the competition of the pinning and depinning force. The wavelength and height of the rings is related to the volume loss of the drop. Both the wavelength and height are larger, if the volume loss is larger. The longer distance the contact line travels, the more polymer deposits. The volume loss between two rings is determined by the competition of the pinning and depinning force. Xu et al.[23] suggested that the pinning force is proportional to the length of the contact line, while the depinning force is non-linear, and the imbalance of the linear pinning force and nonlinear depinning force led to a nonlinear volume loss, resulting in gradient concentric rings.

2.3.3.2 Marangoni flow

In Deegan’s work[24] and Lin’s work[23], the Marangoni flow does not affect the formation of the coffee rings. Marangoni flow was suggested to have significantly influence on the formation of the coffee ring pattern in other researches[69, 73, 74].

The Marangoni flow is the flow caused by the gradient of surface tension. The surface tension can be induced by temperature gradient, concentration gradient and other factors. Hu and Larson[73] suggested that the formation of the coffee ring pattern required not only the pinning of the contact line but also the suppression of the Marangoni effect. Both the coffee ring and drop-like pattern which was considered as a reversal pattern to the coffee rings of PMMA particles were formed after the solvent evaporated. The coffee ring pattern

was from the evaporation of water drop, while the drop-like pattern was from octane drop. The temperature gradient-induced Marangoni vortex was clearly observed in evaporating an octane drop, which brought the particles back to the center of the drop, resulting in a drop-like pattern. The strength of the Marangoni flow was described by Marangoni number which is defined as, where Te is the temperature at the edge of the drop, Tc is the temperature at the top of the drop, R is the contact line radius, t_f is the drying time, β is the surface tension-temperature coefficient and μ is the viscosity of the liquid. The weak Marangoni effect in the water drop was reflected from its low Marangoni number which was around 8 (the Marangoni number was predicted around 45800 for an octane drop).

Majumder et al.[69] produced a surface tension gradient in a drop by immersing the drop in a saturated ethanol vapor and a recirculating Marangoni flow brought nanoparticles from the edge back to the center of the drop, resulting in a uniform thin film rather than a coffee ring pattern induced by the evaporation without ethanol vapor. When a drop of water was exposed to the air saturated with ethanol, the surface tension at the edge of the drop was lower due to the higher adsorption of ethanol, and a surface tension was produced. The recirculating Marangoni flow was also clearly observed.

The surface tension gradient and Marangoni flow can also be induced by adjusting the surface tension of solute and solvent. Poulard and Damman[25] studied a PDMS/heptane system, in which PDMS with different surface tension were used. As the evaporation rate of the solvent was larger at the edge than in the center, the ratio of the polymer to the solvent was higher at the edge. For the system, of which the surface tension of PDMS is larger than heptane, the surface tension at the edge was larger, and the outward Marangoni flow induced a rim at the edge. When the surface tension of the solute is smaller than that

of the solvent, drop-like pattern was formed due to the inward Marangoni flow. A uniform film is formed after the evaporation of the solvent, if the surface tension of the solvent and solute are almost the same.

The solutal Marangoni flow is induced by the surface tension gradient from concentration gradient of solution[9]. Bi et al.[50] suggested that the unconventional multirings and repeated "advancing and receding" motion of the contact line is a result of the competition of an outward solute Marangoni flow and an inward Marangoni flow. The concentration gradient can produce a surface tension gradient. The inward Marangoni flow is due to the higher evaporation rate at the edge and the higher evaporation rate of water which likely leads to a lower surface tension at the edge.

2.4 Fingering instability

Fingering instability is a phenomenon occurring in the vicinity of the contact line of two or three phases, when a drop of polymer solution is drying[66], polymer films are under solvent or thermal annealing[75], or a liquid drop is spreading or receding[76]. Many studies on the fingering instability are concerned on the fingering growth and the developed finger-like structures which are closely related to the motion of the contact line[9, 75]. The motion of the contact line and the formation of the finger-like structures can be driven by external force field. For example, a liquid film flowed downward along a tilted plate [77-79] and the spreading of a rotating drop on a horizontal substrate. Melo et al.[80] studied the evolution of the spinning silicon oil drop on a horizontal disk. The drop gradually enlarged and then a bump developed. Small waves developed; the wave amplitude and mean radius of the drop increased while the wavelength remained constant. Finally, fingers were generated. The mechanism of the fingering instability of a drop is the capillary pressure gradient induced

by the modulation of the rim that drive a secondary flow perpendicular to the main flow.

The fingering has also been found in the process of the dewetting of a polymer film. Sharma and Reiter[81] studied the dewetting behavior of a polymer thin film and found that there were four typical stages for the whole dewetting process: rupture of the film; formation of polygonal cellular pattern; transformation of polygon into holes; fingering growth during the expansion of the hole. The fingering instability only appeared and grew longer quickly for the substrate with low wettability. However, for the substrate with high wettability of the film, the fingering instability never appeared even the annealing temperature was high. High viscosity and wettability of polymer usually led to well-developed finger-like structures which would finally became smaller drop[75].

2.5 Breath figure

Honeycomb patterns with long-range order have potential application in various areas, i.e. biomaterials[26, 82, 83], superhydrophobicity[74], optoelectronic devices[84], optical devices[85], photonics[86], catalyst[87], functional fabrication [88], etc. "Breath Figure" [89] is a simple and effective method to fabricate honeycomb patterns. The "breath figure" method usually proceeds in an environment with high humidity. When a droplet of polymer solution in a volatile solvent is evaporated, the temperature of the droplet surface rapidly decrease. The water vapor from the high humidity environment condense onto the droplet surface and arrange as regular mode. The well-ordered water droplets can serve as a template for the formation of porous polymer film. Various materials can be constructed into honeycomb

patterns, i.e. homopolymer[90], block copolymer[83], cross-linked polymer[91], inorganic/organic hybrid[92], small molecules[93].

2.5.1 Traditional "breath figure" approaches

The most typical system for the "breath figure" patterning is a droplet of polymer solution on a flat substrate in an environment with high humidity. Karthaus et al.[90] fabricated regular honeycomb patterns with different materials, i.e. polystyrene-block-polyisoprene copolymer; a mixture of a TiO2 precursor, a low molar weight amphiphilic and polystyrene. Generally, well-ordered honeycomb patterns are formed with all the materials, while the pore shape and size vary with different materials. The humidity also play important role in the control of the pore size.

Xu et al.[94] successfully fabricated honeycomb porous polysulfone (PSF) film by "breath figure" method, and studied different effects on the sizes of the pores. The nearly circular holes arrange as a hexagonal network. The pore size decreases with the increase of the solution concentration and increases with the increase of the molecular weight. With the condensation onto the solution droplet, the water droplets arrange into a block with hexagonal packing mode. A border between two "blocks" when they are pulled over is reflected as local defects of the patterns.

2.5.2 Novel "breath figure" approaches

Cong et al.[95] constructed a high permeable ordered porous membrane on ice with a "breath figure" method. The pore size decreases with the increase of the solution concentrations due to the decrease of the evaporation rate and condensation rate. The BPPO membrane formed on ice surface had a significant higher permeability than that formed on glass with the same conditions. The ice speeded up the condensation and the water/ice

interface helped the water droplets run through the solution film and increase the permeability.

Besides the flat substrate, the “breath figure” membrane can also be constructed on curved substrate. Jiang et al. [96] fabricated Poly (L-lactic acid) (PLLA) membrane with honeycomb patterns on a micropipette with the assistant of dioleoylphosphatidylethanolamine (DOPE) as a surfactant. The pores were found to significant depend on the curvature of the pipette. The pores formed with high curvature were of hexagonal shapes and arrange with long-range order. On the contrary, the pores formed with low curvature were irregular and were randomly dispersed. The size of the pores increases with the decrease of the curvature. The patterns formed with DOPE were more regular than those formed without DOPE. The effect of the curvature on the shape of patterns was more significant for the PLLA-DOPE system.

Besides water droplet, which condenses in high humidity environment, other droplets may also serve as templates for the formation of the honeycomb patterns. Wang et al.[97] add a non-volatile liquid solute into a polymer solution in a volatile solvent. With the fast evaporation of the solvent, the non-volatile liquid solute gradually reaches saturation and condenses into ordered-arranged droplets, which serve as template for the pattern formation. With this approach, honeycomb patterns were constructed in polysulfone, polystyrene, and polyvinylidene fluoride films.

Nashikawa et al.[98] fabricated an amphiphilic polymer film with regular micropores by evaporating a polymer solution on water surface in a high humidity environment. The “breath figure” template assisted the formation of the honeycomb pores on the film. The evaporation time and the pore size increase with the volume of the droplet of the polymer

solution. The area of the film decreases with the increase of sub-phase (water). The pores observed on both sides were not symmetric. The pores formed on the top-side were round holes, while the pores on the bottom-side were hexagonal.

2.6 Kinetics of the dewetting of liquid film

2.6.1 Wetting

Wetting is a phenomenon referring to how a liquid droplet deposits on a solid/liquid substrate. Typically, there are two types of wetting: complete wetting and partial wetting,[99] which can be distinguished by "spreading parameter" S, defined as:

$$S = \gamma_{so} - (\gamma_{sl} + \gamma) \tag{2.1}$$

where $\gamma_{so}$is the surface tension at the air/solid interface, γ_{sl} is the surface tension at the liquid/solid interface and γ is the surface tension at the air/liquid interface. For the complete wetting, the spreading parameter is positive, and the liquid droplet spreads into a nanoscale film with the smallest contact angle (θ) in order to reach the lowest surface energy. For partial wetting, the droplet is not able to complete spread, but keeps a spherical cap geometry on the solid substrate. The case with $\theta<\pi/2$ is called "most wetting", otherwise it is said to be "most non-wetting. The relations between the surface tension and contact angle is usually described by Young's equation:

$$\gamma cos\theta = \gamma_{so} - \gamma_{sl} \tag{2.2}$$

where θ is the contact angle. "Complete non-wetting" is an ideal case, where a droplet remains a perfect spherical shape. Many studies are focusing on the super-hydrophobicity.[100] Through modification or constructing surface patterns,[101-103] the contact angle can be significantly increased to realize super-hydrophobic surface.

When the substrate is deformable liquid, the case is similar but different from that on

rigid solid substrate. A liquid droplet can complete spread on another immiscible liquid substrate into a very thin film, such as an oil film on the sea.[104] For the "partial wetting" case, the liquid droplet forms a lens geometry with two curved surface at both the air/liquid and liquid/liquid interfaces.[105, 106] The relation of the surface tensions and the contact angle is described by Neumann's triangle.[107]

2.6.2 Dewetting

Dewetting can be considered as the opposite phenomenon to wetting, which refers to the rupture of a liquid film and transformation to a droplet or other geometries. Generally, there are two types of dewetting: thermodynamic dewetting and evaporative dewetting. [108]

Thermodynamic dewetting is induced by thermodynamic instability. For a complete wetting system (S>0), the liquid film can stay stable. In contrast, when the spreading parameter is negative, the liquid film tends to retract into a droplet for the film thickness under a critical thickness (e_c). The critical thickness of the liquid film is described by the equation:

$$e_c = 2\kappa^{-1}\sin(\frac{\theta}{2}) \tag{2.3}$$

where κ is the capillary length, θ is the contact angle.

There are many studies on the dewetting of a polymer film on a hostile substrate induced by thermal annealing.[109-111] Reiter[112] studied the dewetting of a thin polystyrene film on a silicon substrate induced by thermal annealing. Two series of experiments were setup. For type A, the polystyrene film was annealed at 166 ℃ for 12h. The polymer film dewet into smaller droplets which distributed as polygonal shapes. For type B, the same sample as used in type A was annealed at temperature between 135-150℃ for 0.5-2h. Some

holes in the film can be gradually observed, which distributed randomly. The depth of the holes are identical with the original film thickness. As the holes gradually grew, the holes contacted each and decay into ribbons, and finally became into the droplets similar to type A. The number and the size of the droplets were dependent on the film thickness.

Xie et al.[113] investigated the spinodal dewetting phenomenon of a thin polystyrene film on a silicon substrate. They focused on the films composed of the polystyrene of low molecular weight (Mw=4000) with thin film thickness less than10nm. The films were annealed at 115℃ for different time periods in order to study the dewetting kinetics. The breakup were observed throughout the growth of the undulations, different from the nucleation of the holes for the thicker films (>10nm). The amplitude grew exponentially with time.

Redon et al.[114] studied kinetics of a viscous liquid film. PDMS and alkane films of 20-50μm prepared by spin-coating. The dewetting started from the center to the periphery driven by a capillary suction or an air blow. The receding velocity of the dewetting front is independent on the time and the film thickness. However, the velocity is inversely proportional to the oil viscosity.

Evaporative dewetting is referred to the retraction of a liquid film due to the evaporation. The liquid film might be able to wet the substrate and no dewetting would occur without evaporation. Most studies on evaporative dewetting have focused on the films of polymer solution or particle suspension and revealed that the evaporative dewetting can lead to the deposition or accumulation of non-volatile solute (polymer [115] or nanoparticles [116-118]) on the substrate surface and the formation of various labyrinthine structures and polygonal networks. [108, 119-122] The dewetting patterns are generally

associated with the formation and motion of three-phase contact lines and the instabilities in the vicinity of the contact lines during the dewetting.

A droplet of a volatile solvent on a rigid substrate is a typical system, whose dewetting kinetics has been widely studied. Generally, there are two types of the dewetting of a volatile solvent droplet, which is dependent on the wettability of the droplet on the substrate. For a wettable system, the dewetting usually follows a constant contact radius (CCR). [123, 124] In this mode, the contact line is pinned, and the contact angle gradually decreases with the evaporation. In contrast, for a non-wetting system, the droplet dewets in a constant contact angle mode [125], [125] [126-128] in which the contact line moves continuously with a constant contact angle. In some cases, the dewetting follows a mixed mode: the contact angle and contact radius change simultaneously. [129] The kinetics of the contact line motion is more complicated during the formation of the "coffee-ring" patterns, especially for the cases with a controlled template. The concentric "coffee-ring" patterns are usually constructed by the "stick-slip" dewetting of a droplet of polymer solution or suspensions. The contact line repeats several "pinning-depinning" cycles. [23, 56, 130, 131] In the pinning stage, the contact radius is constant, while the nominal contact angle decreases. In the depinning stage, both the contact radius and contact angle change. "advancing-receding" [50, 51] can be considered as a special case of the "stick-slip" motion, in which there is no steady "stick" stage, instead the contact line spread out a little bit towards the opposite direction of the main direction of the contact line motion.

Although a number of the studies have been done on the evaporative dewetting, seldom systematic studies have been focused on the kinetics of the dewetting controlled by a

template. Moreover, most works are on the case of the dewetting on rigid substrate, while few works have discussed the effect of deformable substrate.

Chapter 3. Evaporation-induced formation of self-organized gradient concentric rings on sub-micron pre-cast PMMA films

3.1 Introduction

Well-ordered surface structures at sub-micron scale have been extensively studied due to the potential applications in various areas, including stretchable electronics,[1, 12] photonics, [2] surface adhesion [5] and biosensory devices. [3] Various techniques have been developed to construct well-ordered surface structures at small scales, such as colloidal lithography, [132, 133] polymer demixing, [27, 32] surface wrinkling/buckling, [43, 44] nanoimprint, [34, 38] and fracture-induced structuring. [18, 49, 134] However, the applications of most of these techniques are more or less limited by high cost, low throughput, or the need of pre-fabricated mask.[18] For example, colloidal lithography [132, 133] and nanoimprint [34, 38] require high-quality mask which is usually expensive. Without a modified and pre-patterned substrate, the patterns produced by polymer demixing [27, 32] are irregular. Surface wrinkling/buckling [43, 44] is limited to "hard on soft layer" systems.

Evaporation-induced structuring has the potential to construct high-throughput surface structures. "Coffee ring" [24] is the most typical evaporation-induced pattern. The formation of "coffee ring" generally is controlled by the deposition of material, such as nanoparticles [8, 22] and polymer, [50] in the vicinity of the contact line of a sessile drop of particle suspension or polymer solution. Concentric rings over a large area can be formed after repeated "stick-slip" [22] or "advancing-receding" [50] cycles of the contact line during the evaporation of the drop. Nevertheless the evaporation-induced concentric rings are usually irregular, if the drop evaporation is not well controlled. Xu *et al.* [23] constructed highly-ordered gradient concentric rings by confining a polymer solution between a spherical lens and a flat silicon substrate. The evaporation of the polymer solution was limited at the side surface due to restriction of the "sphere-on-flat" geometry. With the "sphere-on-flat" geometry, gradient concentric rings made of various materials were successfully produced, including homopolymer, [56] polymer blend, [58] carbon nanotube, [60] block copolymer, [57] and semicrystalline polymer. [59] Based on the "coffee-ring" effect, Yabu *et al.* [66] used a computer-system to control the sliding movement of top glass plate to prepare periodic parallel "coffee-stain" stripes by confining a thin film of polymer solution between two glass plates. Although it has been demonstrated that highly ordered surface patterns can be formed by the evaporation process with the confinement of a solution between two solid surfaces, it is very difficult to use the evaporation process to construct regular surface patterns without surface constraint (such as the use of spherical lens or top glass slide) or precise evaporation control. Also, almost all the studies on the evaporation-induced structuring have been focused on the evaporation of polymer solutions or particle

suspensions. There is no report on the preparation of well-ordered structures, using a pure solvent droplet on a pre-cast film.

In this work, we develop a simple "particle-on-film" template to produce ordered surface pattern on pre-cast thin polymer films. In contrast to the surface confinement used by Xu *et al.* [23] and Yabu *et al.* [66] in controlling the evaporation of a polymer solution, the "particle-on-film" template, as shown schematically in Fig. 1, is constructed by placing a small particle on a pre-cast PMMA film to pin a solvent droplet and to control the evaporation of the droplet for the formation of concentric rings on the PMMA film. Note that no polymer solution is used. The effect of particle size and film thickness on the characteristics of the concentric rings is examined.

3.2 Dimensional analysis

To exploit the important factors that govern the geometrical characteristics, i.e. wavelength and amplitude, of the concentric rings, a dimensional analysis is applied. There are several independent variables controlling the wavelength λ and amplitude A of the formed concentric rings, including the average diameter of the particle D, film thickness h, distance to particle center d, viscosity η, modulus of the film E, spreading coefficient $\Delta\gamma$ in terms of the difference of the solid surface tension and the liquid surface tension together with the interface tension, contact angle θ, and evaporation rate R in the unit of kg/(m^{2}s). The wavelength as a function of these independent variables can be expressed as,

$$\lambda = f\left(D, h, d, \eta, E, \Delta\gamma, \theta, R\right) \tag{3.1}$$

Using D, $\Delta\gamma$ and R as fundamental quantities and the Π theorem given by Buckingham [135], one has

$$\frac{\lambda}{D} = \Pi_{\lambda}\left(\frac{d}{D}, \frac{h}{D}, \frac{\eta}{RD}, \frac{ED}{\Delta\gamma}, \theta\right) \tag{3.2}$$

Similarly, one has

$$\frac{A}{D} = \Pi_{A}\left(\frac{d}{D}, \frac{h}{D}, \frac{\eta}{RD}, \frac{ED}{\Delta\gamma}, \theta\right) \tag{3.3}$$

For the evaporation of a toluene droplet on the surface of a pre-cast PMMA film at an ambient temperature under the condition of stationary air, the parameters of R, E, η, $\Delta\gamma$ and θ remain constant. Thus, Eqs. **Error! Reference source not found.** and **Error! Reference source not found.** become

$$\lambda = D\Pi_{\lambda}\left(\frac{d}{D}, \frac{h}{D}\right) \text{ and } A = D\Pi_{A}\left(\frac{d}{D}, \frac{h}{D}\right) \tag{3.4}$$

Thus, the geometrical characteristics of the surface patterns formed via the "particle-on-film" template on a pre-cast PMMA and the evaporation of a toluene droplet is mainly controlled by D, d, and h. Here, we focus the study on the effects of the particle size D and the film thickness h.

Experimental details

The polymer used in this study was PMMA (Mw= 35000) (Fisher Scientific, Pittsburgh, PA), and the solvent for dip-coating was toluene (Fisher Scientific, Pittsburgh, PA). All the chemicals were used without further purification. Glass slides ($15 \times 20 \times 1$ mm^3) were used as the substrate for the dip-coating. The glass slides were cleaned three times by sonication in acetone, each for 15 min, and were then thoroughly rinsed with DI water. The particles used in the "particle-on-film" template were silicon carbide. SiC particles of near

roundness were selected, using an optical microscope (Nikon ECLIPSE LV100POL). The characteristic dimension of the particles was determined by calculating the "average diameter" of the optical images of the particles, using Image-Pro Plus (Media Cybernetics, Inc., Rockville, MD). Each particle was randomly placed on the surface of a glass slide three times, and a 2D optical image was taken. For each image, 4 measurements of the "diameter" were taken along four different directions, and an "average diameter" was calculated from the 12 measurements. The average diameters of the SiC particles used in this study are 360 ± 35μm, 312 ± 62μm, 242 ± 36μm, 160 ± 29μm, respectively.

Polymer solutions for the dip-coating were prepared by dissolving PMMA in toluene. The solution was heated to 120 ℃ and stirred for 10 min to obtain an isotropic, homogeneous solution. The solution was then dip-coated onto the cleaned glass slide. All the films were dried at 180 ℃ for 20 min to remove residual solvent. Controlling the solution concentration (0.5 *wt*%, 1 *wt*%, 2 *wt*%, 3 *wt*%), we obtained the PMMA films with the film thickness in the range of 50 nm to 190 nm, as measured by an atomic force microscope (Q-scope 250, Agoura Hills, CA).

The experimental set-up is shown in Fig. 3.1. A small SiC particle was carefully placed on the surface of a dip-coated PMMA film. A toluene drop of ~30 μL in volume was placed on the PMMA film with the particle being approximately at the center. The evaporation of the toluene drop took place in a glovebox at room temperature. Particles of different sizes were used to study the effect of particle size. In addition, the effect of the film thickness was examined, using the same SiC particles.

It took less than 3 min for the droplet to completely evaporate from the film surface. The evaporation process was monitored by a digital microscope (Dino-Lite Pro, Torrance,

CA). The surface morphology was characterized by an optical microscope (Nikon ECLIPSE LV100POL), and an atomic force microscope (Q-scope 250, Agoura Hills, CA).

3.3 Results

Figure 3.2a shows a typical optical image of the evaporation-induced surface patterns on the surface of the PMMA films with a particle to pin the toluene droplet. The film thickness was 135 nm, and the average particle diameter was 160 ± 29μm. An enlarged view is embedded in Fig. 3.2a to show the pattern near the particle. It is clear that well-organized concentric rings, surrounding the particle, were formed. The outermost rings consist of linked beads, *i.e.* bead-linked rings. The formation of the bead-linked rings was likely attributed to the Rayleigh–Taylor instability [136, 137] during the advancing-receding motion of the contact line at the "stick" stage. As shown in the video in the support material, the contact line of the droplet experienced repeated stick-slip motion during the evaporation. At the "stick" state, the contact line was not at a quasi-equilibrium state and had undergone advancing-receding motion. Note that the advancing-receding motion is different from the observation by Adachi *et al.* [51] in studing the assemply of nanoparticles during droplet evaporation and by Bi *et al.* [50] for the evaporation of polymer solution. This motion led to the accumulation of polymer at the contact edge, which resulted in the formation of the concentric rings after the receding motion at the "stick" state. With a droplet of large size, there was a high evaporation rate across the surface of the droplet, which likely induced a strong solutal convection along the contact line [9] and introduced local perturbations. Small, local perturbations during the advancing of the contact line at the "stick" state caused the Rayleigh–Taylor instability, which resulted in the formation of bead-linked rings. The solutal convection became smaller and negligible with the decrease

of the evaporation rate due to the decrease of the droplet volume. With continuous evaporation, the solutal convection became smaller and negligible and less local perturbations occurred. Smooth, concentric rings of small radii were formed. The concentric rings gradually evolved from bead-linked rings to smooth rings, as the distance to the particle decreased; as the ring approached the particle edge, it slowly conformed to the shape of the particle. This behavior reflects the effect of local curvature of the particle on the evolution of the surface pattern since the motion of the contact line is curvature-dependent. In addition, it was observed that some rings were disturbed by local surface defects, such as dusts, and sub-sets of concentric rings were even formed around the surface defects due to local pinning of the contact line.

For comparison, a typical surface structure created by the evaporation of a toluene droplet without the use of a particle on a pre-cast PMMA film of 135 nm in thickness is shown in Fig. 3.2b. Similar to those reported by Bi *et al.* [50] and Gonuguntla and Sharma, [9] a few irregular rings without a common center were formed. Such behavior is due to less control to the motion of the contact line than the "particle-on-film" system. The evaporation of toluene led to the wandering of the droplet on the PMMA film.

The undulations on the PMMA films were characterized by an atomic force microscope (Q-scope 250, Agoura Hills, CA). Figure 3.3a shows a typical AFM image of the undulations on a PMMA film of 135 nm in thickness, which consists of smooth concentric rings over the scanning area 40×40 m^2. Over the scan area, the arcs of the concentric rings appear parallel. A line scan perpendicular to the arcs, as shown in Fig. 3.3b, was drawn for determining the spatial wavelength and the amplitude of the rings. Both the spatial wavelength (distance between the centers of adjacent rings) and the amplitude

(height of the rings) decreased with the decrease of the distance to the center of the particle. The evaporation of the toluene droplet produced self-organized gradient concentric rings on the pre-cast PMMA film.

Effect of particle size

The effect of the particle size on the evaporation-induced concentric rings was examined on PMMA films of 135 nm in thickness. Due to the shape irregularity of the particles, average diameters of the particles as measured by an optical microscope are used to represent the particle size.

Figure 3.4a shows the variation of the wavelength with the distance to the particle center for several particle sizes. The wavelength decreases approximately linearly with the decrease of the distance to the particle center. This trend suggests that the slip distance between two adjacent "stick" states decreased as the contact line approached to the edge of the particle. This was due to less amount of toluene available for evaporation. Note that the distance to the particle center corresponds to the radius of the corresponding PMMA ring, and the slope of the wavelength versus the distance is closely related to the gradient of the concentric rings. For a wavelength, the size of the PMMA rings (distance to particle center) increases with the increase of the particle size. The slope of the wavelength versus the distance to the particle center is nearly the same for all the films with a particle of average diameter larger than or equal to 160 μm.

To further investigate the effect of particle size on the wavelength of the concentric rings and eliminate the effect of the ring size, the wavelength versus the distance to the particle surface is depicted in Fig. 3.4b. Compared with the distance to particle center, the distance to particle surface excludes the particle size, and by establishing a relation between

the wavelength and the distance to the particle surface, a common relation between the wavelength of a ring with its position, independent on the particle size, is expected to be figured out. One can note that all the curves nearly coincide to a single line, and there is only a slight deviation for the results of the 160 μm particle. The slope is approximately independent of the particle size. The average slope is 0.113 ± 0.009, which represents the ratio of the wavelength to the distance to particle surface and may be affected by other factors (i.e. evaporation rate, surface tension and contact angle). It is worth of mentioning that the curvature effect of particle likely has some effect on local undulation of the surface structures.

Figure 3.5 shows the dependence of the amplitude of the concentric rings on the wavelength for several particle sizes. The amplitude linearly decreases with decreasing the wavelength. According to Fig. 3.3, it can be believed that the dimensions of a ring (*i.e.* the amplitude and the width) are dependent on the amount of the PMMA that was swiped into the shrunken droplet during the slip. Less amount of the PMMA was moved into the droplet for smaller slip distance, *i.e.* smaller wavelength. This trend limited the amount of the PMMA available for the formation of the ring. Thus, rings of small sizes were formed for small wavelengths.

Figure 3.6 shows the variation of the slope of the amplitude verse the wavelength with the particle size. The slope of the amplitude verse the wavelength decreases with the decrease of the average diameter of the particle, reflecting the effect of particle size on the evaporation-induced gradient concentric rings. Particles of small sizes have less constraint to the surface area of the evaporation, and more toluene evaporates for the same time interval.

Using Eq. (3.4) and the results presented in Fig. 3.5, one obtains

$$\Pi_A\left(\frac{d}{D},\frac{h}{D}\right)=\alpha\Pi_\lambda\left(\frac{d}{D},\frac{h}{D}\right)+g(\frac{h}{D}) \tag{3.5}$$

with α representing the slope of the amplitude verse the wavelength and $g(h/D)$ being a function of *h/D* and the material properties. Eq. (5) gives a simple scaling relation between the wavelength and amplitude of the concentric rings, the slope α is a function of *h* and D, which is reflected by the results shown in Fig.6 and Fig.9.

Effect of film thickness

The effect of the film thickness of the PMMA films on the formation of the evaporation-induced concentric rings was examined, using a SiC particle of average diameter of 160 ±29μm. The film thicknesses were 50, 90, 135, and 190 nm. Similar surface structure of concentric rings was observed over all the PMMA films, even for the thinnest PMMA film of 50 nm in thickness, using an optical microscope (Nikon ECLIPSE LV100POL) and an atomic force microscope (Q-scope 250, Agoura Hills, CA). The size of the "particle-influenced" region was found to be independent of the film thickness.

The surface topology of the concentric rings was characterized, using atomic force microscope. Figure 3.7 shows the variation of the wavelength with the distance to the particle center for four different film thicknesses. The wavelength decreases linearly with the decrease of the distance to the particle center, in accord with the observation for different particle sizes. The slope of the spatial wavelength verse the distance increases slightly with increasing the film thickness, which suggests the dependence of the ring structure on the film thickness. For a thick PMMA film, more toluene penetrates into the film across the interface between the toluene and the film and forms a soft, flowable layer.

For the same tangential force (stress) due to the unbalance of the surface tensions, there is less confinement from the PMMA film to the motion of the contact line and larger slip occurs for a soft, thicker layer. The larger slip results in larger distance between two rings and larger wavelength for the same distance to the particle center.

Figure 3.8 shows the dependence of the amplitude of the rings on the wavelength for four different film thicknesses. The linear dependence of the amplitude of the rings on the wavelength is independent of the film thickness for the experimental conditions, which supports Eq. (3.5). This result suggests that the same mechanism, *i.e.* the evaporation-induced unbalance of tangential force (stress) and the softening of the PMMA layer, controls the formation of the concentric rings. The variation of the slope of the amplitude verse the wavelength with the film thickness is shown in Fig. 3.9. An approximately linear dependence of the slope of the amplitude verse the wavelength on the film thickness is observed. The reason for the linear relationship is unclear. The increase of the slope of the amplitude verse the wavelength with the film thickness is likely due to the formation of a soft, thick PMMA layer near the interface between the toluene and a thick PMMA film, and more PMMA is moved into the droplet during the receding of the contact line. Rings of large amplitudes due to the excess amount of PMMA near the contact line are formed on thick films at the "stick" state.

3.4 Summary

In summary, we have demonstrated the formation of self-organized surface structure through the evaporation of a toluene droplet on a pre-cast PMMA film. Using a "particle-on-film" template, well-ordered concentric rings were produced on pre-cast PMMA films. The particle was used to pin the toluene droplet to avoid the random motion of the droplet

induced by the evaporation. The formation of the concentric rings is a consequence of stick-slip motion of the contact line, which involved an unconventional "advancing-receding" motion of the contact line at the "stick" state. The dimensions of the ring-structures are dependent on the particle size and the film thickness. Both the spatial wavelength and the amplitude decrease with the decrease of the distance to the center of the particle. The slope of the amplitude verse the wavelength decreases with the decrease of the particle size, reflecting the effect of particle size on the evaporation-induced gradient concentric rings. The linear dependence of the amplitude of the rings on the wavelength is observed, which is independent of the film thickness for the experimental conditions.

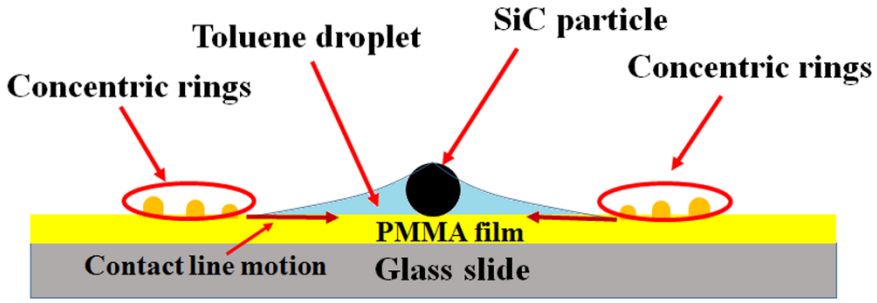

Figure 3.1 Schematic of the evaporation of a toluene droplet via a "particle-on-film" template and the formation of gradient concentric PMMA rings on a pre-cast PMMA film

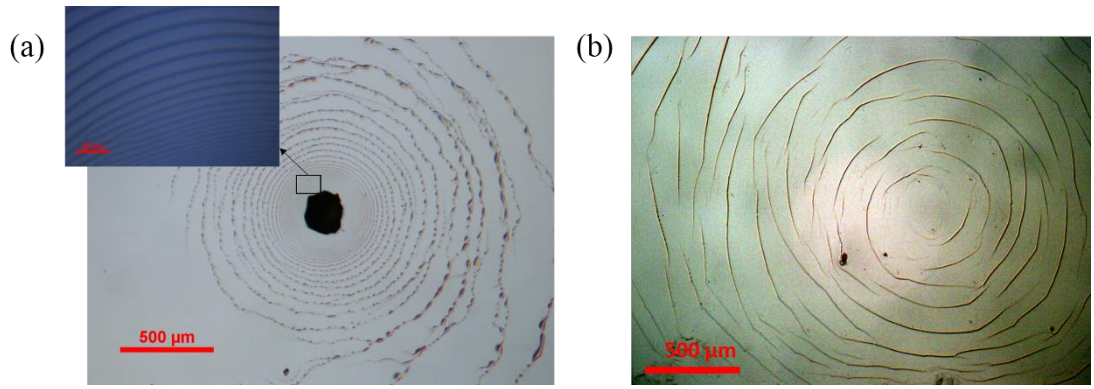

Figure 3.2 Optical images of the evaporation–induced surface patterns: (a) surface pattern with a particle in the drop (film thickness: 135 nm; average particle diameter: 160 ± 29µm), and (b) surface pattern without a particle in the drop (film thickness: 135 nm)

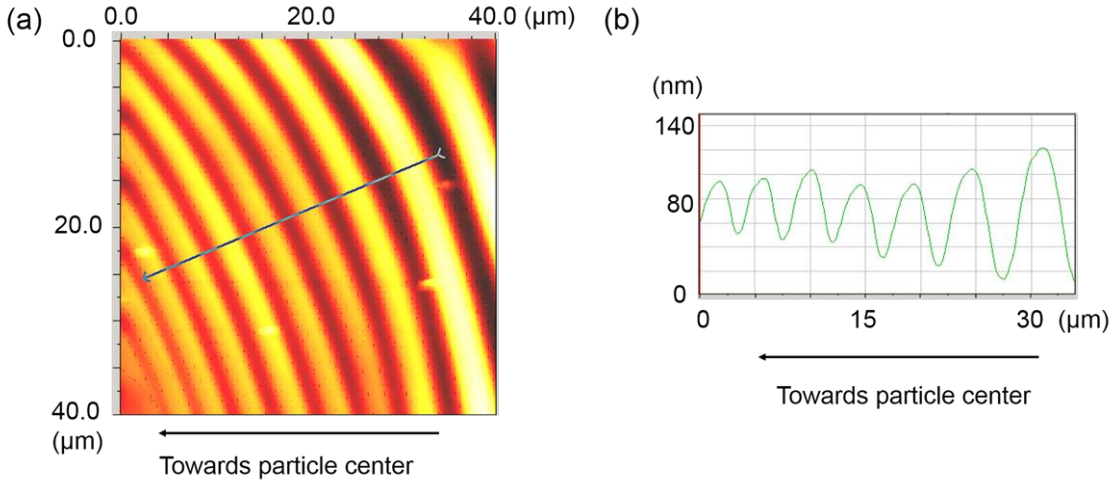

Figure 3.3 (a) AFM image of the concentric rings over an area of 40×40 µm2, and (b) surface profile of the concentric rings (film thickness: 135 nm; average particle diameter: 160 ± 29µm)

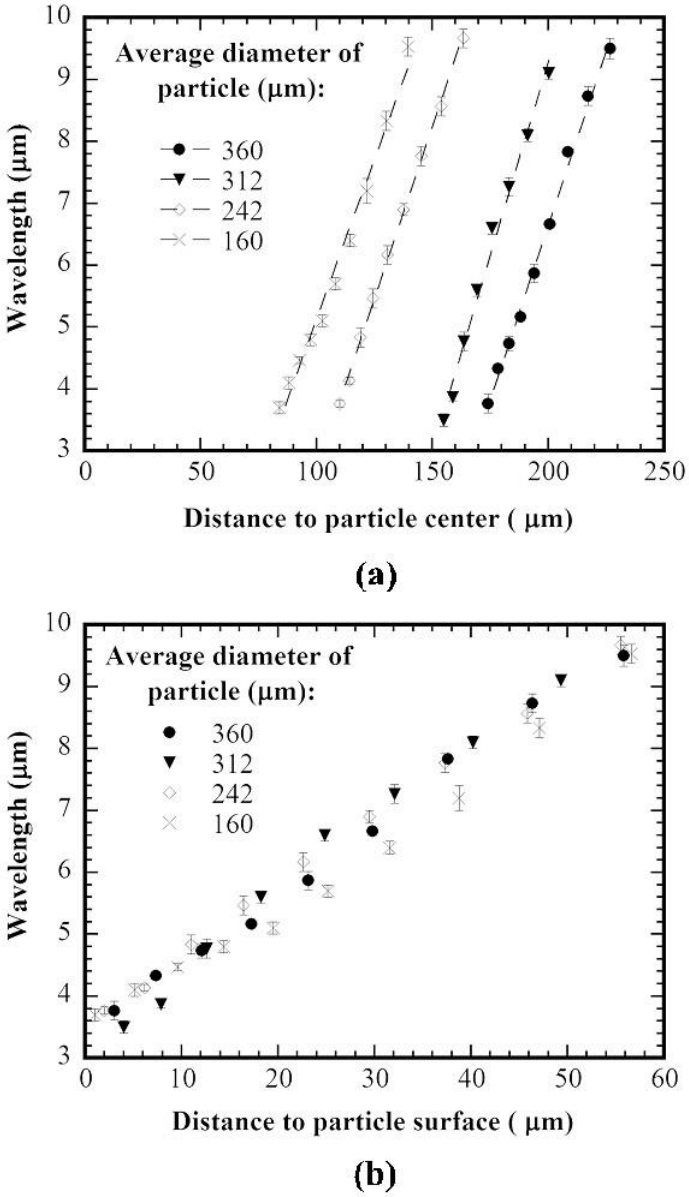

Figure 3.4 (a) Variation of the wavelength of smooth concentric rings with the distance to the particle center for four different particle sizes; (b) Variation of the wavelength of smooth concentric rings with the distance to the particle surface for four different particle sizes (film thickness: 135 nm)

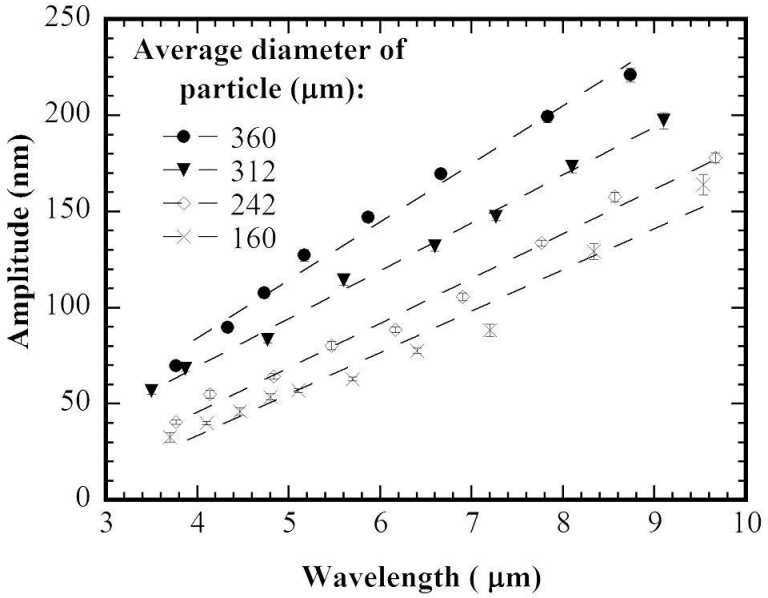

Figure 3.5 Correlation between the wavelength and the amplitude of smooth concentric rings for four different particle sizes (film thickness: 135 nm)

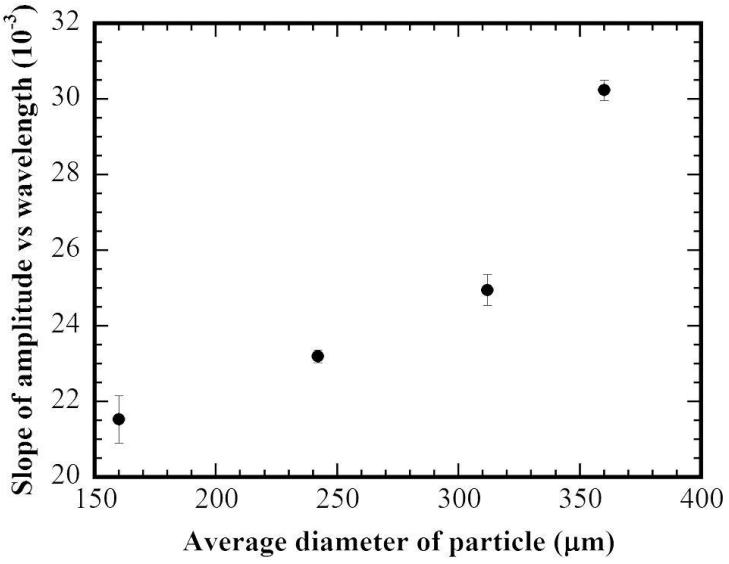

Figure 3.6 Dependence of the slope of the amplitude verse the wavelength on the particle size (film thickness: 135 nm)

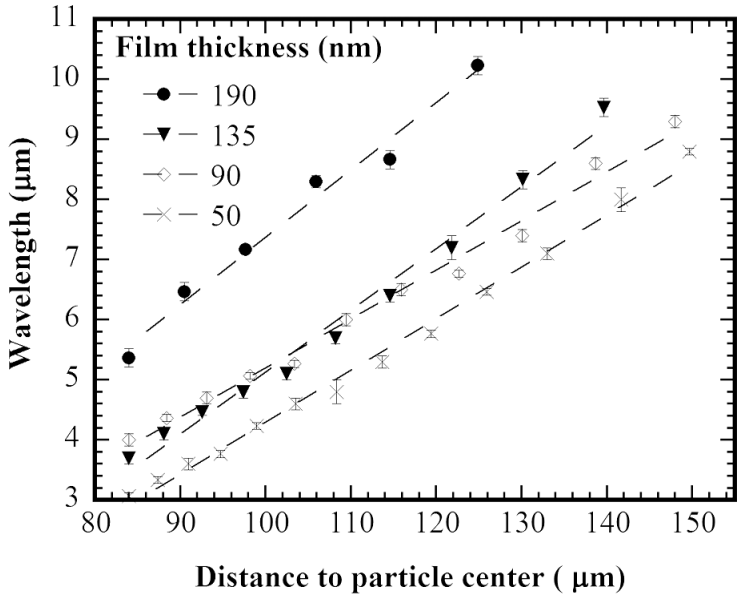

Figure 3.7 Variation of the wavelength of smooth concentric rings with the distance to the particle center for four film thicknesses (average particle diameter: 160 ± 29μm)

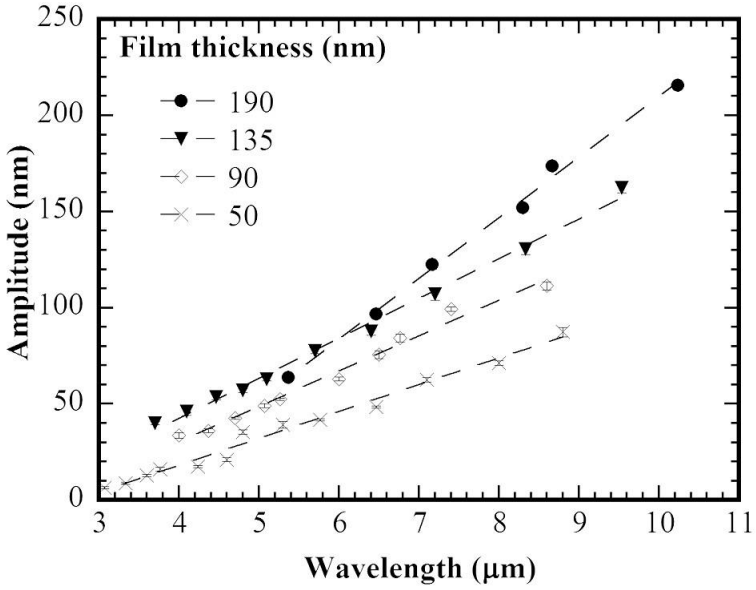

Figure 3.8 Correlation between the wavelength and the amplitude of smooth concentric rings for four film thicknesses (average particle diameter: 160 ± 29μm)

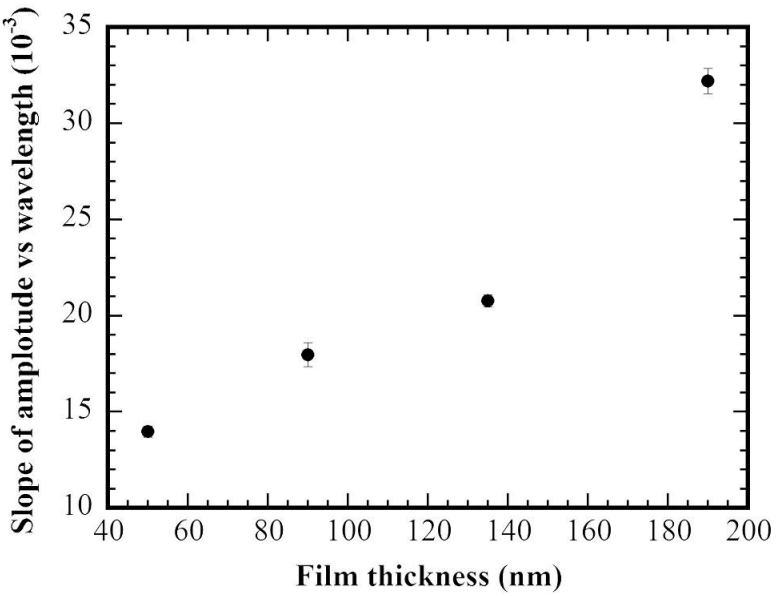

Figure 3.9 Dependence of the slope of the amplitude verse the wavelength on film thickness (average particle diameter: 160 ± 29μm)

3.5 Supporting Information

The split of the droplet in the video (at about 2 s in the video, which is 67 s after the droplet was deposited on the PMMA film) is due to the pinning effect of the particle. The particle size determines the onset of the split. With continuous evaporation, the morphology of the toluene droplet gradually changed and finally split into two "sub-droplets". Here, we mainly focus on the evaporation behavior of the "sub-droplet" pinned by the particle and the patterns formed after the evaporation of this "sub-droplet". Note that the split of a large droplet into two "sub-droplets" occurred in all the experiments in

this study. The arrow points to the SiC particle, which corresponds to the slip direction of a sub-droplet.

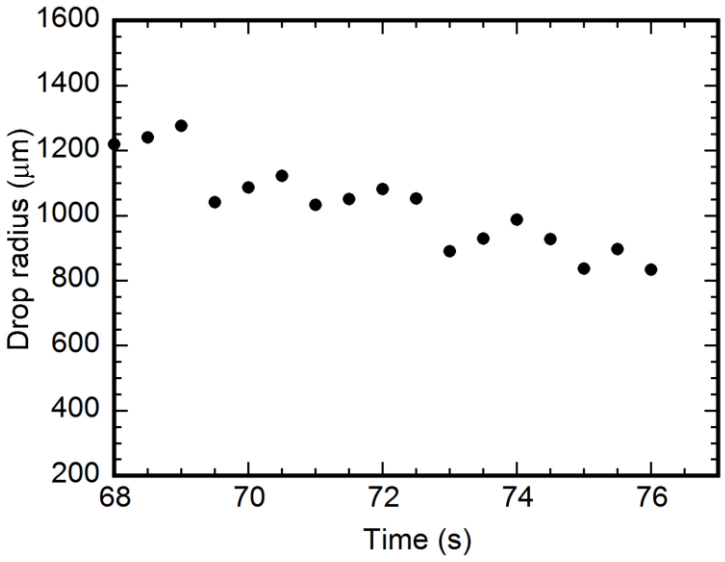

Figure 3.10 Variation of the drop radius with evaporation time during a toluene drop evaporating on a PMMA film with a particle in the drop (film thickness: 135 nm; average particle diameter: 160 ± 29μm).

The particle center was set as the drop center. This plot describes the "advancing-receding" motion of the contact line in the direction indicated by the arrow in Video 1.

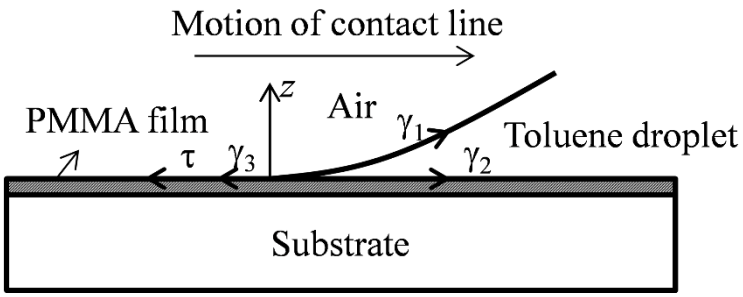

Figure 3.11 Schematic of the external forces exerted on contact line during stick-slip motion

It is known that the stick-slip motion of the contact line is determined by the tangential components of surface tensions at the contact line. [138] As discussed above, the penetration of toluene into the PMMA film results in the formation of a soft, flowable PMMA layer near the interface between the toluene and the PMMA film. During the motion of a contact line, the soft, flowable PMMA layer experiences local deformation and flow which affect the stick-slip behavior of the contact line. Figure 3.11 shows a schematic of a contact line under the action of external forces during the stick-slip motion of a toluene droplet on a PMMA film. Accordingly, the equation of motion of a contact line can be expressed as

$$\rho \frac{d^2 x}{dt^2} = \gamma_1 \cos\theta + \gamma_2 - \gamma_3 - \tau \tag{3.6}$$

where ρ is the line density of mass for the contact line, t is time, γ_1 is the surface tension between toluene and air, γ_2 is the surface tension between toluene and the PMMA, γ_3 is the surface tension between air and PMMA, θ is the nominal contact angle of the droplet, and τ is the line force (force per unit length) exerted on the contact line due to the deformation and flow of the soft, flowable PMMA layer near the interface between the toluene and the PMMA film. x is the displacement of the contact line, which is equal to $R - R_0$ with R being the radius of the droplet and R_0 being the radius of the droplet at the pinning (stick) state.

Some polymer melts and polymer solutions exhibit viscoelastic properties due to the entanglement of the chains.[139-141] If the convection and diffusion of the polymer in the vertical direction is low, the concentration of the polymer should be high and in the thin contact zone should be nearly saturated. [9] So we assume that the soft, flowable layer should

exhibits viscoelastic property due to the high concentration and chain entanglement, and the Voigt-Kelvin model, a widely-used viscoelastic model, [142-145] can be used to describe the rheological behavior of the soft, flowable PMMA layer, so that one has

$$\tau = 1 \cdot \left(\eta \frac{\partial \mathrm{v}}{\partial z} + \mu \frac{\partial u}{\partial z} \right)_{\text{interface}} \approx \frac{\eta}{\alpha h} \frac{dx}{dt} + \mu \frac{x}{\alpha h} \tag{3.7}$$

where 1 represents the unit length of the contact line, η is viscosity, μ is shear modulus, v is tangential velocity, u is tangential displacement, h is the thickness of the PMMA film, and α is the ratio of the thickness of the soft, flowable PMMA layer to the thickness of the PMMA film. Note that the reference state is referred to the quasi-stationary (stick) state of the droplet before the onset of the slip motion of the contact line. Substituting Eq. 3.7 into Eq. 3.6 yields

$$\rho \frac{d^2 x}{dt^2} + \frac{\eta}{\alpha h} \frac{dx}{dt} + \mu \frac{x}{\alpha h} = \gamma_1 \cos\theta + \gamma_2 - \gamma_3 \tag{3.8}$$

for the motion of the contact line.

To the first order of approximation, there is $\cos\theta \approx \cos\theta_0$ (θ_0 is the nominal contact angle of the droplet at the onset of the slip motion). Using the initial conditions of $x = 0$ and $dx/dt = 0$ at t=0, the variation of the droplet size with time is found as

$$R = R_0 - x \tag{3.9}$$

$$= R_0 - \frac{\alpha h(\gamma_1 \cos\theta_0 + \gamma_2 - \gamma_3)}{\mu} \left[1 - \left(\cosh \frac{\sqrt{\eta^2 - 4\alpha h \mu \rho}}{2\alpha h \rho} t + \frac{\eta}{\sqrt{\eta^2 - 4\alpha h \mu \rho}} \sinh \frac{\sqrt{\eta^2 - 4\alpha h \mu \rho}}{2\alpha h \rho} t \right) e^{-\frac{\eta}{2\alpha h \rho} t} \right]$$

The droplet size during the slip is an exponential decay function of time before reaching next quasi-stationary state, qualitatively in accord with the experimental observation. From Eq. 3.9, one can define the characteristic time as $2\alpha h\rho / \eta$. It is clear that the characteristic

time increases with increasing the film thickness. Generally, the slip distance (wavelength) can be approximately calculated by the multiplication of the characteristic time and the slip speed, which suggests that the slip motion of a contact line over a thick PMMA film has large slip distance, i.e. wavelength, as supported by the experimental results shown in Fig. 3.6.

According to Eq. (3.4), oscillatory solution is obtained for $\eta^2 < 4\alpha h\mu\rho$, which indicates the presence of local receding-advancing-receding motion of the contact line. Such behavior has been observed experimentally at the "stick" state (Video S1). However it needs to point out that the underlying mechanism is more complicated; it likely involves the fluid-structure interaction between the droplet and the soft, flowable PMMA layer and the evaporation-induced fluid flow in the droplet. One needs to consider the effect of the outward flow near the contact line at the "stick" state on the motion of the contact line since the flow inside the droplet may introduce outflow component of the flow velocity and lead to the soft, flowable PMMA towards to the contact line.

Chapter 4. Formation of self-organized gradient stripes on pre-cast PMMA films

4.1 Introduction

Surface patterns, especially those in small scales have application potentials in various areas, including electronics,[12] photonics,[2, 47] surface adhesion,[5] tissue engineering[4] and biomaterials.[3, 146] Evaporation-induced surface patterns have the potential to produce well-ordered surface structures with high-throughput in an effective and efficient way. "Coffee ring" [24] is the most typical evaporation-induced surface pattern. When a sessile droplet of polymer solution[50, 53, 147] or nanoparticle suspension [22, 51, 69, 148] is evaporated, non-volatile solute is left in the vicinity of the three-phase contact line to form a ring-like pattern. Concentric ring-like pattern covering a large area can be formed after a series of "stick-slip" [149] or "advancing-receding" [51] motion of the contact line. However the concentric rings are usually irregular without controlling the evaporation.[9, 50] Well-ordered concentric rings with the gradient of wavelength and amplitude have been constructed by Lin and Granick [56] *via* controlling the evaporation of a polymer solution droplet with a "sphere-on-flat" geometry. Gradient concentric rings made of various materials have been fabricated with the "sphere-on-flat" geometry, including homopolymer,[23] polymer blend,[58] block copolymer,[57] semi-crystalline polymer[59] and carbon nanotube.[60]

Evaporation-induced surface patterns are not limited to a single ring or concentric rings, other patterns can also be formed due to the deposition of non-volatile solute around the contact line. Periodic stripes with high regularity are another typical evaporation-induced pattern. Uchiyama and co-workers[20, 70] produced stripe-patterned organic-inorganic hybrid films, which is based on the "coffee-ring" effect *via* dip-coating process. They found that solution concentration, temperature and withdrawal speed play important roles in determining the formation and characteristics of the stripe-like patterns. Park et al.[64] fabricated highly regular polymer stripes with uniform width and intervals on both rigid and flexible substrate via a roll-based evaporation-induced self-assembly method. Yabu et al.[66] developed a "computer-controlled" system to control the sliding motion of the top glass plate to construct highly-ordered polymer stripes by evaporating a polymer solution film, which is confined between two glass plates. Although well-ordered stripe-like patterns can be formed through evaporation-induced self-assembly, using the above-mentioned methods, it is very difficult to fabricate regular stripe-like patterns without controlling the contact line motion precisely. Lin and co-workers[11, 150, 151] used "lens-on-flat" geometry to fabricate well-ordered striped patterns made of various materials, which cover a larger area and show application potentials. However "top restriction" (i.e. lens of different shapes) is always needed in this method.

In this work, we developed a new strategy to fabricate highly-ordered gradient polymer gratings with reflection symmetry on pre-cast PMMA films without controlling the evaporation of a solvent droplet. In this method, a single copper wire is placed on a pre-cast PMMA thin film to limit the motion of a toluene droplet automatically, and no "top restriction" (i.e. glass plate or lens) is used. The effects of the diameter of the copper wires

and the thickness of the PMMA films on the gradient patterns are characterized. Using a "wire-on-film" system with two parallel copper wires, the effect of the wire interaction is also examined.

4.2 Experimental details

Materials

PMMA (Mw=35000) (Fisher Scientific, Pittsburgh, PA) was dissolved in toluene to prepare a polymer solution for dip-coating. Glass slides ($15 \times 20 \times 1$ mm^3) as the substrate were ultrasonically cleaned in acetone for 5 min for 3 times, thoroughly rinsed with DI water and dried with warm condensed air. Bare copper wires (40 AWG, 38 AWG and 24 AWG) (ARCOR, Northbrook, IL) were cut into wire segments of 15 mm in length. The wire segments were cleaned with toluene ultrasonically and dried with condensed air.

Pre-cast PMMA thin film

The pre-cast PMMA films on glass substrates were prepared by a fast dip-coating process at room temperature. The withdrawal speed was 30 cm/min. All the films were dried at 180 ℃ for 20 min to remove the residual solvent. Films of different thicknesses (50 nm, 90 nm and 140 nm) were prepared. To determine the film thickness, a scratch is made on the film carefully using a razor blade, and the depth of the scratch (film thickness) is measured by AFM.

Fabrication of the evaporation-induced gradient stripes with a single copper wire

A single straight copper wire was carefully placed on the surface of a dip-coated PMMA film, with its longitudinal axis parallel to the 15-mm edge of the glass substrate. A toluene droplet of 20μL in volume was placed on the PMMA film using a micropipette, with the copper wire approximately as the symmetrical axis. After initial spreading, the three-phase

contact line was pinned. The droplet had an elliptical shape, rather than a typical spherical cap due to the confinement of the copper wire. The evaporation of the toluene droplet took place at room temperature.

Fabrication of the evaporation-induced gradient stripes with two parallel copper wires

In addition to using a single copper wire for the surface patterning, two parallel copper wires were also used to construct surface patterns on the pre-cast PMMA films. Two copper wires of the same diameter and length were placed on the film surface. The longitudinal axis of the wires was parallel to the 15-mm edge of the glass substrate. A toluene droplet of 20 μL in volume was placed on the PMMA film with the center of the two copper wires as the center, and the droplet evaporated at room temperature. The effect of the diameter of the copper wires on the surface patterns was studied using copper wires of different diameters of 51 μm, 79 μm and 102 μm. The distance between the centers of the two copper wires were changed in the range of 1200 μm to 3500 μm in order to study the effect of the distance between two wires on the surface patterns.

Characterization

The surface morphology was characterized by an optical microscope (Nikon ECLIPSE LV100POL) and an atomic force microscope (Q-scope 250, Agoura Hills, CA). The characteristics of the surface patterns were analyzed, using the AFM software and Image Pro plus. The mechanical properties of the film before and after the droplet evaporation was detected by Nanoindentation (Hysitron TriboScope, Minneapolis, MN) using the following parameter: maximum load is 10μN, loading time is 10s, unloading time is 10s, and holding time is 20s.

4.3 Results

Figure 4.1a shows the evaporation-induced patterns formed on the surface of a pre-cast PMMA film after the evaporation of a pure toluene droplet, using a single copper wire. The thickness of the pre-cast PMMA film was 90 nm, and the diameter of the copper wire was 79 μm. Parallel polymer stripes were formed on both sides of the copper wire. The outermost stripes are less regular than those near the copper wire, which is due to the morphological evolution of the three-phase contact line from an irregular curve to a nearly straight line.

The spatial wavelength and the amplitude (height) of the stripes formed near the copper wire were further measured by an atomic force microscope (AFM) (Q-scope 250, Agoura Hills, CA). Figure 4.2a shows a typical AFM image of the stripes formed on a PMMA film of 90 nm in thickness with a copper wire of 79 μm in diameter. Smooth, parallel stripes are observed in the AFM image, and the spatial wavelength and amplitude of the parallel stripe-like pattern were determined by drawing a straight line perpendicular to the stripes. As shown in Figure 4.2b, both the spatial wavelength and the amplitude of the stripes gradually decrease with the decrease of the distance to the copper wire center.

Gradient surface stripes were constructed on PMMA films of 90 nm in thickness, using copper wires of different diameters of 51, 79, and 102 μm. Figure 4.3 shows the variation of the spatial wavelength with the distance to the copper wire center. The spatial wavelength decreases linearly with the decrease of the distance to the copper wire center.

Figure 4.4 shows the correlation between the amplitude and the spatial wavelength of the gradient stripes for the copper wires of three different diameters. The amplitude increases

linearly with the increase of the wavelength of the gradient stripes for all the copper wires used.

Gradient surface stripes were constructed on PMMA films of 50, 90, and 140 nm in thickness. Similar surface structure of straight stripes was observed on all the PMMA films. For all three PMMA films, the amplitude of the smooth stripes increases linearly with the spatial wavelength, independent of the diameter of the copper wires. Figure 4.5 shows the variation of the slope of amplitude verse wavelength with the film thickness for three copper wires of 51, 79 and 102 μm in diameter. The slope of amplitude verse wavelength for the smooth stripes increases with the increase of the film thickness. For the same spatial wavelength, the stripes formed on a thicker film have larger amplitudes than those on a thinner film due to more flowable PMMA available for accumulating near the contact line at the "stick" state. The copper wire of larger diameter produced smooth surface stripes with larger slope of amplitude verse wavelength. The slope of amplitude verse wavelength is the smallest for the thinnest film; there is no significant difference between the slopes for the surface stripes formed on the film of 50 nm, using the copper wires of 51 and 79 μm in diameter, respectively.

Figure 4.6 shows the gradient surface stripes formed on a PMMA film *via* the evaporation of a toluene droplet, which was pinned by two parallel copper wires. The film thickness was 90 nm, and the diameter of both copper wires was 79 μm. The distance between the centers of the copper wires was 1695 μm. Parallel polymer stripes, which were formed on both sides of the copper wires, are observed. The embedded image in Fig. 4.6a shows the enlarged view of the surface patterns in the region enclosed by the rectangular box. Near the copper wire, well-ordered smooth, straight stripes were formed on both sides,

which are similar to the surface patterns formed *via* a single copper wire. There is no significant asymmetry of the innermost patterns according to the embedded optical image. A featureless zone between the copper wires is observed, and irregular stripes, as show in Fig. 4.6b, are observed on the outmost region outside the two copper wires.

The interaction between two parallel copper wires influences the formation and characteristics of the surface stripes formed on the PMMA films. The extent of the interaction is dependent on the distance between the two copper wires. The effect of the distance between two copper wires on the formation of smooth, straight stripes was investigated on PMMA films of 90 nm in thickness, using copper wires of 51, 79 and 102 μm in diameter. Both copper wires had the same diameter, and the distance between two copper wire centers was in the range of 1.2 mm to 3.5 mm.

Figure 4.7 shows the variation of the wavelength of smooth stripes with the distance to individual copper wire centers and the correlation between the amplitude and the wavelength of the stripes. Here, the smooth stripes were formed on a PMMA film of 90 nm in thickness, using two copper wires of 79 μm in diameter with the distance between the two wire centers being 1.7 mm. Similar to the surface stripes formed by using a single copper wire, the wavelength increases linearly with increasing the distance to the individual copper wire centers, and the amplitude is a linear function of the wavelength. There is no significant difference between the stripes of the left side and those of the right side for each individual copper wire. The smooth stripes near the individual copper wires have relatively good symmetry with the corresponding copper wire as symmetric axis. Also no significant difference is observed between the stripes near the left wire and those near the right wire.

For simplicity, we mainly focus on the smooth stripes formed between the copper wires in the following discussion.

Figure 4.8 shows the variation of the slope of amplitude verse wavelength with the distance between two copper wires for a film thickness of 90 nm and the copper wires of 51, 79 and 102 μm in diameter. For comparison, the results for the smooth stripes formed by using a single copper wire are also included in Fig. 8. Generally, the slope of amplitude verse wavelength for the stripes made by the copper wires of 79 and 102 μm in diameter increases with the increase of the distance between two wires in the range of 1.2 to 3.5 mm, The large value of the ratio for the stripes formed by the copper wires of 102 μm diameter at the distance of 1.82 mm might be due to the thickness non-uniformity of the PMMA film or local disturbance to the evaporation, which caused the large deviation. For the strips formed by the copper wires of 51 μm diameter, the slope of amplitude verse wavelength first increases, reaches the maximum, and then decreases with the increase of the distance between two wires. The reason for such behavior is unclear. Note that, for the same wavelength, the amplitudes of the stripes formed with two copper wires of 51μm diameter are almost the same as those formed with a single wire when the distance between two wires was larger than 2.3 mm. It is interesting to note that the slope of amplitude verse wavelength for the stripes made by single individual copper wires of 51, 79, and 102 μm diameters, respectively, is different from that made by the corresponding two copper wires of the same diameter. This result reveals the interaction of the copper wires which interfered with the formation of the surface stripes near the copper wires. The interaction between copper wires limited the evaporation of the toluene droplet confined between the wires and played a role in controlling the motion of the contact lines.

The splitting of a droplet confined between two parallel wires led to the formation of a featureless zone, as shown in Fig. 6a. The size of the featureless zone is determined by the distance between the innermost surface stripes, associated with the first individual stick states of the corresponding contact lines. Figure 4.9 shows the dependence of the size of the featureless zone on the center distance between two parallel copper wires for three copper wire sizes. The copper wires were placed on a PMMA film of 90 nm thickness. The size of the featureless zone increases linearly with increasing the distance between two copper wires. For the same distance between two copper wire centers, the size of the featureless zone formed by large copper wires is less than that formed by small copper wires. The effect of the film thickness on the size of the featureless zone was examined on the PMMA films of 50, 90, and 140 nm, using copper wires of 79 m diameter. The size of the featureless zone increases linearly with increasing the distance between two copper wire centers, independent of the film thickness. The slopes of the size of the featureless zone verse the distance between two copper wire centers are 0.52, 0.55, and 0.47 for the film thicknesses of 50, 90, and 140 nm, respectively. This result suggests that the first slipping distance of the contact lines after the splitting of the droplet into two "sub-droplets" is independent of the film thickness.

4.4 Discussions

Evaporation-induced surface pattern via a single copper wire

The polymer stripes were formed as the contact line underwent a series of "stick-slip"[9] or "advancing-receding" motion.[50, 51] The contact line motion can be described by the force exerted on the contact line as in Eq (1):

$$\rho \frac{d^2x}{dt^2} = \gamma_1 \cos\theta + \gamma_2 - \gamma_3 - \tau$$

(4.1)

where ρ is the line density of mass for the contact line, t is time, γ_1 is the surface tension between toluene and air, γ_2 is the surface tension between toluene and the PMMA, γ_3 is the surface tension between air and PMMA, θ is the nominal contact angle of the droplet during the contact line motion, and τ is the resisting force (force per unit length) exerted on the contact line due to surface roughness near the PMMA-toluene interface. *x* is the displacement of the contact line. Assuming the contact line is first pinned, as the evaporation, the nominal contact angle θ gradually decreases resulting in an increasing tangential surface tension $\gamma_1 \cos\theta + \gamma_2 - \gamma_3$ which drives the contact line to slip. Due to the accumulation of the polymer in the vicinity of the contact line by the contact line motion, the roughness at the interface which resists the contact line motion increases, and the contact line would be pinned at some location. As the evaporation continues, a new "stick-slip" cycle would begin.

As suggested by Sun and Yang,[152] the motion of the contact line led to the accumulation of the softened PMMA in the vicinity of the contact line, which formed the stripes with the shape similar to the corresponding contact line at the "stick" state. The vertical surface tension at the contact line can also contribute to the deformation of the soft layer.[153-156] The softening effect of the droplet to the film can be reflected by the mechanical properties of the "toluene droplet-treated PMMA" after completely drying. Nanoindentation was performed to detect the mechanical properties under the following conditions: Maximum load is 10μN, loading time is 10s, unloading is 10s, and holding time is 20s. Under the

experimental conditions, the Young's modulus of the PMMA film before droplet evaporation is 15.04 ± 0.76 Gpa and the hardness is 0.42 ± 0.06. In comparison, after evaporation, the Young's modulus and hardness of the PMMA film decrease to 7.10 ± 1.16 Gpa and 0.29 ± 0.02, respectively. This result proves that the PMMA film can be softened by the toluene droplet.

At the onset of the evaporation, the contact line was not regularly straight and the movement was less uniform. As the droplet became smaller, the effect of the copper wire on the shape of the droplet and the motion of the contact line became more significant. The contact line became straight and moved more orderly. The well-ordered gradient stripes formed near the copper wire are shown in Fig. 4.1b.

As shown in Fig. 4.1a, the outermost stripes are bead-linked lines, which can be attributed to the occurrence of the Rayleigh–Taylor instability[157] during the "stick" state of the contact line . At the "stick" state, the contact line was not at an equilibrium state and had undergone advancing-receding motion. When the droplet was relatively larger, the high evaporation rate and the viscous flow inside the droplet likely induced local disturbance to the contact line during the advancing motion at the "stick" state, which grew and caused the formation of the bead-linked lines. With continuous evaporation, the droplet became smaller. Both the evaporation rate and the viscous flow rate towards the contact line inside the droplet became smaller, and less local disturbance occurred. Smooth gradient stripes were formed in the region near the copper wire as shown in Fig.4.1b. With the evolution from the bead-linked stripes to smooth-straight stripes, one can note that the spatial wavelength (distance between the centers of the adjacent stripes) decreases with the decrease of the distance to the copper wire center.

The result shown in Fig.4.3 indicates that the slipping distance of the contact line between two adjacent "stick" states decreased as the contact line approached the copper wire. This phenomenon may be explained from the aspect of long-range interfacial interaction (i.e. van de Waals force) between the solvent droplet and the pre-cast film. Without the copper wire confinement, toluene is able to complete wet the PMMA due to the high solubility, and forms a thin liquid film. However with a copper wire, a meniscus zone appears near the wire and the thickness of the toluene film decreases with the increase of the distance to copper wire. Without evaporation, this system is stable when the thickness of the toluene film is larger than a critical value e_c, with $\frac{d^2\mathrm{P(e)}}{\mathrm{d}e^2} > 0$ where P(e) is long-range interfacial energy and e is the thickness of toluene film.[99] As evaporation, the local toluene film near the contact line becomes unstable when it is thinner than the critical thickness e_c, and then the contact line starts to recede to the bulk droplet to seek a thicker film and a stable status. When the contact line is relatively further from the copper wire, where the local toluene film is thin and the evaporation rate is high, a longer receding distance is needed to reach a stable status than the case that the contact line is nearer to the copper wire and with a thicker toluene film next to it, resulting in the decreasing wavelength gradient.

The average rate of the wavelength to the distance to the copper wire center decreases with the increase of the diameter of the copper wires, reflecting the size confinement on the stick-slip motion of the contact line. A copper wire of larger diameter has a larger influential zone than that for a smaller copper wire. For the same distance of the contact line to the copper wire center, the confinement to the motion of the contact line for the "wire-on-film" system with a copper wire of larger diameter limits the motion of the

contact line and allows a smaller slipping distance between two adjacent “stick” states. Additional, the roughness of the interface due to the accumulation of the polymer and the vertical surface tension at the contact line can also affect the wavelength. In general, the evolving tendency of the wavelength of the stripes is determined by a combined effect of the nominal contact angle influenced by the copper wire and the roughness at the interface.

As mentioned, the formation of the surface stripes on the PMMA films is controlled by the accumulation of polymer around the edge of the contact line at the “stick” state. The penetration of toluene into the PMMA films across the interface between the toluene and the film led to the formation of a soft, flowable polymer layer, which was swiped inward by the contact line during the slipping motion. For a larger slipping distance (wavelength), more flowable PMMA was pushed to the vicinity of the contact line, resulting in a stripe with a larger dimension (*i.e.* width and amplitude). Using linear regression to fit the experimental data as shown in Fig. 4, one obtains the slope of the amplitude verse the wavelength as 8.6×10^{-3}, 13.1×10^{-3} and 15.1×10^{-3} m/ m for the copper wires of 51, 79 and 102 μm in diameter, respectively. The increase of the slope can be attributed to the greater confinement of a copper wire of large diameter to the toluene droplet. From Fig. 4.3, one can note that, for the same wavelength, the distance of the contact line to the copper wire center is larger for the droplet pinned by a large copper wire than that by a small copper wire. A larger copper wire confines more toluene, which causes the formation of a thick, flowable polymer layer at the interface between the toluene and the PMMA film. During the slipping, more PMMA accumulates around the contact line, resulting in the formation of surface stripes of large amplitudes.

Evaporation-induced surface pattern via two parallel copper wires

The process for the formation of the surface patterns *via* two parallel copper wires was recorded by a digital camera (Dino-Lite Pro, Torrance, CA). As shown in Movie S1 in the supporting materials, the toluene droplet at the onset of the evaporation was continuous between the copper wires, and the contact line gradually moved towards the copper wires. When the droplet reached a critical volume which is mainly determined by the copper wire diameter and the distance between two wires (Table S1 in supporting information), it spilts into two "sub-droplets" with the shape of the contact line conforming to the copper wire. Two new contact lines appeared between the copper wires. The new contact lines first moved towards individual copper wires respectively to some distance and then "stuck" to form the first set of "internal" stripes. The region between the first set of the internal stripes is featureless due to the smooth slipping motion of the contact lines. The evaporation behavior of the two "sub-droplets" was similar to that of a droplet pinned by a single copper wire.

In general, there exists an "influential zone" of a copper wire, within which the copper wire confines the evaporation of a droplet and the motion of the contact line, leading to regularly straight polymer stripes. The size of the "influential zone" of a copper wire is mainly determined by the cross-sectional size and the surface characteristics of the copper wire. A copper wire of a larger cross-sectional size tends to have a larger "influential zone. For the copper wires used in this study, the width (perpendicular to the straight stripes) of the "influential zone" is 1297±30 μm for 51μm copper wire, 1560±29 μm for 79μm copper wire and 2255±36 μm for 102μm copper wire, respectively. When the distance between two parallel wires is small enough, there is an overlap of the individual "influential zones". In the overlap region, it needs more evaporation before the splitting of a droplet two "sub-

droplets" of small volumes and the presence of two contact lines. Less amount of solvent evaporates from the "sub-droplets" of small volumes. There is only a small amount of solvent lost in each "stick-slip" cycle, which results in surface stripes of small amplitudes. When the distance between two wires is large enough, there is no overlap of the "influential zones". The surface patterns formed by using two parallel wires will be the same as those by using a single wire.

The difference of the size of the featureless zone is likely due to the confinement effect of the copper wires. For the droplet confined by large copper wires, the tangential component of the surface tension at the contact line is smaller than that for the droplet confined by small copper wires. The smaller tangential component of the surface tension results in smaller slipping distance for the contact lines to reach the first stick state, i.e. smaller featureless zone.

4.5 Conclusion

In summary, we fabricated the gradient stripe-like patterns on pre-cast PMMA films *via* the evaporation of a pure toluene droplet, which was confined by a single copper wire or two parallel copper wires. Parallel polymer stripes with the gradient of spatial wavelength and amplitude were formed near the copper wire(s) as the contact line underwent a series of "stick-slip" motion. The amplitude of the smooth stripes is a linear function of the spatial wavelength for the experimental conditions used. The slope of amplitude verse spatial wavelength is a function of the wire diameter and the film thickness. For the "wire-on-film" system with two parallel wires, the characteristics of the stripes between the two wires is dependent on the distance between the two wires due to the overlap of the "influential zone", as determined by individual wires. A featureless zone

between two copper wires was formed as a result of the splitting of the droplet confined between two wires into two “sub-droplets” and the slipping motion of the contact lines to the corresponding first stick states. The size of the featureless zone increases linearly with the distance between two copper wires and is a function of the diameter of copper wires, while it is independent of the film thickness.

The microscale stripes might be miniaturized by reducing the dimensions of the template and carefully controlling the evaporation rate. The well-ordered surface patterns formed with the template reported in this study may be applied in electronics, batteries, biomedical devices or other fields.

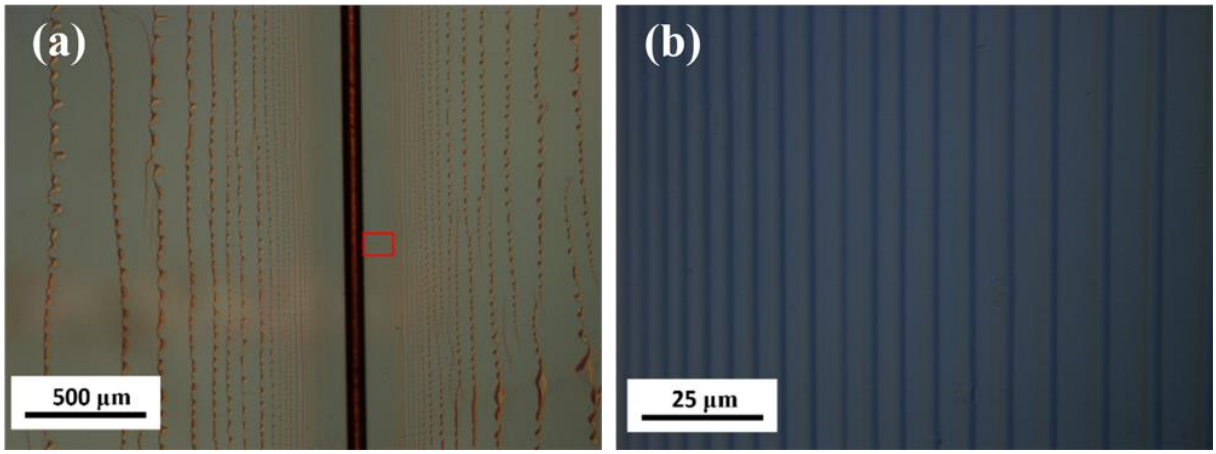

Figure 4.1 Optical images of the evaporation–induced surface patterns; (a) surface pattern formed *vis* a single copper wire, and (b) enlarged view of the surface pattern in the enclosed area in (a) (film thickness: 90 nm; diameter of the copper wire: 79 µm)

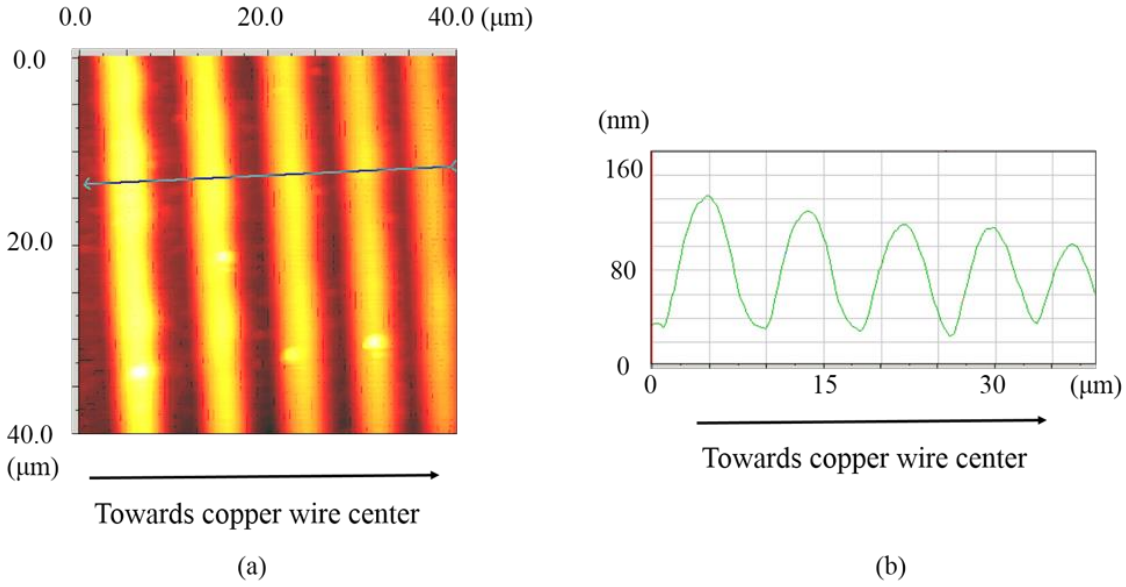

Figure 4.2 (a) An AFM image of the parallel stripes over an area of 40×40 µm^2, and (b) surface profile of the parallel stripes (film thickness: 90 nm; copper wire diameter 79 µm)

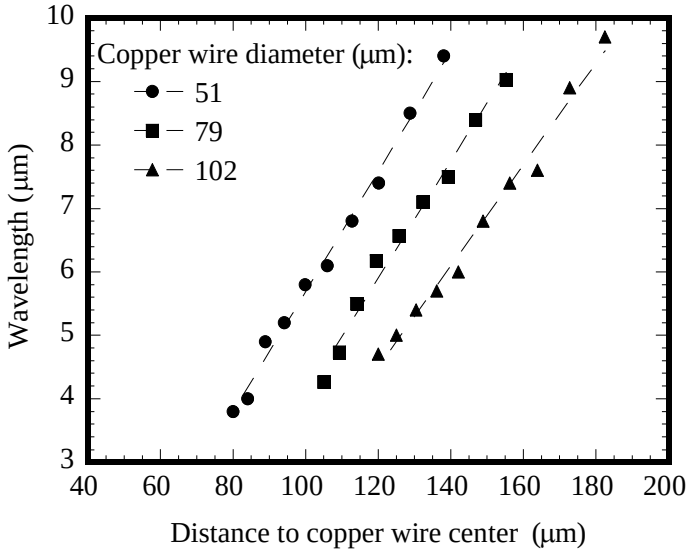

Figure 4.3 Variation of the wavelength of the smooth stripes formed *via* a single copper wire with the distance to the copper wire center for three copper wire diameters (film thickness: 90 nm)

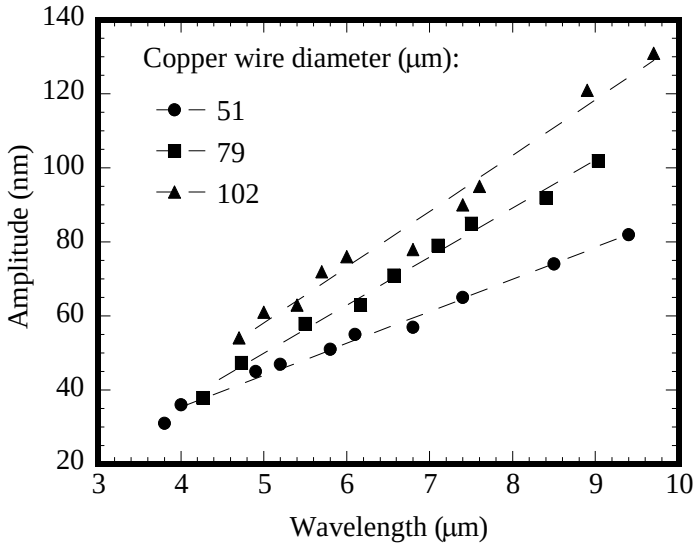

Figure 4.4 Correlation of the spatial wavelength and the amplitude of the smooth stripes formed *via* a single copper wire for three copper wire diameters (film thickness: 90 nm)

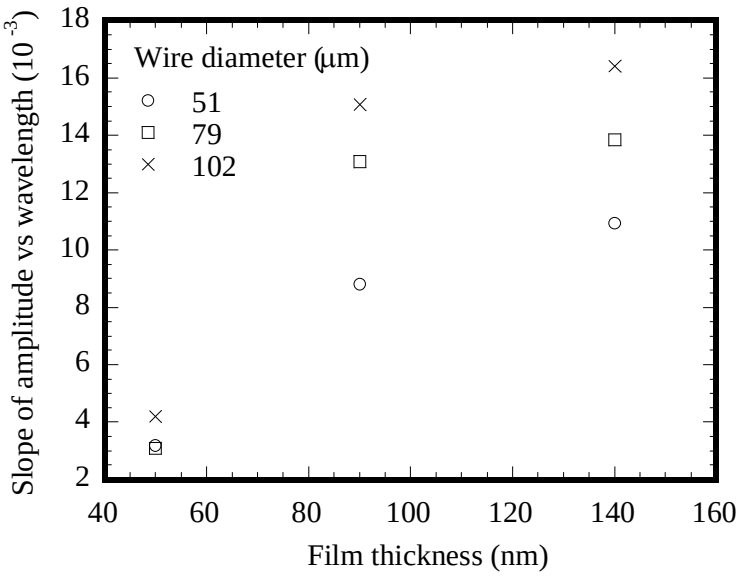

Figure 4.5 Variation of the slope of amplitude verse wavelength of smooth stripes (formed *via* a single copper wire) with film thickness for three wire diameters

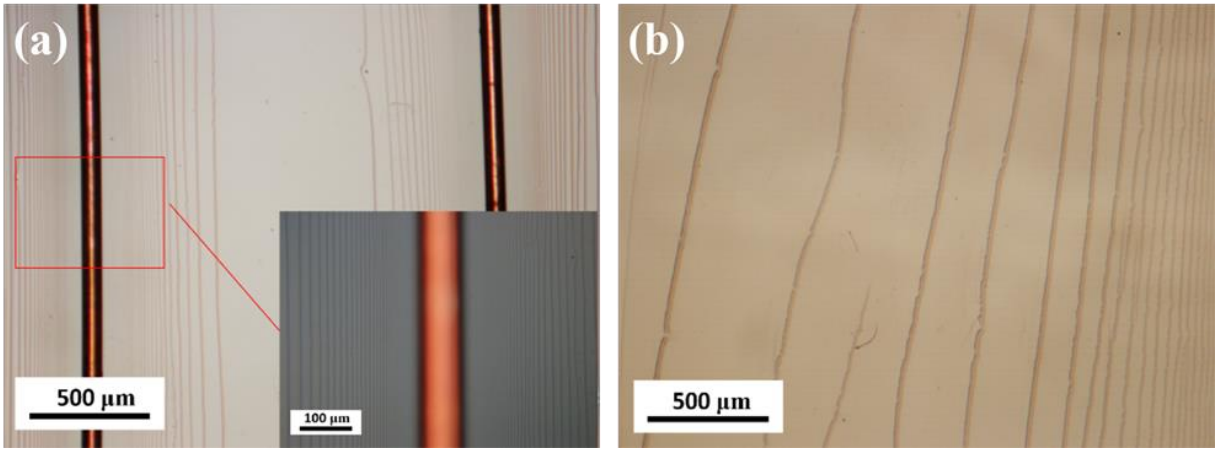

Figure 4.6 (a) Optical images of the evaporation–induced surface patterns formed *via* two parallel copper wires (Inset: enlarged view of the pattern in the rectangular box), and (b) surface patterns far away from the copper wires (film thickness: 90 nm; diameter of the copper wire: 79 mm)

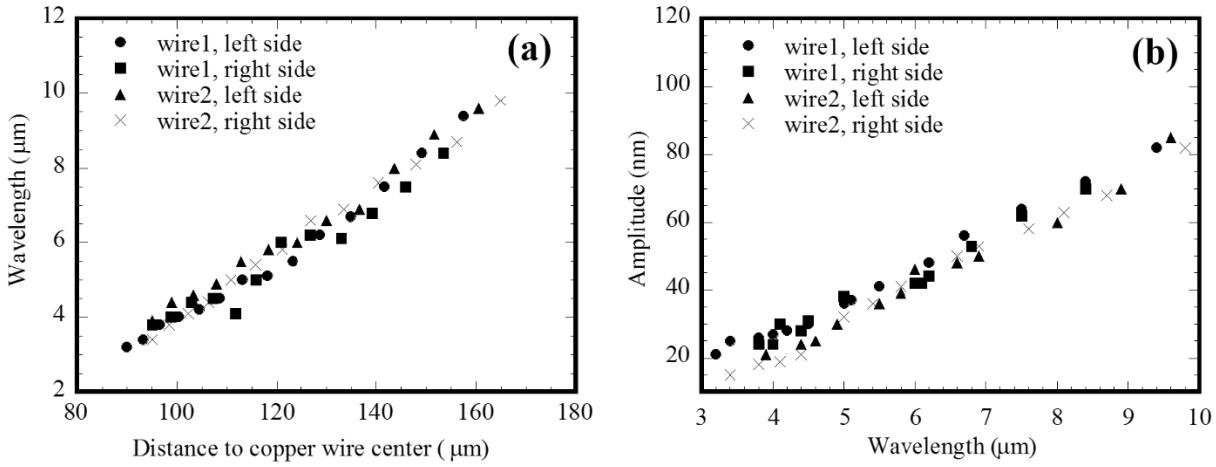

Figure 4.7 (a) Variation of the wavelength of smooth stripes with the distance to individual copper wire centers, and (b) correlation of the amplitude and the wavelength of the smooth stripes formed *via* two copper wires (diameter of the copper wires: 79 μm; distance between two copper wire centers: 1.7 mm; film thickness: 90 nm)

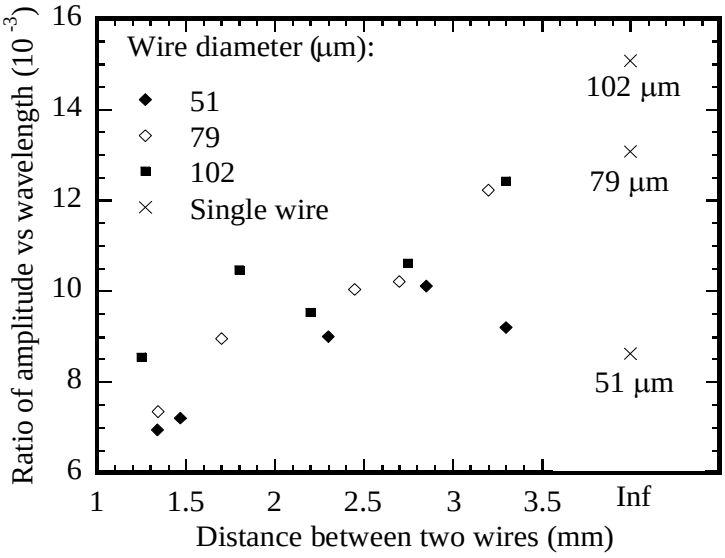

Figure 4.8 Variation of the slope of amplitude verse wavelength with the distance between two copper wires for three copper wires (film thickness: 90 nm)

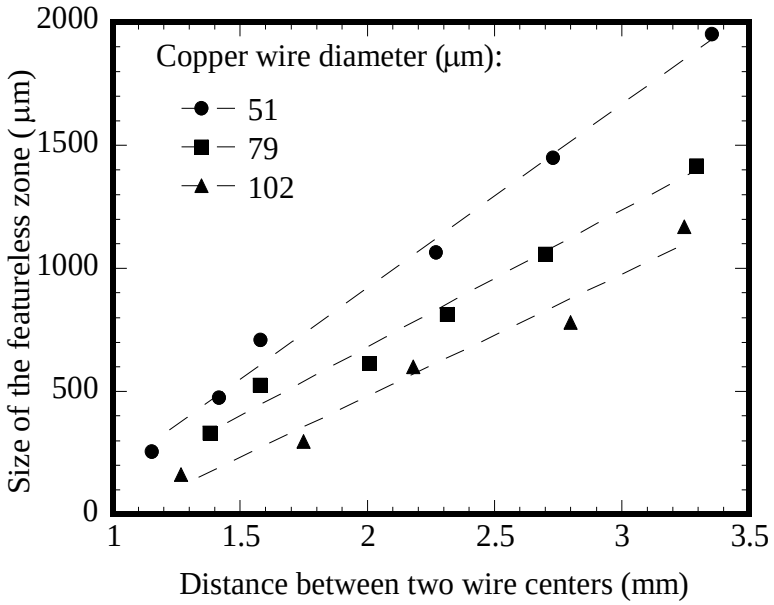

Figure 4.9 Variation of the size of the featureless zone with the distance between two copper wire centers (film thickness: 90 nm)

Chapter 5. Self-organization of unconventional gradient concentric rings with a circular ring as template

5.1 Evaporating a pure solvent droplet on a pre-cast film

5.1.1 Introduction

Evaporation-induced self-assembly has potential to produce high-throughput surface patterns effectively and economically in a simple way. “Coffee ring” is the most typical evaporation-induced surface pattern which is formed at the perimeter of a coffee drop after complete drying.[22] Besides a single “coffee ring”, concentric ring-like patterns that cover a larger area can also be formed when the contact line undergoes several “stick-slip”[9, 158] or “advancing-receding”[50, 51] motion. The shape of the polymer or the particle deposit formed in the vicinity of the contact line is mainly determined by the stick state of the contact line. A circular contact line can lead to the formation of a ring or concentric rings, and a straight contact line can result in multiple straight stripes.[63, 70] However the evaporation-induced surface patterns formed without the evaporation control are usually irregular.[9, 51]

In order to fabricate well-ordered evaporation-induced surface patterns with potential applications, several strategies based on "top-restriction" have been developed. A "sphere-on-flat" geometry composed of a spherical lens and a rigid, flat substrate was used to confine a drop, and well-ordered gradient concentric rings were developed via the confinement of the evaporation by this geometry.[10, 56] Gradient stripes were formed when the spherical lens was replaced by a cylindrical lens.[11, 61, 150] A roll-based evaporation-induced strategy was used to fabricate large-scale stripes via confining a drop between a rolling jig and a flat substrate.[64, 65] Multi-stripes were also constructed when a flat "top restriction" was applied. Through carefully controlling the movement of the top glass plate, one can regulate the evaporation at the edge.[66]

Various materials have been used in forming surface patterns, including homopolymer[23], polymer blend[58], block-copoymer[57], carbon nanotube[60], graphene[64], etc. The effects of solution concentration[23, 66], solvent[9, 69], temperature[20], and electrical field[159] on the surface patterns have also been studied. It was found that the curvature of the contact line has a significant effect on the evolution of surface patterns,[24, 160] while no systematical work has been performed to examine the curvature effect.

As demonstrated in literature, a high quality "top-restriction" is always needed in order to successfully construct well-ordered evaporation-induced surface patterns. There are reports on the evaporation behavior and the evaporation-induced surface morphology on dissolvable substrates.[9, 161-165] None of them has demonstrated the formation of well-ordered concentric rings on a dissolvable substrate.

In this study, we develop a simple "ring-on-film" method to fabricate regular evaporation-induced surface patterns without using the "top-restriction". In our system, a

simple copper wire ring is placed on a pre-cast PMMA film to confine the motion of a pure toluene droplet, which allows the evaporation of toluene on the top surface of the droplet. The principle controlling the formation of surface structures on the pre-cast PMMA films in our "ring-on-film" systems involves the softening of the pre-cast polymer film via pure solvent and the evaporation of the solvent. This approach is in contrast to the evaporation of a polymer solution droplet or a particle suspension droplet on a non-dissolvable substrate, which has been widely used in most studies for surface patterning.[23, 25, 71, 148] Unconventional gradient concentric rings are formed both outside and inside the copper ring after evaporation. The effects of curvature and film thickness on the characteristics of the patterns formed are examined.

5.1.2 Experimental section

PMMA (Mw=3500) (Fisher Scientific, Pittsburgh, PA) film was spin-coated on glass slides (15×20×1 mm^3), using a spin coater (WS-400B-6NPP/LITE, Laurell Technologies Corp., North Wales, PA). The solvent for the spin coating was toluene (Fisher Scientific, Pittsburgh, PA), and the spinning rate was 2000 rpm. The film thickness was adjusted in the range of 50 nm to 140 nm by controlling the PMMA concentration of the solution in the range of 0.5 wt% to 2 wt%. Copper rings served as the templates were made of a bare copper wire of 79 □m in diameter (40 AWG) (ARCOR, Northbrook, IL). The copper rings were ultrasonically cleaned in an acetone bath and dried before being placed on the surface of the PMMA film.

To construct the evaporation-induced surface patterns, a copper ring was carefully placed on a spin-coated PMMA film, and a toluene droplet of 10μL was placed on the film with the copper ring at the center. The copper ring pinned the toluene droplet and limited

the motion of the droplet. The droplet was evaporated at 25 ℃. It took less than 3 min for the droplet to completely evaporate from the film. The surface morphology was characterized by an optical microscope (Nikon ECLIPSE LV100POL) and an atomic force microscope (Q-scope 250, Agoura Hills, CA). The characteristics of the surface patterns were analyzed with Image Pro and the AFM software. The effect of the copper ring was studied by using copper rings of different diameters (1425μm, 2360μm, 2900μm and 3750μm), and the surface patterns formed on the films of different thicknesses (50 nm, 90 nm and 140 nm) were investigated.

5.1.3 Results and discussion

Figure 5.1 shows the typical surface patterns formed on a pre-cast PMMA film of 140 nm via the evaporation of a toluene droplet with a copper ring of 1425 μm in diameter as a template. The copper ring was made from a copper wire of 79 □m in diameter. Concentric rings were formed inside and outside the copper ring. Some less regular polymer rings with "branches" can be observed outside the copper ring in the region relatively far from the copper ring, as shown in Fig. 5.1a. The polymer rings formed near the copper ring are more regular, as shown in Fig. 5.1b. Outside the copper ring, the diameter of the PMMA rings gradually decreases with as the rings approach the copper ring. Inside the copper ring, the diameter of the PMMA rings gradually increases with as the rings approach the copper ring, and there is a featureless zone formed right at the center.

At the onset of the evaporation, there was only one external contact line outside the copper ring, which gradually moved towards the copper ring. As the evaporation continued, the droplet inside the copper ring reached a critical volume and an internal circular contact line inside the copper ring appeared due to the evaporation-induced dewetting. The internal

circular contact line enlarged smoothly and reached the first "stick" state to form the first (smallest) internal PMMA ring. As the evaporation continued, the internal contact line continuously enlarged in a "stick-slip" mode, similar to the external contact line, resulting in the formation of concentric rings both inside and outside the copper ring.

The evaporation-induced formation of the concentric rings is likely controlled by the stick-slip motion of the contact lines inside and outside the copper ring. The toluene diffuses into the PMMA layer and forms a flowable PMMA film at the interface between the toluene and the PMMA layer. The flowable PMMA film moves with the motion of the contact line and accumulates in the vicinity of the contact line. This trend eventually leads to the occurrence of the "stick" state of the contact line when the driving force for the motion of the contact line is balanced by the friction force. With continuous evaporation, the contact angle at the contact line decreases and the driving force for the motion of the contact line becomes larger than the friction force. The contact line starts to move and reaches to the next "stick" state. It is worth mentioning that the "stick" state is a dynamically equilibrium state and there exists local flow and deformation around the contact line at the "stick" state.

From Fig. 5.1b, one can note that the wavelength (distance between the centers of adjacent rings) of both the internal and external concentric rings decreases as the distance to the copper wire decreases. For the rings outside the copper ring, the rings of larger sizes which are far away from the copper ring have greater wavelength than those of smaller sizes closer to the copper ring. This behavior is similar to the gradient rings formed by using the "sphere-on-flat" geometry.[56] On the other side, the internal rings displayed opposite trend. For the rings inside the copper ring, the rings of smaller sizes which are far

away from the copper ring have greater wavelength than those of larger sizes closer to the copper ring. The wavelength gradient can be clearly observed in a very small region, as shown in Figs.5.1c and 5.1d. The polymer rings outside the copper ring have different wavelengths from those inside the copper ring for the same distances to the copper wire, which can be attributed to the curvature effect.

Figure 5.2 shows the AFM images and line scans of the concentric rings formed inside and outside a 2360 μm copper ring on a PMMA film of 140 nm. Over a scanning area of 40×40 μm^2, the arcs of individual concentric rings appear parallel. Drawing a line perpendicular to the arcs, one can determine the wavelength (the distance between the centers of adjacent rings) and the amplitude of the arcs. It can be noted that both the wavelength and amplitude decreases with the decrease of the distance to the copper ring in accord with the observation as shown in Figs. 1c and 1d. The gradient concentric rings are asymmetric with reference to the copper ring. Such behavior is due to the curvature effect, which will be discussed below.

Figures 5.3 shows the variation of the wavelength of both the internal and external PMMA rings with the distance to the copper ring for copper rings of four different sizes. The film thickness is 140 nm. For the rings outside the copper rings, the wavelength increases approximately linearly with the increase of the distance to the copper ring, while there is a deviation from the linear dependence for the concentric rings formed near the copper ring of 3750 μm diameter, when the distance to the copper ring is less than 100 μm. This unusual phenomenon is not found in the cases of the rings of diameters larger than 3750μm, either. The reason for such behavior is unclear, which may be due to sudden

disturbance on the evaporation. The wavelength is also dependent on the diameter of the copper ring. For the approximately same distance to the copper ring, the copper ring of larger size produced the PMMA ring of smaller wavelength than that of smaller size. For the rings inside the copper rings, the wavelength increases approximately linearly with the increase of the distance to the copper ring, similar to those outside the copper rings. No deviation from the linear dependence is observable, and the difference between the wavelengths formed by using the copper rings of four different sizes is not as large as that between the wavelengths of the rings formed outside the copper rings. All of the results suggest that there exist the curvature effect. The size of the copper rings (curvature) has less effect on the wavelength of the gradient PMMA rings inside the copper ring than that of the gradient PMMA rings outside the copper ring.

The difference between the wavelengths of the gradient PMMA rings outside and inside the copper rings is likely related to the curvature effect. The curvature of the contact line outside the copper wire is positive; on the other hand, the curvature of the contact line inside the copper wire. From the experimental results shown in Fig. 3, the positive curvature tends to lead to form the gradient rings of larger wavelength that the negative curvature for the same distance to the copper ring. With the increase of the size of the copper ring, the curvature effect become less significant, leading to smaller difference between the wavelengths of the concentric rings outside and inside the copper ring.

Figure 5.4 shows the dependence of the amplitude of the gradient concentric rings on the wavelength outside and inside the copper ring. The gradient concentric rings were formed on a PMMA film of 140 nm via a copper ring of 2360 □m in diameter. The amplitude increases linearly with the increase of the wavelength, and the PMMA rings

outside the copper have larger slope that those inside the copper rings. Generally, the dimension of the PMMA rings is determined by the amount of the polymer accumulated around the vicinity of the contact line at the "stick" state, which is controlled by the slipping process of the contact line. During the slipping, the soft, flowable polymer film at the PMMA-toluene interface was swiped by the contact line. For a larger slipping distance (wavelength), more flowable PMMA was pushed to the vicinity of the contact line at the "stick" state, resulting in a PMMA ring with a larger dimension (*i.e.* width and amplitude).

The dependence of the slope of the amplitude to the wavelength on the diameter of the copper rings is depicted in Fig. 5.5 for the gradient rings formed on the PMMA films of 90 nm in thickness. For comparison, the slope for the gradient strips formed by using a single straight copper of 79 μm in diameter is also included in Fig. 5.5. The slope of the amplitude to the wavelength for the concentric rings formed outside the copper ring decreases with the increase of the diameter of the copper rings, while the slope of the amplitude to the wavelength for the concentric rings formed inside the copper ring increases with the increase of the diameter of the copper rings. Both approach to the slope of the gradient stripes with the increase of the diameter of the copper ring; the value of the slope of the gradient stripes is always less than those of the gradient concentric rings formed outside the copper rings and larger than those formed inside the copper rings. Such behavior is likely due to the curvature effect. The contact line of positive curvature can have larger slipping distance than that with negative curvature, which leads to larger slope of the amplitude to the wavelength for the gradient rings formed outside the copper ring. There exists asymmetric motion of the contact lines inside and outside the copper ring.

The effect of the film thickness on the formation of the gradient concentric rings was investigated on pre-cast PMMA films with thicknesses of 50, 90 and 140 nm. A copper ring of 1425 μm in diameter was used for the surface patterning. Figure 5.6 shows the variation of the wavelength with the distance to the copper ring for the PMMA rings outside and inside the copper ring for three film thicknesses. Linear dependence of the wavelength on the distance is observed, independent of the film thickness and the rings inside and outside the copper ring. For the same distance to the copper ring, the wavelength increases with the increase of the film thickness, especially significant for the concentric rings formed outside the copper ring on the thickest film. Such behavior is likely due to the less resistance to the slipping of the contact line on a thick PMMA film.

It is known that the driving force for the motion of a contact line is controlled by the difference of the tangential components of the surface tensions at the contact lines, which is a function of the contact angle. The resistance to the motion of the contact line is determined by local deformation[154, 166] and flow of the soft, flowable PMMA film at the toluene-PMMA interface and the film thickness. Thicker PMMA layers lead to the formation of the soft, flowable PMMA film of larger thickness at the toluene-PMMA interface, which reduces the resistance to the motion of the contact line. For the same driving force, the contact line experiences larger slipping distance for the PMMA film of larger thickness, as shown in Fig. 5.6.

Linear dependence of the amplitude on the wavelength for the gradient concentric PMMA rings formed on films of three thicknesses are also observed. Figure 5.7 shows the variation of the slope of the amplitude to the wavelength with the film thickness for the rings outside and inside the copper ring of 1425 μm in diameter. The slope of the amplitude

to the wavelength decreases with the decrease of the film thickness for both the concentric rings inside and outside the copper rings. Such behavior suggests that the geometrical characteristics of the gradient concentric rings depend on the film thickness. More soft, flowable PMMA is available to form concentric rings when a thick PMMA film is used in constructing the gradient concentric rings on the film.

As discussed above, the evaporation leads to the occurrence of dewetting inside the copper ring and the formation and motion of the contact line. The slipping motion of the contact line inside the copper ring to the first "stick" state resulted in the formation of a circular featureless zone at the center of the copper ring. The continuous motion of the contact line in the featureless zone can be attributed to the small contact angle in this zone due to the good wettability of the toluene to PMMA and negligible influence from the copper ring. The small contact angle leads to a relatively large tangential surface tension towards the copper ring which drives the contact line to move smoothly in this zone. Figure 5.8 shows the dependence of the size of the featureless zone on the diameter of the copper ring for three PMMA film thicknesses. The size of the featureless zone increases linearly with the increase of the size of the copper ring, and the film thickness has little effect on the size of the featureless zone for the experimental conditions. The thickness of the residual film in the featureless zone is found to be uniform. There are no significant differences of the thickness of the residual film at different positions R (normalized distance to the center of the featureless zone by the radius of the featureless zone) of the featureless zone. For example, for the patterns formed with a copper ring of 3750μm in diameter, the thickness of the residual film is 70nm at R=0, 72nm at R=0.5 and 69nm at R=0.75. The mechanism behind the uniform distribution of the thickness of the residual

film is unclear, which may be related to the competition on the soft layer between the moving contact line and the glass substrate. The average thicknesses of the residual film in the featureless zone of the patterns formed with a 3750μm copper ring are 71.3±2.3nm for 140nm pre-cast film, 44.3±0.9nm for 90nm pre-cast film and 19.5±1.3nm for 50nm pre-cast film.

As discussed above, both the size of copper ring and the film thickness can affect the gradient concentric rings. By combining these two factors, the features of the concentric rings may be flexible controlled. In order to better understand the fundamental knowledge of the gradient concentric rings and combining effect of the size of copper ring and film thickness on the features of the concentric rings, more reproducible experiments will be will be done in the future. For example, the study of film thickness effect will be extended to all different copper ring sizes, and both these two factors will be investigated in a wider range.

Besides the factors we discussed in this study (copper ring size and film thickness), other factors, i.e. temperature, solvent and etc. also significantly influence the formation and features of the evaporation-induced surface pattern, which have been investigated by other studies.[9, 167] In the system of this study, the features of the "template ring" is another important factor that determine the surface patterns. The size effect of the "template ring" on the surface patterns is discussed in this study, while the rings composed of different materials can also lead to different surface patterns due to different surface characteristics, i.e. surface roughness and surface tension. The confining effect of the "template ring" to the droplet is decided by the surface characteristics. The size of the "influenced zone", nominal contact angle during the contact line motion and other factors may all changed if

"template ring" of other materials are utilized, resulting in surface patterns of different features. The effect of the surface characteristics of the "template ring" will be studied in future work.

5.1.4 Conclusion

In summary, we constructed gradient concentric rings - on pre-cast PMMA films via the evaporation of a toluene droplet, using a copper ring to pin the droplet without limiting the evaporation of the droplet from its top surface. The evaporation of the toluene droplet inside the copper ring led to the presence of a circular contact line inside the copper ring due to the evaporation-induced dewetting and the formation of a featureless zone. The contact lines experienced a series of "stick-slip" motion, and gradient concentric rings were formed both outside and inside the copper ring. The wavelength and amplitude of the concentric rings decrease with the decrease of the distance to the copper ring. The concentric rings outside the copper ring have positive curvature and have larger wavelength and the ratio of the amplitude to the wavelength than those with negative curvature inside the copper ring. Increasing the size of the copper ring, i.e. decreasing the radius curvature, led to the decrease of the ratio of the amplitude to the wavelength for the concentric rings outside the copper rings and the increase of the ratio of the amplitude to the wavelength for the concentric rings inside the copper rings, which approached that of the gradient stripes formed with a straight copper wire of the same diameter. The slope of the amplitude to the wavelength also decreases with the decrease of the film thickness for both the concentric rings inside and outside the copper rings. All of these results demonstrate the potential of using the "ring-on-film" method to construct gradient concentric rings on polymer films, which can be easily controlled by the ring size and the film thickness.

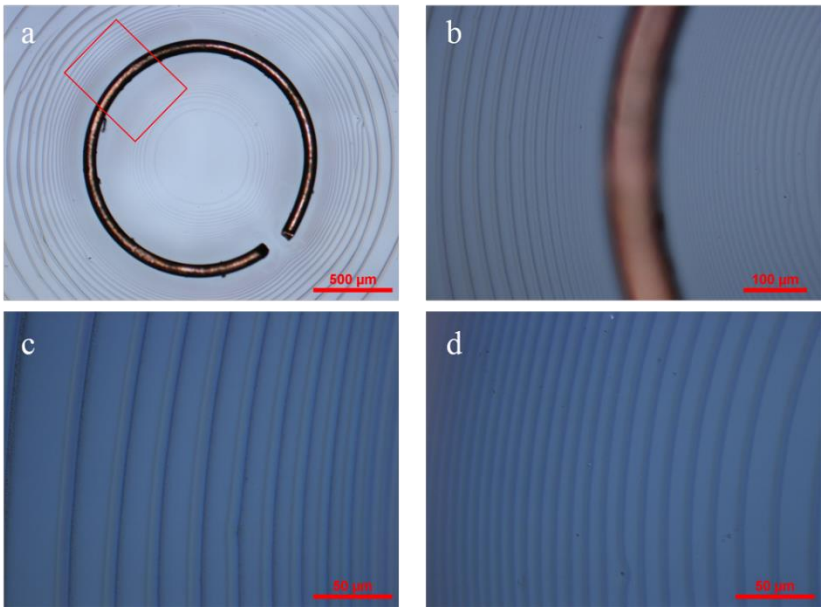

Figure 5.1 Optical images of the evaporation–induced gradient concentric rings on a pre-cast PMMA film (film thickness: 140 nm; diameter of the copper ring: 1425 µm); (a) a large view of the surface pattern, (b) an enlarged view of the surface pattern in the enclosed area in (a), (c) the concentric rings outside the copper ring, and (d) the concentric rings inside the copper ring

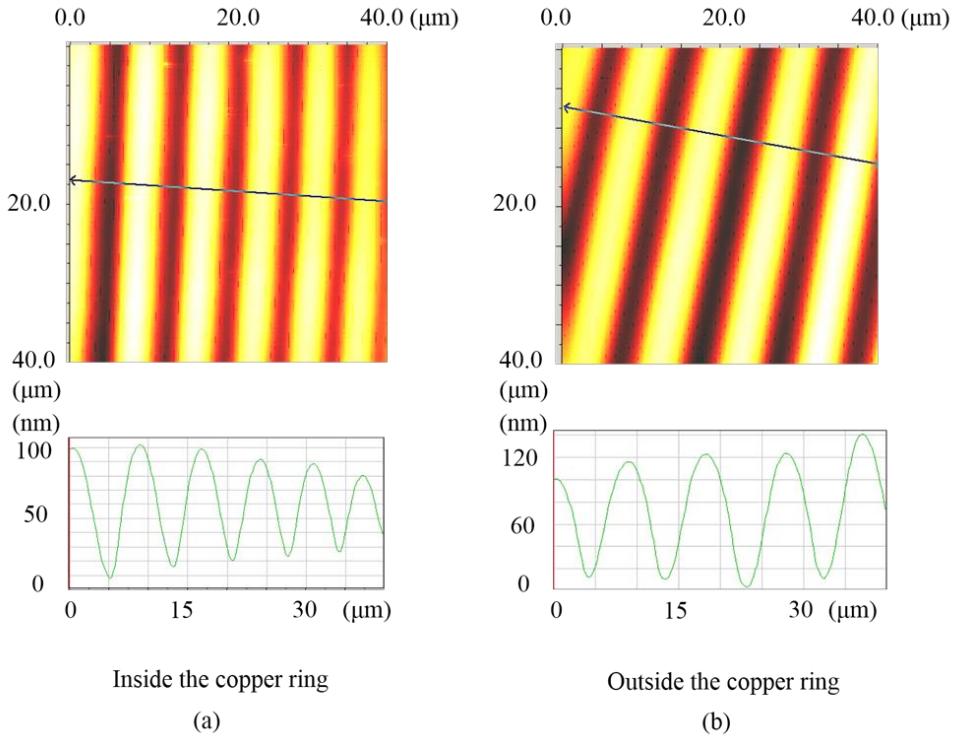

Figure 5.2 AFM images and line scans of the concentric rings nearest to a copper ring over an area of 40×40 μm^2 (film thickness: 140 nm; diameter of the copper ring: 2360 μm); (a) the PMMA rings inside the copper ring, and (b) the PMMA rings outside the copper ring

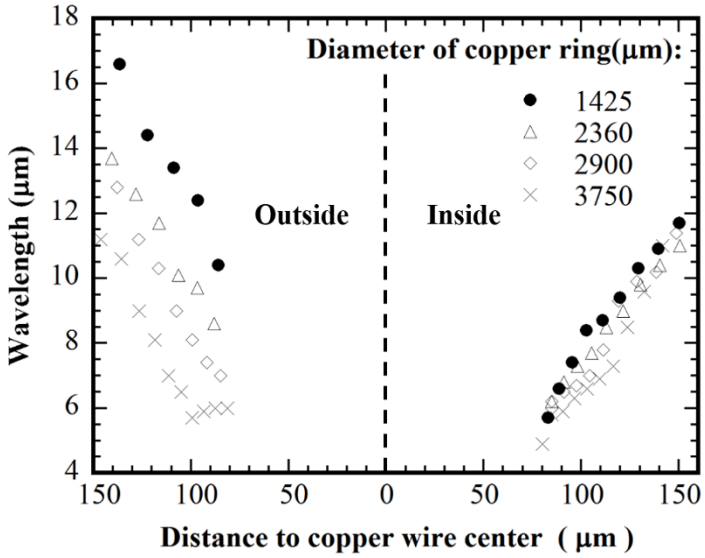

Figure 5.3 Variation of the wavelength of the gradient concentric rings with the distance to the copper ring for copper rings of different diameters (film thickness: 140 nm). “0” in the x-axis refers to the position of the copper wire, and the negative sign refers the positions outside the copper ring.

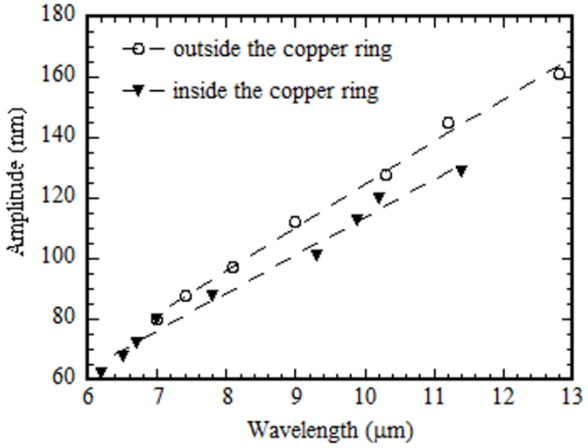

Figure 5.4 Correlation between the amplitude and the wavelength of the concentric rings formed via a copper ring of 2360 μm in diameter (film thickness: 140 nm)

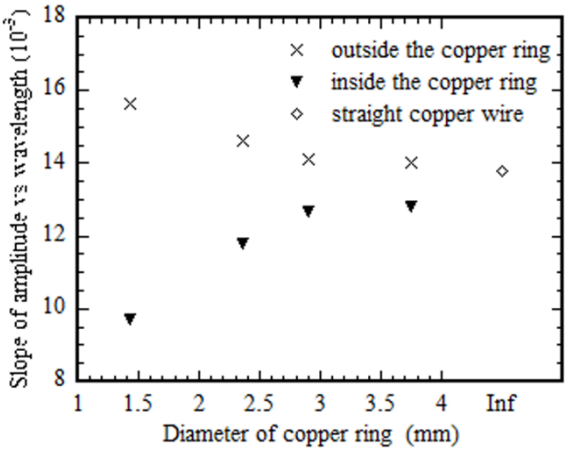

Figure 5.5 Variation of the slope of the amplitude to the wavelength with the size of the copper ring (film thickness: 90 nm)

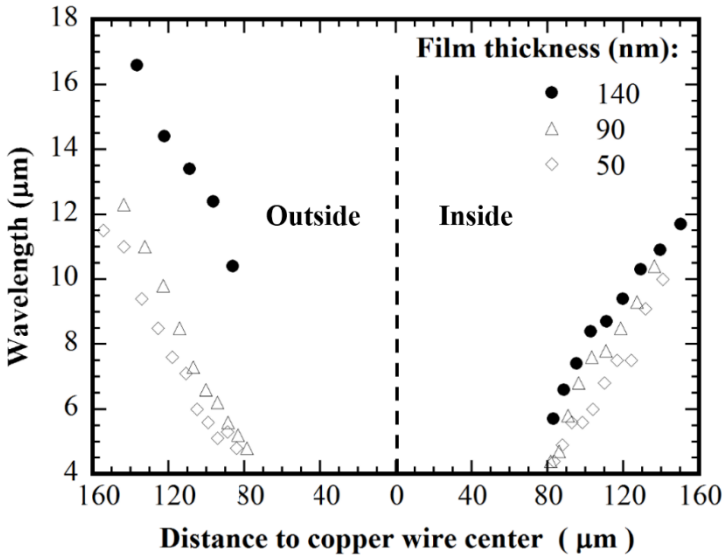

Figure 5.6 Variation of the wavelength with the distance to copper ring (diameter of copper ring: 1425 μm). "0" in the x-axis refers to the position of the copper wire.

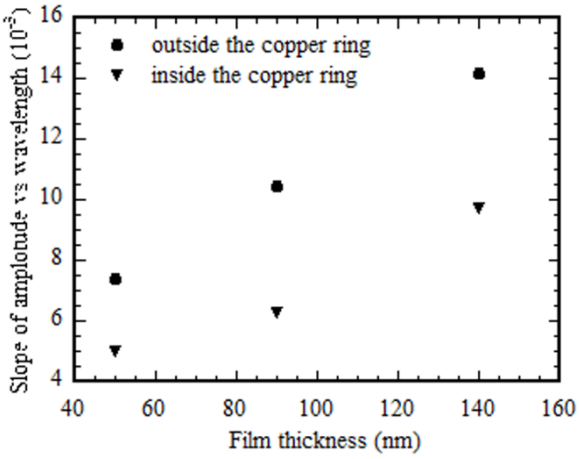

Figure 5.7 Dependence of the slope of the amplitude to the wavelength of the gradient concentric rings on film thickness (diameter of copper ring: 1425 μm)

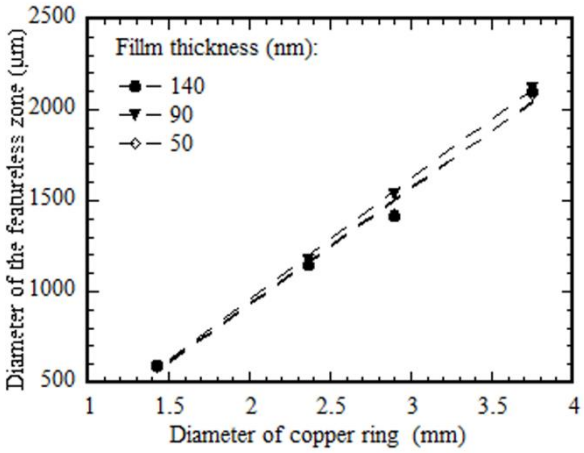

Figure 5.8 Variation of the size of featureless zone with the diameter of copper ring for three film thicknesses

5.2 Evaporating a droplet of polymer solution on a glass substrate

5.2.1 Introduction

Well-ordered surface structures, especially those in the micro and nano scales, have application potentials in various areas, including electronics [12], photonics [2], surface adhesion [5], tissue engineering [4], biomedical devices [3, 16], etc. Various techniques have been developed to fabricate well-ordered surface structure [14, 18, 19, 21, 30, 146], while it is still a great challenge to construct highly-ordered surface structures efficiently and economically. Evaporation-induced surface patterning is an economy-effective method to construct surface patterns. The principle behind the evaporating-induced surface patterning is the "coffee-ring" behavior [24]. When a droplet of a polymer solution or a particle suspension evaporates on a substrate, the non-volatile solute tends to deposit in the vicinity of the contact line as the contact line is pinned [8]. Several templates have been developed to fabricate well-ordered surface structures *via* controlling the evaporation of a solution droplet and the motion of the contact line. Concentric rings with gradients of wavelengths and amplitudes were constructed by confining the evaporation of a solution droplet within a "sphere-on-flat" geometry [10, 56].

Gradient straight stripes also were fabricated by replacing a spherical lens with a wedge or a cylinder [11, 150]. Straight stripes of uniform wavelength were produced by confining a polymer solution film within two parallel glass plates and using a computer system to control the motion of the top glass plate [168]. A "roll-based" system were developed to fabricate parallel stripes over a large area [64]. Various materials have been used to construct surface patterns via the evaporation-induced surface patterning, such as homopolymer [169], polymer blend [58], block copolymer [170], nanoparticles [150], carbon nanowire [171], graphene [64], DNA [151], etc. All of these works demonstrate the potential to meet the requirement of different fields.

To better control the characteristics of surface patterns and understand the formation mechanisms, several effects have been investigated, *i.e.* solution concentration [10, 66], droplet size [22], solvent[9], affinity between solute and substrate [172], curvature of contact line [24, 173], etc. Temperature, which determines the evaporation rate, viscosity and micro-flows inside a droplet, is another important factor. However, there are only limited studies investigating the temperature effect on the evaporation-induced patterns. Bodiguel et al. [174] studied the temperature effect on the pinning and depinning force for the "stick-slip" motion of a liquid film sandwiched between two glass plates. Uchiyama et al. [20] fabricated surface-patterned hybrid films by combining sol-gel process with dip-coating process. They found that the dimensions of the parallel stripe patterns were enlarged significantly when increasing the dip-coating temperature.

In this study, we fabricate concentric ring-like patterns with asymmetric gradients, using a simple copper ring to confine the evaporation of a polymer solution droplet. Well-ordered patterns are formed both inside and outside the copper ring, while the

characteristics of the patterns inside and outside the copper rings are different due to curvature effect. The effects of the solution concentration and the substrate temperature on the characteristics of the surface patterns are examined, and the structures formed in the trenches between two adjacent rings are also analyzed.

5.2.2 Experimental details

Materials

Poly(methyl-meth-acrylate)(PMMA) (Mw=35000) (Fisher Scientific, Pittsburgh, PA) was dissolved in toluene to prepare polymer solutions of different concentrations (0.5, 0.25, 0.125 and 0.063 wt%). The substrate was glass slide ($15 \times 20 \times 1$ mm^3), which was ultrasonically cleaned in an acetone bath for 5 min for 3 times and dried with condensed air. Copper rings of different diameters (3750, 2560 and 1380μm) were made from bare copper wires (38 AWG, 79 μm in cross-sectional diameter) (ARCOR, Northbrook, IL). The copper rings were cleaned with toluene ultrasonically and dried at room temperature.

Sample preparation

A copper ring was carefully placed on the surface of a cleaned glass slide. A solution droplet of 6 μL in volume was then dripped on the glass slide, using a micropipet, with the copper ring approximately at the center. The evaporation of the droplets took place at different substrate temperatures (21, 35 and 55 ℃), which was controlled by placing the substrates on a heating stage. For the evaporation at 21℃, the substrates were not heated. For the experiments at 35 and 55 ℃, the substrates were pre-heated at the pre-set temperature for half hour to reach thermal equilibrium state before the droplet was dripped on the substrate. Note that the solution was also pre-heated to the pre-set temperature before

being dripped on the substrate. During the evaporation, the temperature of the system remained unchanged.

Characterization

The surface patterns formed after complete evaporation of the droplets were characterized, using an optical microscope (Nikon ECLIPSE LV100POL) and an atomic force microscope (Q-scope 250, Agoura Hills, CA). The characteristics of the surface patterns were analyzed, using the AFM software and Image Pro plus.

5.2.3 Results and discussion

Figure 5.9 shows typical optical images of the surface patterns formed *via* the evaporation of a droplet of PMMA-toluene solution with a concentration of 0.25 wt%, using a copper ring of 1380 μm in diameter. From Fig. 1a, one can observe that concentric ring-like patterns were formed both inside and outside the copper ring with an approximately circular-featureless zone in the center. Less regular rings interconnecting with neighbors by "branches" are found outside the copper ring, and the concentric rings inside the copper ring are well ordered. The wavelength of the concentric rings (distance between the centers of adjacent rings) gradually decreases as the PMMA rings approach to the copper ring for both the patterns inside and outside the copper ring. The wavelength gradient is more clearly revealed in Fig. 5.9b and 5.9c. The gradient circular pattern related to the copper ring is not symmetric. For approximately the same distance to the copper ring, the concentric rings inside the copper ring (Fig. 5.9b) exhibit larger wavelengths than the corresponding concentric rings outside the copper ring (Fig. 5.9c).

The concentric rings outside the copper ring were formed due to the typical "stick-slip" motion of the contact line outside the copper ring [58, 59]. The contact line motion can be

considered as the result of the force exerted on the contact line. When the tangential surface tension and the local friction on the contact line reaches force balance, the contact line would be pinned. As the contact line was pinned, the non-volatile PMMA accumulated in the vicinity of the contact line and formed circular ridges. During the pinning, the solvent continues evaporating and the nominal contact angle decreases which increases the force toward the copper ring. When the force is enlarged enough, it would drive the contact line to start to move towards the copper ring again until the next pinning due to the increase of the contact angle.[35] As the repeated "stick-slip" motion, the concentric ring patterns were formed.

When a droplet was deposited on the glass slide, with the evaporation of toluene and the confinement of the copper ring, the solution droplet started to dewet towards the copper ring when a critical volume was reached [29]. The internal dewetting front (the internal contact line newly formed) first receded smoothly to the copper ring until it was pinned. The first pinning produced the smallest internal PMMA ring and formed a featureless zone in the center of the copper ring. Note that the system in this study is different from the "copper ring-on-film" system,[173] in which the patterns were formed due to the flow of the soft, flowable layer between softened pre-cast film and toluene. Here the PMMA is deposited from the solution. The difference of the mechanisms in the pattern formation can also be revealed from the comparison of the formed micro-patterns, as discussed late.

Figure 5.10a shows an AFM image of the concentric rings formed inside a 3750 μm copper ring. The solution concentration was 0.125 wt% PMMA. Locally, the segments of the concentric rings appear parallel. By drawing a line perpendicular to the segments, as shown in Fig. 5.10a, the wavelength and the amplitude of the concentric rings can be

determined. From the line scan in Fig. 5.10a, one notes that both the wavelength and amplitude gradually decreases as the concentric rings approach to the copper ring. Figure 5.10b shows the variation of the amplitude with the wavelength of the concentric rings inside and outside a 3750 μm copper ring for the droplets with a concentration of 0.125 wt% PMMA. The amplitude increases linearly with the increase of the wavelength for both the concentric rings inside and outside the copper ring. The amplitude of a concentric ring is mainly determined by the amount of the non-volatile PMMA deposited during the "stick" state, which can be approximately evaluated by the volume loss of the droplet between two adjacent "stick" states. As schematically illustrated in Fig. 5.9d, P, W and V represent pinning (stick), wavelength and volume change during the stick-slip motion of the contact line, respectively. For two adjacent "stick" states, 1 represents the first pinning state, and 2 is for the second pinning state. From the experimental observation, the polymer ring formed earlier has larger wavelength, so W1 is greater W2. Thus the volume change for the corresponding pinning: V1 is likely to be larger than V2. Assume that the solution concentration remains constant and the deposition during the "slip" motion is negligible. The amount of solute in V1 which deposit in the vicinity of the contact line is greater than that at the following pinning state (P2), resulting in a polymer ring with larger dimensions at P1. Note that for certain wavelengths, the circular rings outside the copper ring have greater amplitudes than the circular rings inside the copper ring and the slope of the linear-fitting of the amplitude *verse* the wavelength for the external concentric rings is slightly larger than that of the internal concentric rings. This asymmetric feature can be attributed to the curvature effect.

Curvature effect

Figure 5.11 shows the variation of the wavelength with the distance to copper ring for copper rings of different diameters. The concentration of the PMMA solution was 0.125 wt% PMMA, and the substrate temperature was 21 ℃. From Fig. 5.11, one can note that the wavelength of the concentric rings outside the copper ring decreases approximately linearly with the decrease of the distance to the copper ring for all the three copper rings. For the approximately same distance to the copper ring, the concentric rings formed via a smaller copper ring have larger wavelengths than the concentric rings formed via a larger copper ring, which indicates the curvature effect on the slipping motion of the contact line. For the concentric rings inside the copper ring, the wavelength also decreases with the decrease of the distance to copper ring. There is no significant difference among the concentric rings formed via different copper rings. This result suggests that the curvature effect is more significant for the concentric rings formed outside the copper rings.

According to Fig. 5.11, one notes that the external concentric rings have greater wavelengths than the corresponding internal concentric rings with the approximately same distance to the copper ring. This result suggests that there exists a curvature effect on the slipping motion of the contact lines and the formation of the PMMA rings; the portion of the droplet outside the copper ring (positive curvature) will form concentric rings of larger wavelengths than that inside the copper ring (negative curvature) due to the difference in the confinement to the evaporation of the PMMA-toluene droplet.

Concentration effect

Figure 5.12 shows the variation of the wavelength with the distance to copper ring for four solution concentrations. The diameter of the copper ring was 1380 μm. The evaporation took place at a temperature of 21 ℃. The wavelengths of both the internal and

external concentric rings decreases with the decrease of the distance to the copper ring, independent of the solution concentration, and the external rings have larger wavelengths than the internal rings for the approximately same distance to copper ring. For the approximately same distance to the copper ring, the wavelength increases with increasing the solution concentration for both the internal and external concentric rings.

Consider the contact line at a "stick" state. The contact angle gradually decreases due to the evaporation of toluene, and the contact line begins to move to the next "stick" position when the contact angle decreases to a critical value.[175] The critical contact angle is determined by the geometrical confinement of the copper ring and the solution concentration. For the same copper ring and the same distance to the copper ring, the geometrical confinement can be approximated as the same. For a solution droplet with a high concentration, the contact line experiences high resistance to the de-pinning and slipping motion due to the interaction with a PMMA ridge of large size and a high viscosity of the solution. The local solution concentration can be expected to increase with the increase of the concentration of the bulk droplet, as more polymer could deposit for a solution with higher concentration. A increasing tendency of the local viscosity with the increase of the solution concentration can be inferred based on the equation: $\frac{(\eta-\eta_0)}{\eta_0 c} = [\eta] + k'[\eta]^2 c$, where η is the viscosity of the polymer solution, η_0 is the viscosity of the solvent, $[\eta]$ is intrinsic viscosity which describes the contribution of an individual polymer molecule to the solution viscosity, k' is Huggins slope constant which is a constant for a given "polymer-solvent" system and c is the concentration of the solution.[176] As a result, the resistance to the contact line is increased, and more evaporative volume loss of toluene is needed to reduce the contact angle and initiate the slipping motion of the contact line,

which leads to a smaller critical contact angle [175] and a larger tangential force for the slipping motion of the contact line. The large tangential force is able to drive the contact line to move a greater distance in the slip state than that with a lower concentration.[177]

As shown above, the amplitude is a linear function of the wavelength for the experimental conditions used. The dependence of the slope of the amplitude to the wavelength on the solution concentration is depicted in Fig. 5.13 for the concentric rings formed with three copper ring diameters. The slope of the amplitude to the wavelength increases with the increase of the solution concentration for both the concentric rings inside and outside the copper ring, regardless of the diameters of copper rings. The slope is closely related to the amount of PMMA in droplets. For droplets with the same initial volume, there are more PMMA in a droplet of a higher concentration which are available to form a concentric ridge of larger dimensions near the contact line at a "stick" state for the approximately same slipping distance. Also, a solution of a higher concentration has a higher viscosity, which produces higher viscous resistance to the motion of the contact line and increases the pinning time of the contact line for the deposition of more PMMA.

Figure 5.13 also demonstrates the curvature effect. For the same solution concentration, the slope of the amplitude to the wavelength increases with the increase of the diameter of copper rings for the internal concentric rings, while it decreases with the increase of the diameter of copper rings for the external concentric rings.

Temperature effect

Figure 5.14 shows the variation of the wavelength with the distance to the copper ring of a diameter 1380 μm for the concentric rings formed at different substrate temperatures. The solution concentration was 0.125 wt% PMMA. For the same distance to the copper

ring, the wavelength increases with increasing the substrate temperature for both the concentric rings inside and outside the copper ring. Such behavior is due to the temperature dependence of the evaporation rate and the solution viscosity. As discussed above, the decrease of the contact angle due to the evaporation introduces the force imbalance on the contact line, leading to the receding of the contact line. During the “slipping” process, the contact angle gradually increases due to the droplet geometry and reaches another “stick” state when the resultant tangential force becomes zero. The evaporation rate increases with temperature, while the solution viscosity decreases with temperature. At a higher temperature, the faster evaporation reduces the time to reach the critical contact angle for the onset of slip motion and also reduces the increasing rate of the contact angle during slipping motion, resulting in a larger driving force for the receding. Moreover, the smaller solution viscosity reduces the viscous resistance to the motion of the contact line. Thus, the contact line can travel a longer distance before reaching the next pinning (“stick”) state at higher temperatures.

Figure 5.15 shows the variation of the slope of the amplitude to the wavelength with the substrate temperature for the concentric rings formed inside and outside the copper rings of three diameters. For all the three copper rings, the slope of the amplitude to the wavelength of both the internal and external concentric rings decreases with the increase of the substrate temperature. This trend suggests that the evaporation temperature plays an important role in controlling the geometrical dimensions of the concentric rings through the control of the evaporation rate and the solution viscosity. The total evaporation time of a solution droplet of 6 μL reduced significantly from 180 s at 21 ℃ to 110 s at 55 ℃. One expects that the pinning time of the contact line also decreases with the increase of the

evaporation temperature. Thus, less amount of PMMA was deposited during the "stick" state at a higher substrate temperature for the droplets of the same geometries, and concentric rings of smaller amplitudes were formed.

In addition, thermal Marangoni flow [178, 179] also contributes to the temperature dependence of the dimensions of the concentric rings. The temperature gradient between the dewetting front of a thin liquid film and the top of the film is more profound at a higher substrate temperature than at a lower temperature. This thermal gradient induces an inner circular flow inside the droplet and causes more solute to move from the contact line back to the droplet, resulting in less deposition of solute. [69]

We may also take into account the effect of polymer diffusion in the droplet on the dimensions of the polymer ridges. Due to the geometry of the droplet and non-uniform evaporation along the droplet surface, a concentration gradient is induced. In the droplet, the polymer is expected to diffuse from the vicinity of the contact line (high local concentration) to the buck droplet (low local concentration) thermodynamically, which means the self-diffusion has an effect of reducing the amount of the polymer deposition at the contact line. The polymer coils in dilute solutions are separated without overlapping, which can be considered as molecule-scale sphere. The threshold of the overlapping can be defined in terms of polymer fraction by the equation: $\Phi^* = N^{-\frac{4}{5}}$, where N is the degree of polymerization.[180] For the PMMA used in this study, the degree of polymerization is about 350, and the overlapping threshold for this PMMA is about 0.009. The solution concentrations used in this study in terms of the polymer fraction is in the order of 10^{-4}, much less than the overlapping threshold 0.009, so we consider the solution in this part of study as dilute solution, in which the polymer coil existing as separated particles. Assuming

the polymer solution with low Reynold's number, Stokes-Einstein equation is applied to describe the relations between diffusion coefficient, viscosity and temperature: $D = \frac{k_B T}{6\pi\eta r}$, where D is diffusion coefficient, k_B is Boltzmann's constant, η is the viscosity of the medium, r is the radius of the spherical particle and T is absolute temperature. [181] The viscosity of the medium (toluene) decreases with the increase of the temperature from 0.554 mpa·s at 298K, 0.458 mpa·s at 315K to 0.375 mpa·s at 335K. [182] Ignoring the size change of the "polymer sphere", the diffusion coefficient is expected to increase with temperature based on Stokes-Einstein equation, which means the polymer tends to diffuse from the contact line to the buck droplet faster at higher temperature than lower temperature. This phenomenon may partially contribute to the decrease of the amplitude of the polymer ridge with the increase of the temperature.

Structures in the trenches between two adjacent rings

From Fig. 5.10a, one notes that the trenches between two polymer rings are not featureless. There exist small islands in the trenches. Figure 5.16 shows typical AFM images of the microscale structures at three different trenches formed at three different substrate temperatures. The diameter of the copper ring was 1380 μm. Figures 5.16a-c show the typical structures in the trenches formed at a substrate temperature of 21 ℃. At a wavelength of 15 μm, both isolated and interconnected islands can be observed (Fig. 5.16a). With the increase of the wavelength to 20 μm, the size of the islands increases (Fig. 5.16b), and the islands become interconnected and a network was formed at a wavelength of 25 μm (Fig. 5.16c).

At a substrate temperature of 35 ℃, large interconnected islands can be found, and the

size of the islands increases with the wavelength and become a continuous film with some larger holes (Fig. 5.16f). At a substrate temperature of 55 ℃, a continuous film with non-uniform holes can be found even for a wavelength of 15 μm (Fig. 5.16g). The number of the holes significantly decreases for a wavelength of 20 μm (Fig. 5.16h). A uniform film without any holes can be found in the trench for a wavelength of 25 μm (Fig. 5.16i). It is worth mentioning that there is no significant difference between the microscale structures in the trenches inside and outside the copper ring.

For comparison, the microscale structures formed in the trenches between two adjacent rings *via* the evaporation of a pure toluene droplet on a pre-cast PMMA film are shown in Fig. 5.16j-l. The film thickness was ~90 nm, the diameter of the copper ring was 1380 μm, and the substrate temperature was 21 ℃. In contrast to the microscale structures formed via the evaporation of the PMMA-toluene droplet, multiple individual holes of micron sizes were formed in the trenches. The hole size does not change with the wavelength significantly. Such behavior is similar to the etching pits formed on the surface of crystalline metals during chemical etching, which reveals the presence of local defects (weak points). The local defects allow the penetration of more toluene locally into the PMMA film, results in the formation of holes after complete evaporation. Note that there are a few larger holes in the trenches for small wavelength of 15 μm (Fig. 5.16j).

The area fraction of the islands or the continuous film as a function of the wavelength for three substrate temperatures is shown in Fig. 5.17. The area fraction increases with the increase of the wavelength, suggesting that there are fewer holes over larger trenches for all the three temperatures. For the same wavelength, the area fraction also increases with the increase of the substrate temperature due to easier flow of the solution at a higher

temperature.

Note that the height of the islands (or the depth of holes in the continuous film) does not exhibit significant change with the wavelength. They are 27.6±1.9, 34.2±2.4, and 45.4±2.7 nm for the substrate temperatures of 21, 35, and 55℃, respectively; the height of the islands (or the depth of holes) increases with the increase of the substrate temperature.

The formation of the microscale structures in the trenches is likely due to the deposition of PMMA and the accumulation of "large" amount of toluene during the "slipping" stage. The variation of the dimensions of the microscale structures might be explained from the aspect of the competition between the polymer motion and the motion of the contact line. At room temperature, the evaporation rate is relatively low, the rate of the polymer motion inside a droplet is compatible with the evaporation rate and only a small portion of the polymer directly deposits on the substrate during the "slipping" stage. At a higher temperature, the evaporation rate is significantly high; the contact line recedes to the copper ring at a much faster speed. The liquid film near the contact line might be very thin, leading to a high local viscosity. Thus the polymer may experience a larger resistance and is difficult to keep pace with the motion of the contact line, which results in non-uniform deposition of polymer during the "slipping" stage. Similar situation occurs for the microscale structures formed between the rings of different wavelengths at the same substrate temperature. The evaporation rate is higher and the wavelength is larger when the droplet size is larger. Thus the microscale structures covering a larger area are formed in the wider trenches. It is worth mentioning that we cannot measure the velocity of the contact line in the small scale and the moving rate of PMMA chains in the thin liquid film near the contact line due to the high receding rate of the contact line during the "slipping"

process.

It needs to point out that the evaporation behavior at the same wavelength is different for different substrate temperatures due to the differences in the distance to the copper ring, viscosity and evaporation rate. Comparing the micro-structures formed with the same distance to copper ring, one can note the difference. For example, for the distance to the copper ring being 160 μm, from Fig. 6, one can find the wavelength inside the copper ring is about 15 μm at 21 ℃, 19 μm (approximately being 20 μm) at 35 ℃ and 25 μm at 55 ℃, respectively. Comparing the micro-structures as shown in Fig. 5.16 for the corresponding conditions, one can observe significant differences for different substrate temperatures. Moreover, according to Fig. 5.17, there is an increasing tendency of the area fraction of the micro-structures with the substrate temperature for the same distance to the copper ring.

If considering the microscale patterns as defects, some methods might be applied to reduce their formation. Based on the results and discussions above, the polymer seems to cover more areas in the trench with a higher local viscosity during the contact line slipping. So we may increase the viscosity by increasing the evaporation rate or solution concentration, if a thin polymer film is desired. Conversely, the opposite experimental conditions should be applied to obtain pure glass surface in the trenches. Moreover, the wetting properties between the polymer, solvent and the substrate surface also play an important role in the formation of the microscale structures. When the polymer does not wet the substrate surface, it tends to dewet with the solvent, leaving nothing in the trench. Contact angle can be changed by choosing different substrate and solvent. An increasing contact angle is expected to slow down the contact line motion, as a result of which the polymer might be able to keep pace with the contact line motion and does not deposit in

the trenches. In addition, the dust or other contamination could pin small polymer droplet during the contact line motion, leading to patterns formed in the trenches, so it is important to keep the substrate clean. Note that all the possible changes mentioned above, might cause surface patterns with different dimensional characteristics (wavelength and amplitude) or even different types of the patterns.

Patterns formed without template

Without a template to control the evaporation of the droplet of polymer solution, only irregular patterns can be formed. Figure 5.18 shows the patterns formed on clean glass slides by evaporating a PMMA solution droplet without any templates for different solution concentrations. The substrate temperature is 21 ℃. Only one nearly circular polymer ridge was formed for 0.5wt%, 0.25wt% and 0.125wt% solution. However multiple ring-like patterns can be constructed when the solution concentration is reduced to 0.063wt% (Fig. 5.18 d, e). There is an increase of the width of the outermost polymer ring with the concentration of the solution. Without a copper ring to control the evaporation, there is only one typical "pinning" process during the whole lifetime of the droplet for relatively high solution concentrations (0.125wt% or higher) due to high viscosity, and almost all the polymer deposits during the pinning which further increases the pinning force. For the dilute solution, the contact line is able to overcome the first pinning in a relatively shorter time and only a portion of the polymer is deposited, and other polymer is deposited during the following several pinning stages.

Figure 5.19 shows the patterns formed by evaporating a ~0.125wt% solution droplet on a glass slide without any template at different substrate temperatures. As mentioned above, at 21℃, only one polymer ring was formed, while the number of the polymer rings

increases as the substrate temperature increases to 35℃and 55℃. The multiple ring-like patterns formed at higher substrate temperatures is a result of “stick-slip” motions due to higher evaporation rate and lower viscosity. Comparing the irregular patterns formed without a template and the controllable concentric ring patterns formed with a copper ring, one can notice that the template plays important role in the fabrication of the regular patterns.

5.2.4 Conclusion

In summary, we fabricated concentric ring patterns via the evaporation of a droplet of the PMMA-toluene solution by using a copper ring to control the evaporative behavior and the motion of the contact line. Concentric rings were formed both inside and outside the copper ring with a featureless zone in the center. Both the wavelength and amplitude of the concentric rings inside and outside the copper ring decrease with decreasing the distance to the copper ring. There exists the curvature effect, which made the surface structure asymmetric with respect to the copper ring. Both the wavelength and the ratio of the amplitude to the wavelength increase with increasing the solution concentration.

The substrate temperature played an important role in controlling the formation of the concentric rings. Higher substrate temperature led to the formation of concentric rings of larger wavelengths and smaller ratio of the amplitude to the wavelength for the inner concentric rings. Microscale structures were formed in the trenches between adjacent polymer ridges, whose geometric characteristics were dependent on the wavelength of the concentric rings and the substrate temperature. The technique presented in this study has the potential to fabricate well-ordered concentric ring patterns, whose characteristics can be simply controlled in an effective and economic method. Besides the factors we focused

in this study, other factors may also be used to control the characteristics of the patterns formed by this strategy. For example, the diameter of the copper wire, the choice of the solvent, molecular weight of the polymer and surface properties of the substrate, etc. More investigation on these factors will be done to make the surface patterns more controllable.

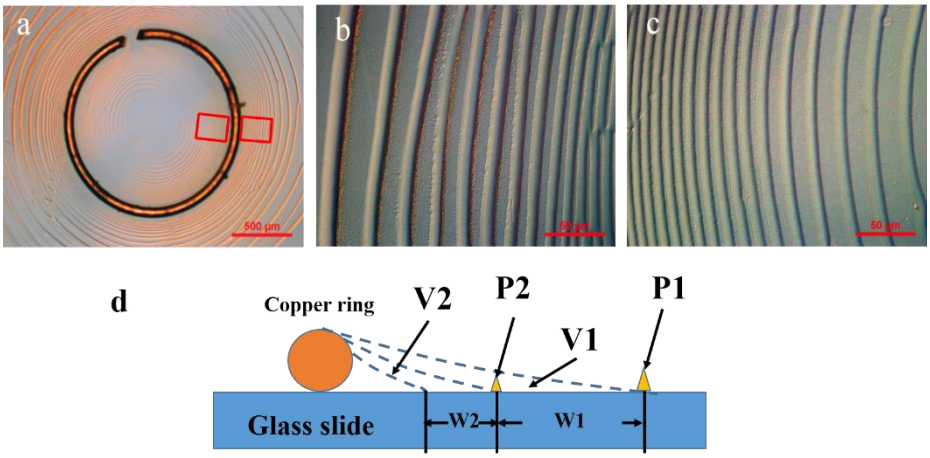

Figure 5.9 Typical optical images of the concentric rings formed with a copper ring *via* the evaporation of a PMMA solution droplet (copper ring diameter: 1380 μm, solution concentration: 0.25 wt%, substrate temperature: 21 ℃). (a) a large view of the surface pattern, (b) an enlarged view of the concentric rings near the copper ring formed outside the copper ring, (c) an enlarged view of the concentric rings near the copper ring formed inside the copper ring, and (d) schematic of the formation of the PMMA rings.

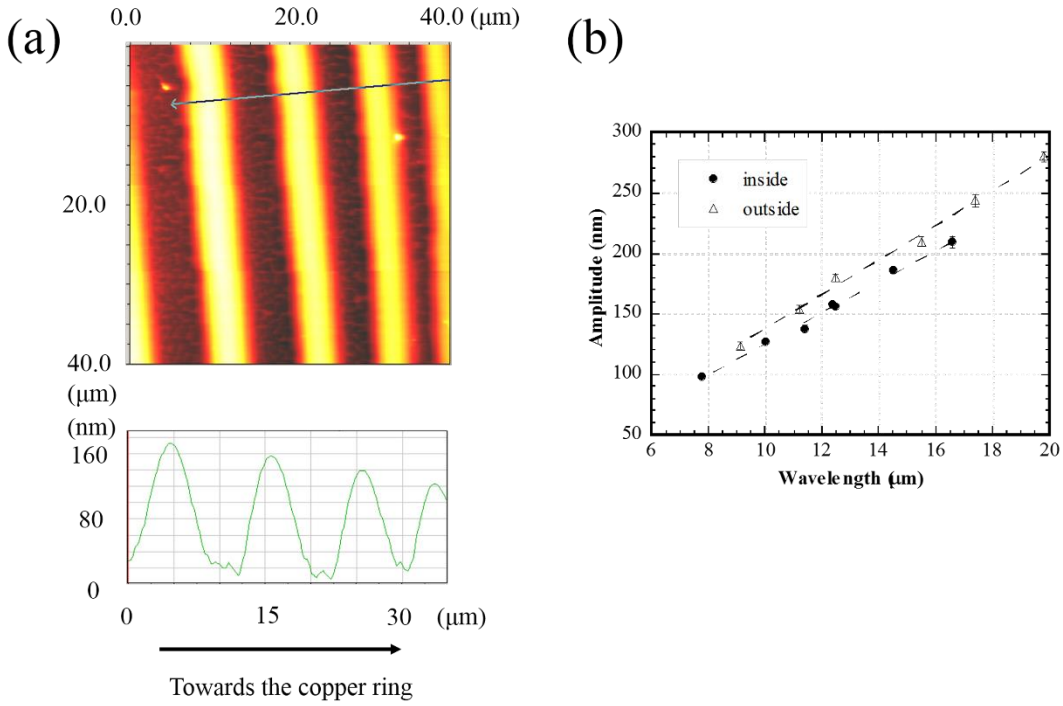

Figure 5.10 (a) A typical AFM image of the concentric rings formed inside a copper ring; (b) correlation between the amplitude and the wavelength of the concentric rings formed both inside and outside the copper ring (copper ring diameter: 3750 μm, solution concentration: 0.125 wt%, substrate temperature: 21 ℃)

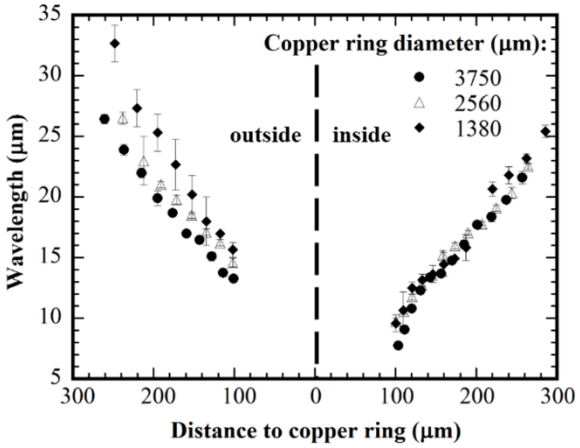

Figure 5.11 Variation of wavelength with the distance to copper ring for both the concentric rings inside and outside the copper ring for different ring diameter (solution concentration: 0.125 wt%PMMA; substrate temperature: 21 ℃)

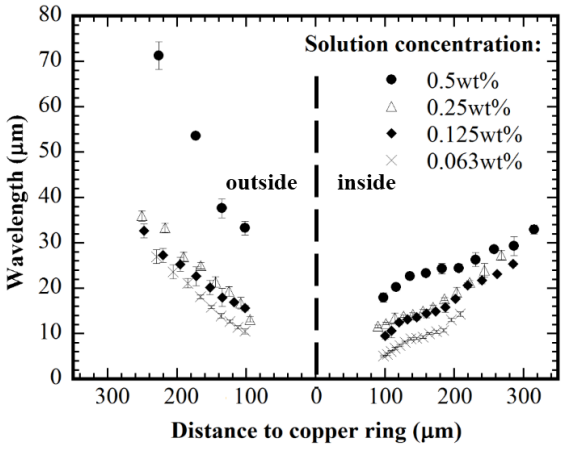

Figure 5.12 Variation of wavelength with the distance to copper ring for four solution concentrations (copper ring diameter: 1380 μm, substrate temperature: 21 ℃)

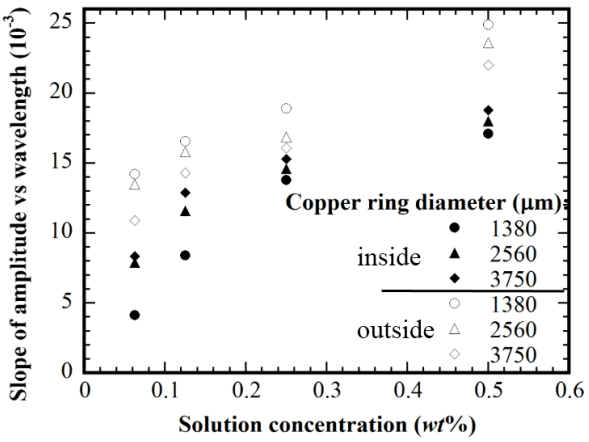

Figure 5.13 Variation of the slope of the amplitude to the wavelength with the solution concentration (substrate temperature: 21 ℃)

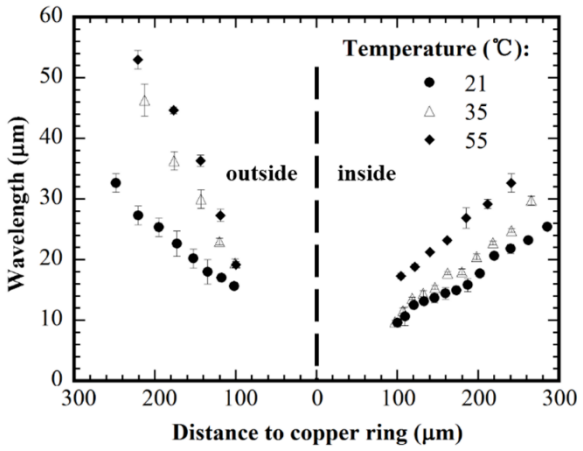

Figure 5.14 Variation of wavelength with the distance to copper ring for the concentric rings formed at different substrate temperatures (solution concentration: 0.125wt% PMMA; copper ring diameter: 1380 μm)

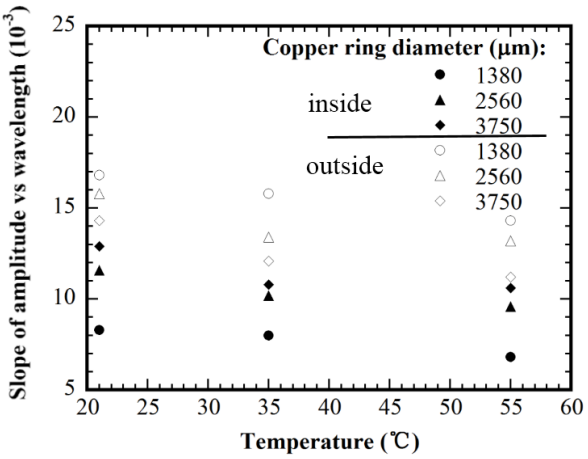

Figure 5.15 Variation of the slope of the amplitude to the wavelength with the substrate temperature (solution concentration: 0.125 wt% PMMA)

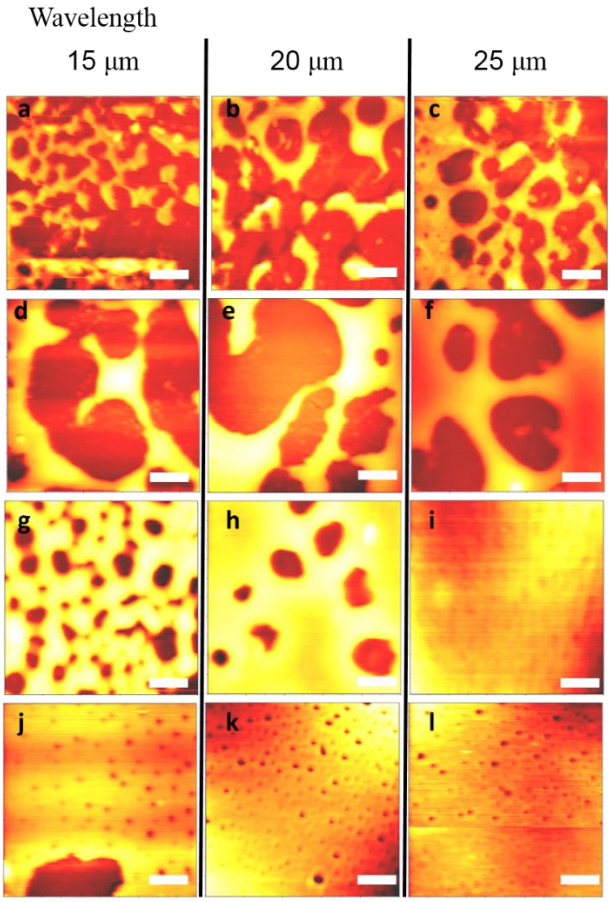

Figure 5.16 AFM images (5×5 μm^2) of the patterns formed in the trenches between two adjacent rings at different substrate temperatures (solution concentration: 0.125 wt% PMMA, copper ring diameter: 1380 μm): (a-c) 21℃, (d-f) 35℃, (g-i) 55℃; (j-l) patterns in the trenches between two adjacent rings *via* the evaporation of a pure toluene droplet on a pre-cast PMMA film (film thickness: ~90 nm, copper ring diameter: 1380 μm, substrate temperature: 21 ℃). The scale bars in all the images represent 1μm

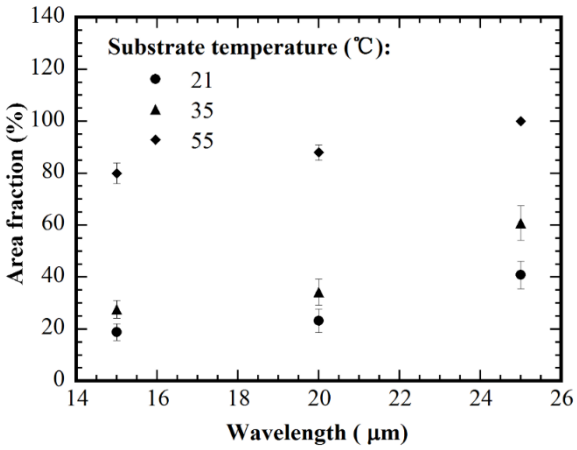

Figure 5.17 Variation of the area fraction of the island patterns in the trenches between two polymer ridges with the wavelength of the concentric rings at three substrate temperatures. (solution concentration: 0.125 wt% PMMA, copper ring diameter: 1380 μm)

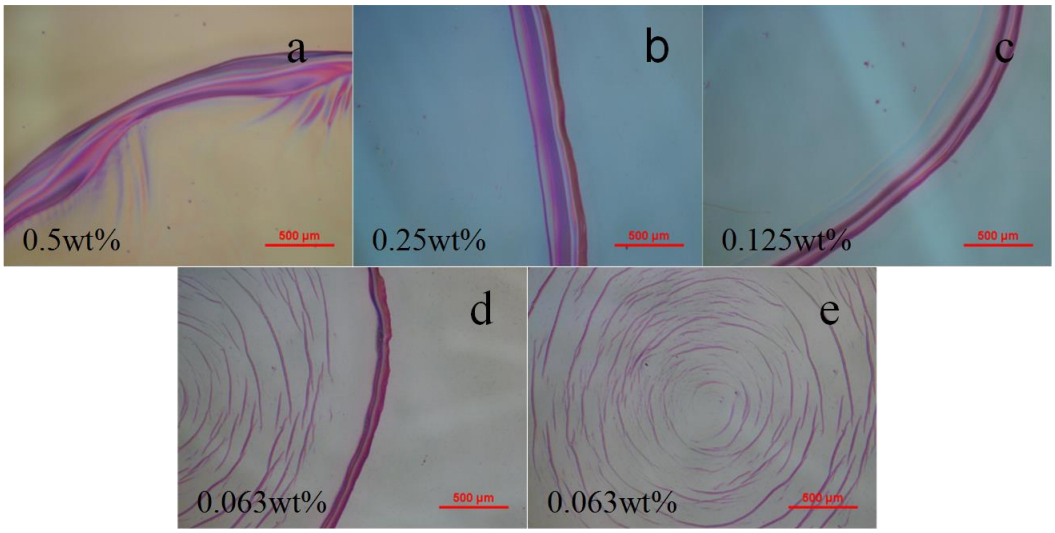

Figure 5.18 Optical images of the patterns formed by evaporating a droplet of PMMA solution in toluene on a glass slide without templates. Solution concentrations: (a) 0.1wt%, (b) 0.25 wt%, (c) 0.125wt% and (d, e) 0.063wt%. Substrate template is 21℃.

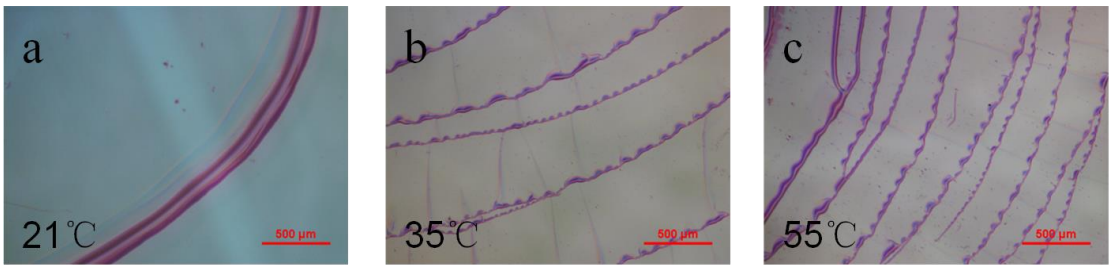

Figure 5.19 Optical images of the patterns formed by evaporating a droplet of PMMA solution in toluene on a glass slide without templates at different substrate temperatures: (a) 21℃, (b) 35℃ and (C) 55℃. Solution concentration is 0.125wt%.

Chapter 6. Formation of well-ordered finger-like structures on pre-cast thin films

6.1 Introduction

Evaporation-induced self-assembly has been studied for a long time.[1] The principle for this phenomenon is so-called "coffee-ring" effect,[24] in which the non-volatile solute in a droplet gradually accumulates in the vicinity of the contact line and forms a ridge with the shape conforming to the contact line. If the contact line moves discontinuously in a "stick-slip" mode, multiple ridges covering a larger area may be formed.[9, 50, 183] The topology of the evaporation-induced surface patterns(concentric rings,[56] parallel rings,[184] parallel straight stripes,[66] concentric triangles[171] and etc.)are determined by the shape of the corresponding contact line. Various highly-ordered evaporation-induced patterns can be formed if the evaporation of the droplet can be controlled by using some templates. Gradient concentric rings consisting of various materials have been fabricated via a "sphere-on-flat" template[10], and concentric triangles have been formed by replacing the "spherical lens" with a "triangular pyramid".[171] Surface structure of multi-straight stripes is another typical "coffee-ring" pattern, which have been constructed via a "cylinder-on-flat" template [150] or a "wedge-on-flat"[61] template to maintain a straight contact line. Straight stripes have also been formed in a dip-coating process.[20]

To fabricate parallel stripes covering a large area, a "roll-based" system [64, 65], a "computer-controlled" system[66], and an "inkjet printing-based" process[67] have been developed. Recently, Sun and Yang[185-187] developed "particle-on-film", "ring-on-film", and "wire-on-film" templates to produce gradient concentric rings and gradient stripes on pre-cast thin polymer films. There is no report to demonstrate the formation of well-ordered finger-like structures.

In this report, we demonstrate the formation of well-ordered finger-like structures on pre-cast poly(methyl methacrylate) (PMMA) films for the first time. A pure toluene droplet is confined between a tilt carbon rod and a pre-cast PMMA film to limit the evaporation of the droplet and the motion of the contact line. A gradient finger-like structure consisting of multiple arc-segments and line-segments is formed. The geometric characteristics of the gradient finger-like structures are characterized, and the effects of the droplet volume and the tilt angle of the rod are examined. A template consisting of four tilt perpendicular carbon rods is developed to construct a "cross" pattern of four finger-like structures.

6.2 Experimental section

PMMA (Mw=35000) (Fisher Scientific, Pittsburgh, PA) thin films were spin-coated on slides (15×20×1 mm^3), using a spin-coater (WS-400B-6NPP/LITE, Laurell Technologies Corp., North Wales, PA). The glass slides were cleaned in an acetone bath ultrasonically for 10 min for three times and dried by condensed air. The solvent for the spin-coating was toluene (Fisher Scientific, Pittsburgh, PA), and the solution concentration was 1 wt%. The spinning speed was 2000 rpm. The film thickness was 90 nm which was measured by an atomic force microscope (AFM) (Q-scope 250, Agoura Hills, CA). Carbon rods (PENC25HB, 500 μm in cross-sectional diameter, and 10 cm in length) (Pentel of America, Ltd, Torrance, CA) were cleaned ultrasonically in toluene and dried in ambient environment.

Figure 6.1a shows the schematic of the experimental set-up. One end of a carbon rod was in contact with one edge of a glass slide (1 mm in thickness) at point A and the other end was supported by a glass plate (3 mm in thickness). A droplet of toluene was placed carefully near the point A, and a finger-like droplet was formed between the carbon rod and the PMMA film. The droplet was evaporated at 22 ℃. To examine the effect of tilt angle, a droplet volume of 5 μL was used, and the angles between the carbon rod and the glass substrate were 5.71°, 3.81°, 2.86° and 2.29° by varying the horizontal distance between the two contact points from 20 mm to 50 mm. To study the effect of the droplet volume on the characteristics of surface patterns, the tilt angle of 2.86° was used, and the volumes of toluene droplets were 5, 10, 15 and 20 μL.

To construct “cross” surface patterns, four tilt carbon rods were placed on a polymer film with the lower ends of all the four rods being in contact with the polymer film at the same point and each rod being perpendicular to adjacent rods. Two cases were studied. The first one had a tilt angle of 2.86° for all four rods, and for the other one, the tilt angles of the four rods were 5.71°, 5.71°, 2.86° and 2.29°, respectively. The volume of toluene droplets was 10 μL, which was placed at the “common” contact point on the PMMA film.

The characteristics of the surface patterns formed after the complete evaporation of a toluene droplet was analyzed, using an optical microscope (Nikon ECLIPSE LV100POL) and a digital camera (Dino-Lite Pro, Torrance, CA).

6.2.1 Results and Discussions

When a droplet was placed near the point A, shown in Fig. 6.1a, a liquid bridge between the carbon rod and the PMMA film was formed due to the capillary effect. A contact line on the surface of the PMMA film formed due to the pinning effect. The contact line consisted of an arc segment and two straight segments. The geometric characteristics of the contact line are dependent on the tilt angle and the droplet volume. Receding motion of the contact line towards to the point A occurred due to the evaporation of the droplet, which led to the formation of finger-like patterns on the surface of the PMMA film.

Figures 6.1b-d show the finger-like surface patterns at three different positions indicated in Fig. 1a. The film thickness was 90 nm, the droplet volume was 5μL, and the tilt angle is 2.86°.Near the tip of the finger-like patterns (Fig. 6.1b), the patterns consisted of only multiple arc-segments with the two end points of each segment being at the outmost edge of the finger, i.e. the first contact line formed after placing the droplet. In the intermediate region (Fig. 6.1c), the patterns consisted of multiple arc-segments and straight

line-segment with each arc-segment smoothly connecting with two straight line-segments (Fig. S1b and S1c).In the rear region of the finger-like surface structures (Fig. 6.1d), the widths of the arc-segments (the distance between two endpoints) decreased and approached the diameter of the carbon rod. There is a featureless zone near the point A.

The formation of the finger-like surface pattern is controlled by the motion of the contact line first formed on the PMMA film (the outmost edge of the finger consisting of an arc-segment and two straight line-segments) after placing a droplet. The toluene droplet softened the pre-cast PMMA film and a softened, flowable layer was formed at the interface of the toluene and PMMA film. As the toluene evaporated, the contact line started to recede which pulled the softened polymer near the contact line to move inside and accumulate near the contact line. When the contact line was pinned (stick), a polymer ridge was formed. During the whole evaporation process, the contact line experienced a series of "stick-slip" motion and multiple polymer ridges were formed. The receding stick-slip motion of the arc-segment results in the formation of multiple nearly parallel arc-ridges in the middle, and the receding stick-slip motion of the line-segments of the contact line leads to the formation of straight-parallel ridges. The moving rate of the arc-segment of the contact line is higher than that of the line-segments. Thus, several arc-segments converged into the same straight line-segment (Fig. S1a and S1b). Also, local Rayleigh–Taylor instability at the dynamic "stick" state introduced bead-like shape of the outmost contact line (Fig. S1a-d). With continuous evaporation, less local instability occurred and smooth finger-like ridges were formed. More details of the formation of the evaporation-induced surface patterns on pre-cast film are discussed in our previous work.[16]

Figure 6.2 shows the variation of the dimensions of the outmost finger-like pattern with

the droplet volume and the tilt angle of the carbon rod. For a given tilt angle, both the length and width of the outmost finger-like pattern increase with the increase of the droplet volume, since a toluene droplet of a large volume can spread over a large surface area of a PMMA film. For a given droplet volume, the length of the outmost finger-like pattern decreases with the increase of the tilt angle, while the width increases with the increase of the tilt angle. For a small tilt angle, more toluene is confined between the carbon rod and the PMMA film to form a longer liquid bridge, leading to the formation of a thinner and longer finger-like ridge.

The distance to the finger tip of the outmost finger-like ridge along the symmetric axis is normalized by the total length of the outmost finger-like ridge. Define wavelength as the distance between two adjacent arc-ridges along the symmetric axis. Figure 6.3a shows the variation of the wavelength with the normalized distance for different droplet volumes. The normalized distance is schematically illustrated in Fig.6.1. The normalized distance is 0 at the fingertip and 1 at the rear of the finger. The variation of the wavelength with the non-normalized distance to fingertip can be found in Fig.S2. As shown in Fig.6.3a, the wavelength first decreases with the increase of the normalized distance, reaches minimum when the normalized distance is about 0.52, and then increases with the increase of the normalized distance for all the four different droplet volumes. The increase rate of the wavelength is relatively higher than the decrease rate. Moreover, a larger droplet generally created surface patterns of larger wavelengths that a smaller droplet for the same normalized distance. Such behavior is likely due to less resistance to the motion of the contact line for a droplet of a larger volume. Figures 6.2b and 6.2c show the comparison of the multiple arc-ridges of the finger-like patterns formed on the PMMA films of 90 nm

thickness with the droplet volumes of 10 and 5μL, respectively, at a normalized distance of 0.5. The tilt angle was 2.86°. Over the same imaging area, a droplet of 5μL volume produced more arc-ridges than a droplet of 10μL volume, indicating that a droplet of a larger volume produced a larger average wavelength for the same normalized distance.

Figure 6.4a shows the variation of the wavelength with normalized distance for four tilt angles. The droplet volume was 5μL. The variation of the wavelength with non-normalized distance to the finger tip is shown in Fig. S3. The wavelength is relatively independent on the tilt angle for the normalized distance less than or equal to 0.35. The normalized distance, at which the wavelength reaches the minimum, increases with decreasing the tile angle due to the confinement effect of the rod on the evaporation of the toluene droplet. The normalized distances corresponding to the minimum wavelengths are 0.43, 0.49, 0.52, and 0.57 for the tilt angles of 5.71°, 3.81°, 2.86° and 2.29°, respectively. After the wavelength reached minimum, a larger tilt angle led to the formation of the surface patterns with larger wavelengths for the same normalized distances.

Besides the droplet volume and tilt angle, the film thickness and molecule weight of the polymer should also affect the formation and characteristics of the formed patterns. A larger film thickness tends to lead to a higher viscosity at the toluene/PMMA interface and larger resistance force against the contact line motion. A larger molecule weight could bring the similar effect. As a result of the change of the contact line motion, patterns of different dimensional characteristics can be formed. In addition, a thicker film can provide more materials to form the polymer ridges. Systematic works on the film thickness and molecule weight effects will be done in the future.

Figure 6.5 shows typical “cross” patterns consisting of four single fingers, which were

constructed via four carbon rods. The “cross” patterns, as shown in Fig. 5a, were formed, using four carbon rods of the same dimensions at a tilt angle of 2.86°.The carbon rods were perpendicular to adjacent rods. The “cross” patterns have four fold symmetry. Figure 5b shows the “cross” patterns formed by using four carbon rods with different tilt angles. The tilt angle was 5.71° for finger 1 (as indicated in Fig. 6.5b, 5.71° for finger 2, 2.86° for finger 3 and 2.29° for finger 4. As discussed previously, the geometrical characteristics of individual finger-like patterns are dependent on the tilt angle between the rod and the PMMA film. The use of different tilt angles led to the formation of the “cross” patterns with different finger lengths and widths. The surface patterns consisting of two fingers and three fingers, which were constructed via templates with two rods and three rods, respectively, are shown in Fig. S4 of supporting information. All of these demonstrated the potential to construct well-ordered surface structures of large area on the surface of polymer films simply through the confinement effect on the evaporation of volatile liquid and the control of geometric configuration of templates.

This system may also be applied to other polymers. Figure 6.6 shows the typical surface patterns formed on pre-cast polystyrene (PS) film via evaporating a toluene droplet with a tilt carbon rod. The film thickness is around 90 nm, and the tilt angle is 2.86°. Patterns different from those formed on PMMA film can be found. Along the symmetric axis (Fig.6.6a), multi-arcs were formed, which are not as smooth as the PMMA arcs. The arcs are partial undulated line and partial disconnected beads. Beads can also be found in some regions between two polymer ridges. In transition zone of the arc-segment and the straight line-segment (Fig.6.6b), only separated beads can be observed. Some of the beads seem to align into arcs, while others align randomly. In comparison, the PMMA patterns are always

continuous curves. The beads should the result of the dewetting of the PS film from the glass surface induced by the toluene. Owing to the unfavorable interaction of PS with glass,[188] PS is more likely to dewet into separated beads rather than keep as a film network or continuous curves, when treated with a solvent.

6.3 Conclusion

In summary, we fabricated well-ordered finger-like patterns on the surface of pre-cast PMMA films by forming a toluene-liquid bridge and confining the evaporation of the toluene bridge. The finger-like patterns consisted multiple arc-segments and parallel line-segments. The wavelength of the multiple arc-segments along the symmetric axis first decreases, reaches minimum, and then increases with increasing the distance to the fingertip. The dimensions of the finger-like patterns and the wavelength gradient of the multiple arc-segments are dependent on the droplet volume and the tilt angle. We also constructed the "cross" patterns of four finger-like patterns, using "four-rods-on-film" templates. Using similar mechanism, more complex patterns can also be constructed just by setting up templates of various geometrical configurations. The technique developed in this study provides the rationale to construct surface structures over a large area via the control of volatile liquid for the applications in flexible electronics, microfluidics, and biosensory devices.

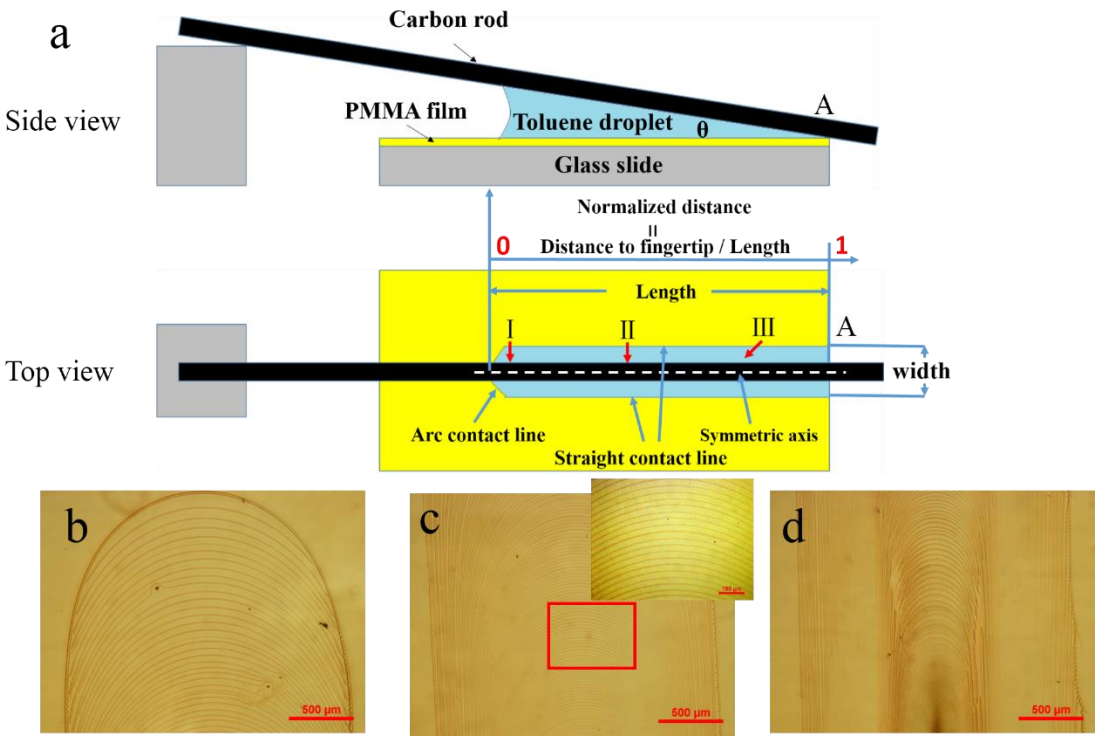

Figure 6.1(a) Schematic of the experimental set-up for constructing finger-like surface patterns, and (b-d) the surface patterns formed in the regions of Ⅰ, Ⅱ and Ⅲ indicated in (a). The inset in (c) is an enlarged view of the patterns enclosed in the red box (film thickness: ca. 90 nm; tilt angle: 2.86°; droplet volume: 5μL)

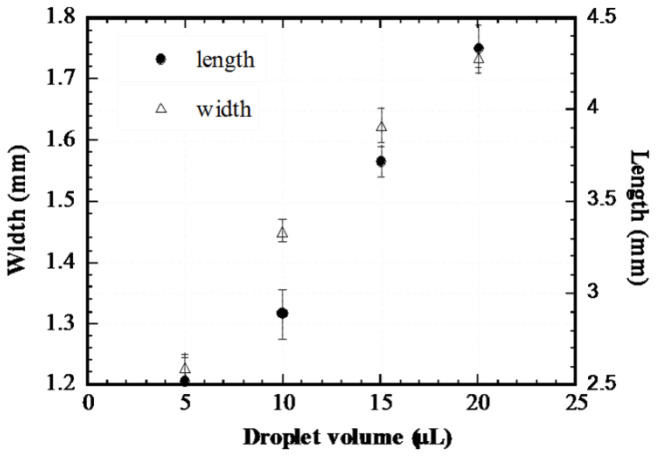

(a)

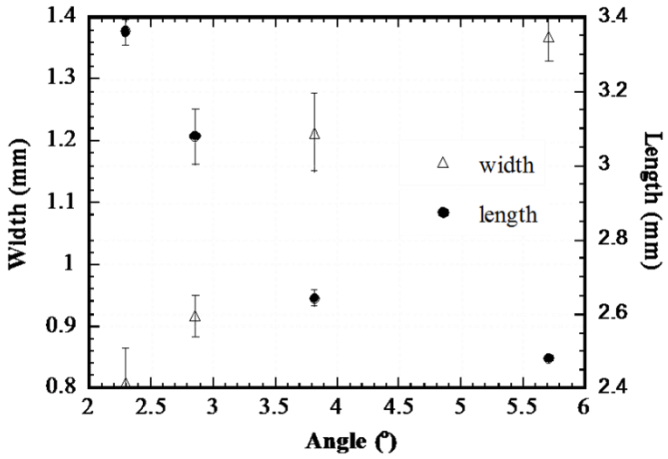

(b)

Figure 6.2 (a) Variation of the dimensions of the outmost finger-like pattern with the droplet volume (tilt angle: 2.86°, film thickness: ca. 90nm); (b) Variation of the dimensions of the outmost finger-like pattern with tilt angle (droplet volume: 5μL, film thickness: ca. 90nm).

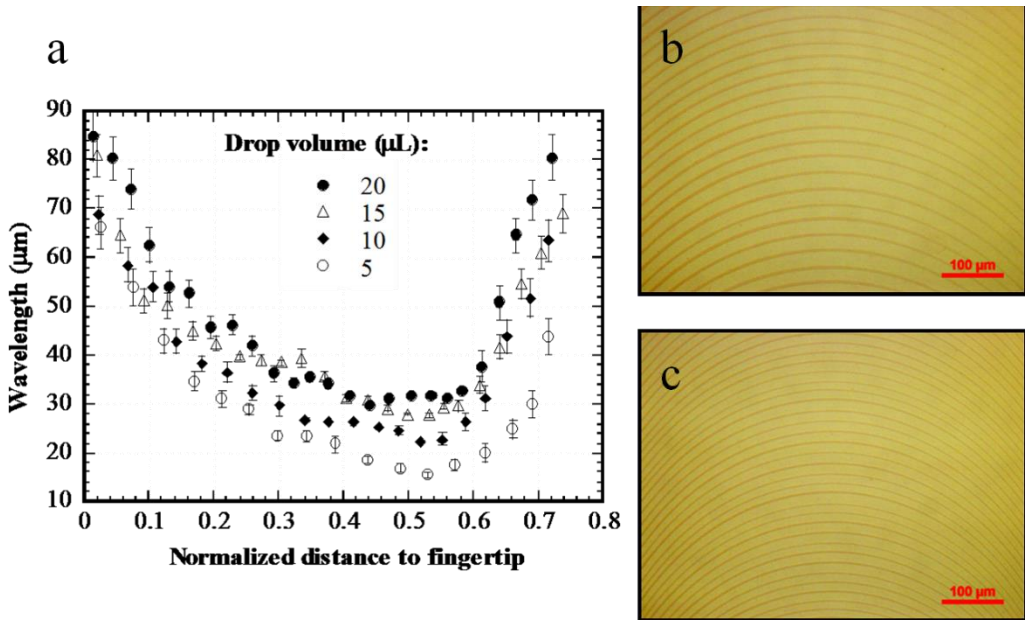

Figure 6.3(a) Variation of the wavelength with the normalized distance to the finger tip for different droplet volumes(tilt angle: 2.86°,film thickness: ca. 90nm);(b and c) Optical images of the typical multiple arc-ridges formed along the symmetric axis for different droplet volumes of 10μL (b) and 5μL (c)(tilt angle: 2.86°, normalized distance:0.5, film thickness: ca. 90nm)

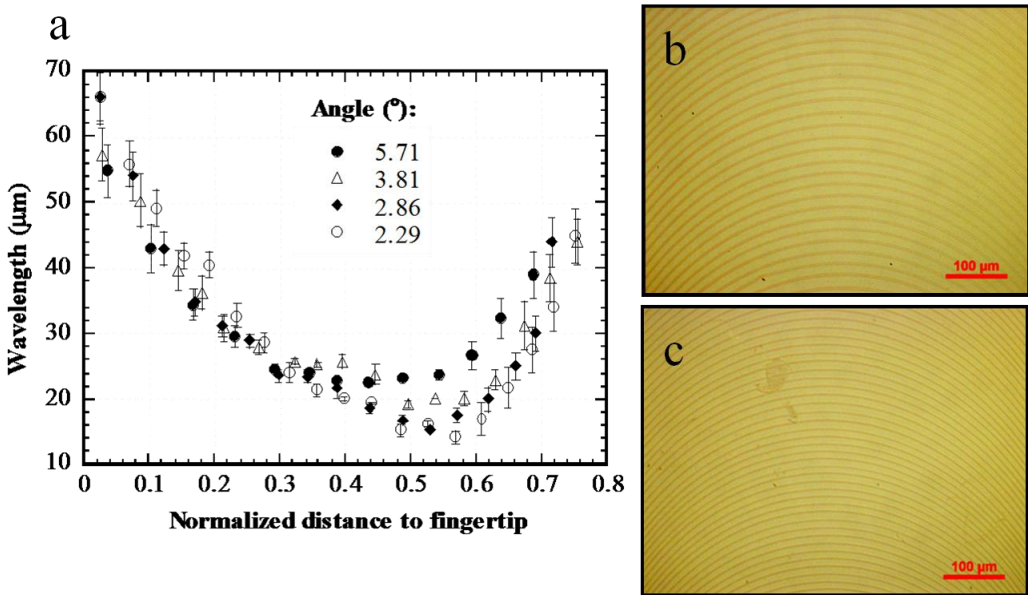

Figure 6.4 (a) Variation of the wavelength with normalized distance for four different tilt angles(droplet volume: 5μL, film thickness: ca. 90 nm); (b) and (c) optical images of the multiple arc-ridges formed along the symmetric axis for two tilt angles of 5.71° (b) and 2.29° (c) (droplet volume: 5μL,normalized distance:0.5)

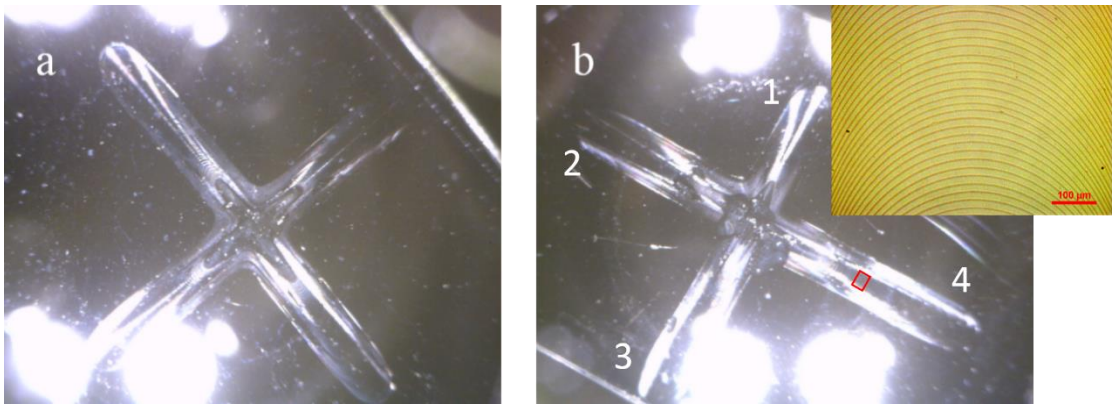

Figure 6.5 Optical images of the "cross" patterns: (a) the "cross" patterns of the same length; (b) the "cross" patterns of different lengths. The inset is an enlarged view of the patterns enclosed in the red box in (b).

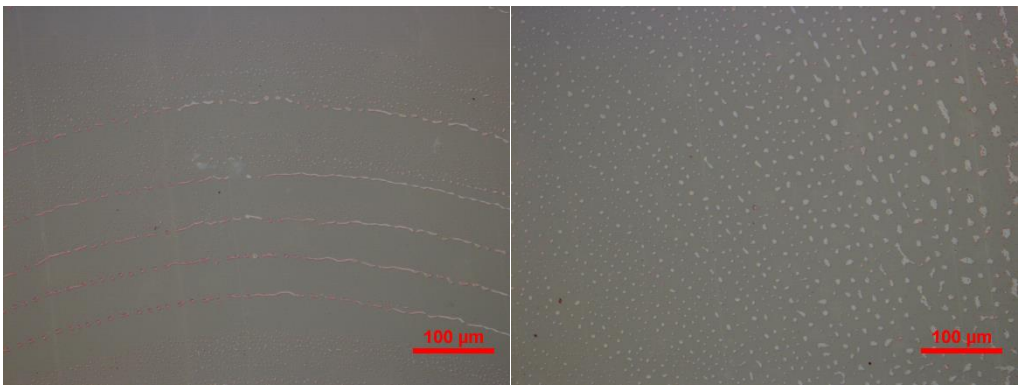

Figure 6.6 Optical images of the typical surface patterns formed on polystyrene (PS) film (tilt angle: 2.86°, film thickness: ca. 90nm). (a) along the symmetric, normalized distance: 0.25; (b) the transition zone of the arc-segment and the straight line-segment, normalized distance: 0.25.

Chapter 7. Cooling-induced formation of honeycomb patterns on pre-cast PMMA films at low temperatures

7.1 Introduction

Evaporating-induced surface patterning is an effective and efficient method to construct well-ordered surface structures. By evaporating a droplet of a polymer solution or a particle suspension on a non-dissolvable substrate [23] or a pure solvent droplet on a dissolvable polymer film [189], self-assembled patterns are formed through the "stick-slip" motion of the contact line, which is associated with the "coffee ring" effect [22]. Various patterns, such as concentric rings [58], parallel straight stripes [190, 191], gradient arcs, spokes [151], etc. have been constructed, using different templates. One can alter the geometrical characteristics of the surface patterns by controlling the solution concentration, template, film thickness, solvent, molecular weight, etc.

In addition to the patterns mentioned above, honeycomb structures, which has various application potentials [192], can also be fabricated via the solution evaporation [90]. When a droplet of a polymer solution, in which the solvent is immiscible with water, is placed on a substrate and evaporates at relatively high humidity, the evaporation of the droplet can introduce a temperature difference between the droplet surface and ambient environment, leading to the condensation of small water droplets onto the surface of the solution droplet.

The condensed water droplets can arrange into a hexagonal network which serves as a template for the formation of honeycomb patterns [193]. There are many factors, including ambient humidity [94], solvent [90], evaporation rate [194], solution concentration [94, 95], molecular weight [94, 195], surfactant [96], etc., which control the formation and geometric configurations of the "water-assisted" honeycomb patterns. Many materials, including hydrophobic polymer, amphiphilic copolymer [82], organic and saccharine-containing polymers [196], inorganic/organic hybrid [92], small organic molecules [93], etc., have been used to form honeycomb patterns via evaporation at relatively high temperatures. However, there is no report of the formation of honeycomb patterns at low temperatures.

Following the technique to form gradient concentric rings via the evaporation of a toluene droplet at room temperature [197], we develop a "ring-on-film" system, in which a pure toluene droplet is placed on the surface of a pre-cast PMMA film coated on a glass slide and a copper ring is used to confine the toluene droplet. Instead of using the air (moisture) flow for the condensation of water, a cooling stage is used to limit the evaporation of the toluene droplet at temperatures much lower than ambient temperature, which allows the condensation of water on the surface of the toluene droplet and leads to the formation of honeycomb-like patterns. The effects of the film thickness, the size of the copper ring and temperature are examined. In addition, the surface patterns formed on PS films, using the same template structure, are reported. It is worth pointing out that the system consists of a pure solvent and a pre-cast dissolvable film in contrast to the use of polymer solutions on non-dissolvable substrate systems, as reported in literature.

7.2 Experimental detail

Preparation of polymer films

The PMMA films were prepared, using a spin-coating process at room temperature. The solution for spin-coating was PMMA (Mw=35000) (Fisher Scientific, Pittsburgh, PA) in toluene (Fisher Scientific, Pittsburgh, PA). The spin-coating was performed on a spin coater (WS-400B-6NPP/LITE, Laurell Technologies Corp., North Wales, PA) at 2000 rpm. PMMA thin films of different thicknesses were obtained, using different solution concentrations (~90 nm from 1 wt% solution, ~140 nm from 2 wt% solution, and ~290 nm from 5 wt% solution, as measured by atomic force microscopy).

Formation of hexagon network on pre-cast PMMA films

The surface patterns were constructed via the evaporation of a toluene droplet on a pre-cast PMMA film, using a copper ring to confine the droplet. The evaporation temperature was controlled by a cooling stage. Figure 1a shows the experimental setup. A toluene droplet (~6 μL) was placed on the surface of a pre-cast PMMA film coated on a glass slide, and a copper ring with a wire diameter of 79 μm (30 AWG) was used to confine the droplet. The glass slide was then moved onto the cooling stage immediately. Note that the cooling stage had already reached the pre-set temperature before the glass slide was placed on it. The evaporation of the toluene droplet took place within an ambient environment (temperature: 24.8 ºC; humidity: 35%). The temperature of the surface temperature of the PMMA films was controlled in the range of -3.5 to 8 ºC, and the real-time temperature of the surface of the pre-cast PMMA films during the evaporation was monitored, using a thermocouple. The surface morphology of the surface patterns formed in different areas (as noted in Fig. 1a) after complete evaporation was examined under an optical microscope, and the height of the patterns was characterized by an atomic force microscopy (AFM). Copper rings of different diameters (1.45, 2.90, and 3.75 mm) were used to study the size

effect of the copper ring on the patterns.

7.3 Results

Figure 7.1b-d show the surface patterns formed on a pre-cast PMMA film of ~140 nm in thickness via the evaporation of a toluene droplet. The surface temperature of the PMMA film at equilibrium was 8 ºC. In the circular area of about 0.4 mm in radius around the center of the copper ring (noted as zone 1 in Fig. 7.1a), irregular holes were formed, of which the hole sizes are not uniform. A few large holes are observed, but most of the holes are small. In zone 2, the surface pattern exhibits a hexagon network with some local defects, and there is a size distribution of the hexagons. In zone 3, i.e. the area outside the copper ring, the surface patterns become more irregular. Both irregular holes of relatively large sizes and the local hexagon network can be found in some small areas. The following study mainly focuses on the regular patterns formed inside the copper ring.

Using a thermocouple, the temporal evolution of the temperatures of the cooling stage and the structure consisting of a pre-cast PMMA film and a glass slide was recorded, respectively. Figure 7.2 shows the variation of the measured temperatures of the cooling stage and the surface temperature of a pre-cast PMMA film of ~140 nm thickness with time for the cooling stage at a pre-set temperature of 5 ºC. Note that the cooling stage had already reached thermal equilibrium state at 5 ºC and the probe of the thermocouple was at 25 ºC before the measurement. It took about 30 s for the probe/cooling stage to reach local thermal equilibrium at ~6.8 ºC, while it took about 50 s for the probe/PMMA/glass

structure to reach local thermal equilibrium at ~8 ºC. There exists a temperature difference between the cooling stage and the surface of the PMMA film, which was due to the difference between the pre-set temperature and the ambient temperature and the resistance of the glass slide and the PMMA film to heat flow. This result suggests that toluene droplets were at a non-thermal equilibrium state during the evaporation in addition to the evaporation-induced temperature difference between the contact front and the evaporation surface.

Figures 7.3a-c show the patterns formed in zone 1 for PMMA films of three thicknesses. The surface temperature of the films at equilibrium was ~8 ºC. Holes of multiple sizes were formed on the PMMA films of ~90, ~140 and ~290 nm thicknesses are non-uniform. Several holes, as circled by red circles, are relatively large, and most holes are relatively small. Figure 7.3d shows the size distributions of the holes formed on the PMMA films of three thicknesses. Broad distribution of the hole sizes is observed for all the three films. Generally, the holes in the thicker films have smaller sizes than the holes in the thinner films. Most holes have the sizes in the range of 2-3.5 μm for ~90 nm films, 1-2.5 μm for ~140 nm films, and 0.5-2 μm for ~290 nm films, respectively. There are only small portion of holes with larger sizes for all the films.

The surface patterns in zone 2 on all the films appear more likely as a hexagon network, as shown in Figs. 7.4a-c, for water condensed on the films at an equilibrium surface temperature of ~8 ºC. The surface pattern formed on the thinnest films (~90 nm) has a nearly perfect hexagon network, while some local defects can be observed on thicker films. The average size of a single unit (hexagon) decreases with the increase of the film thickness, which is ~4.37±0.55 μm for ~90 nm films, ~2.96±0.91μm for ~140 nm films, and

~1.83±0.57 μm for ~290 nm films. Comparing with the surface patterns formed in zone 1 for the same film thickness, one can note that the sizes of the hexagon holes in zone 2 are more uniform. Figure 4d shows the size distribution of the hexagons in zone 2. About 86% hexagonal holes have size in the range of 2.5-5.5 μm for ~90 nm films, about 84% hexagonal holes have sizes in the range of 2-4 μm for ~140 nm films, and about ~90% hexagonal holes have sizes in the range of 1-3 μm for ~290 nm films. There is no significant change in the sizes of the hexagon holes formed in zone 2.

Fast Fourier Transform (FFT) was used to analyze the ordering of the holes. The FFT diffraction patterns, as shown in the inset in Figs. 7.3a-c and Figs. 7.4a-c, reveal a square arrangement of both the nearly circular holes in zone 1 and hexagonal holes in zone 2. The hexagonal packing of the holes is known as a usual packing mode of holes, which is free-energy favored [198]. The mechanism for the square arrangement is unclear, which might be attributed to the low substrate temperature. The low surface temperature of the toluene droplet can lead to a fast condensation of water droplets and reduce the mobility of the water droplets, resulting in a non-equilibrium packing mode. Other factors, i.e. micro-flow inside the toluene droplet and the evaporation rate of the toluene might also play important roles in the packing of the water droplets and influence the arrangement of the holes and the surface patterns.

Figures 7.5a-c show the surface patterns formed on a ~290 nm PMMA film with copper rings with different sizes. The surface temperature of the film is 8 ºC. Holes of multiple sizes are observed for all the three copper ring sizes. As shown in Fig. 7.5d, the holes formed with all the three copper rings have broad size distributions, while the hole size is relatively more uniform for the patterns formed with a smaller copper ring. The hole size

also has a decreasing tendency with the decrease of the size of the copper ring. The hole size is in the range of 2.5-4.5 μm for the ~3.75 mm copper ring, 1-3.5 μm for the 2.90 mm copper ring, and 0.5-2 μm for the 1.45 mm copper ring, respectively.

The hexagonal network is formed in zone 2 for the templates with the three copper rings, as shown in Figs. 7.6a-c. Generally, the size of the hexagons decreases with the decrease of the size of the copper ring. The average size of hexagonal units is ~4.72±1.20 μm for the ~3.75 mm copper ring, ~3.56±0.71 μm for the 2.90 mm copper ring, and ~1.83±0.57 μm for the 1.45 mm copper ring, respectively. Figure 6d shows the size distribution of the hexagon units in zone 2. The patterns formed with a smaller copper ring have narrower size distribution than those formed with a larger copper ring. About 92% hexagonal holes have sizes in the range of 2.5-6.5 μm for the ~3.75 mm copper ring, 90% of the hexagonal holes have sizes in the range of 2-5 μm for the ~2.9 mm copper ring, and 90% hexagonal holes have sizes in the range of 1-3 μm for the ~1.45 mm copper ring, respectively.

Figure 7.7 shows the surface patterns formed in zone 2 on the PMMA films of ~290 nm film thickness at four equilibrium temperatures. The copper ring size is 1.45 mm. At the temperature of -3.5 ºC, the surface patterns were random and disorder, while at the temperature of ~8 ºC, the surface patterns became well-ordered. Increasing the temperature introduced a transition of the surface patterns from disordered structures to well-ordered hexagon networks. Note that well-ordered concentric rings instead of hexagon networks will be formed at room temperature [197]. The morphology of the holes changed from irregular shape to uniform and regular hexagon.

Figure 7.8 shows a typical AFM image of the hexagon network formed in zone 2 on a

~90 nm PMMA film. The surface temperature of the film at equilibrium state was ~8.0 ºC. The surface pattern appears as a hexagon network in accord with the optical image shown in Fig. 7.7d. By drawing a line across the AFM image, one can determine the heights of the polymer ridges, i.e. the heights of the walls of the hexagon hexagons. Figure 7.8b shows the topology of the polymer ridges, corresponding to the line scan in Fig. 7.8a. It is clear that there is no significant difference in the heights of the polymer ridges. Multiple scans were performed over the PMMA films of three different thicknesses. The measurement results are depicted in Fig. 7.8c. The height of the polymer ridges increases with increasing the thickness of the PMMA films.

The formation of surface patterns on a PS film was also examined, using the same experimental procedure. The thickness of the PS film was ~290 nm, and the diameter of the copper ring was 1.45 mm. The equilibrium surface temperature was ~8. 0 ºC. Figure 9 shows the typical surface patterns formed. Comparing Fig. 7.7 with Fig. 7.5, one can note that the surface patterns formed on the PS film is significantly different from those on the PMMA films. The patterns in both zone 1 and zone 2 are irregular and the thickness of the polymer ridges is non uniform. The average hole size in zone 2 is much smaller than that in zone 1. Generally, the evaporation kinetics of toluene is dependent on the interaction between toluene and substrate. Such behavior likely reveals that the interaction between PMMA and toluene is different from that between PS and toluene.

7.4 Discussion

Generally, a toluene droplet will spread and evaporate simultaneously after being placed on the surface of a PMMA film at ambient temperature. The copper ring will confine

the spreading of the toluene droplet and keep the moving front circular if there are no local defects to pin the motion of the contact line. Following the placement of the toluene droplet, the structure consisting of the droplet, PMMA film, and a glass substrate is moved to a cooling state with a temperature less than ambient temperature. This will cause the condensation of water on the surface of the toluene droplet and the surface of the PMMA film not covered by the toluene droplet. The condensation of water on the surface of the PMMA film will reduce the resistance to the motion of the contact line and accelerate the spreading of the toluene droplet. It also can introduce local disturbance, due to non-uniform condensation of water, to the motion of the contact line and cause the contact line to deviate from a circular-like contour to an irregular one. The water condensation can only limit the evaporation of the toluene confined by the copper ring through the formation of water micro-droplets. It is known that the density of water is larger than that of toluene and there is a deformable layer formed at the interface between the toluene and the PMMA film due to the penetration of toluene into the PMMA film [199]. The water droplets will cause deformation of the deformable layer, which leads to the formation of vertical channels, i.e. the PMMA ridges, after the evaporation of the toluene. Note that the vertical channels provide the space for the evaporation of the toluene. Since water is immiscible with toluene, the water droplets will continuously occupy the same positions until they are completely evaporated. This route eventually leads to the formation of holes on the surface of the PMMA film, as demonstrated above.

The hexagon patterns formed on the PMMA films can be explained by the "breath figure" mechanism [200]. Figure 7.10 shows a schematic illustration of the formation of a water droplet template. As shown in Fig. 7.2, the temperature of the PMMA film was less

than ambient temperature after placing the droplet/film/glass system on the surface of a cooling stage. It is expected that the temperature on the surface of a toluene droplet on the surface of a PMMA film over a cooling stage also is less than ambient temperature. Due to the temperature difference between ambient temperature and the temperature of the toluene droplet, water condensation on the surface of the toluene droplet occurs even for a relative humidity of 35% and the nucleation of water droplets takes place when the droplet sizes are larger than the critical size. The droplets gradually grow with time and arrange into hexagonal geometry locally under the action of capillary force and the interaction between droplets [94]. With continuous evaporation of toluene, these water droplets gradually penetrate into the compliant PMMA film, resulting in the formation of a porous PMMA film with a hexagonal surface pattern after both water and toluene completely evaporate.

The evolution of water droplets and the interaction between water droplets and the compliant substrate are a function of the experimental conditions, including the film thickness, temperature, and the film material, as demonstrated above. The use of a copper ring to confine the spreading and evaporation of the toluene droplet has made the evaporation process different from the evaporation of a droplet without any confinement, which can be in a mode of constant contact area, constant contact angle, or a mixed mode with only one contact line. With the confinement of the copper ring, the contact line outside the copper ring moves towards the copper ring after the end of spreading, and the surface of the toluene droplet inside the copper ring evolves gradually from convex to concave during evaporation. This allows the accumulation of water droplets on the surface of the toluene droplet and the motion of water droplets towards the center of the copper ring (i.e. the vertex of the surface of the toluene droplet). The motion of water droplets introduces

the collision and merge of water droplets to form larger water droplets in contrast to the formation of uniform water droplets on a smooth, flat surface. The large droplets formed through random merge of small droplets leads to the wide distribution of the porous structures in zone 1. Note that the motion of water droplets on the surface of the toluene droplet and the evaporation of toluene also induce micro-flow inside the toluene droplet, and the micro-flow plays a role in controlling the motion of water droplets. In contrast, the water droplets in zone 2 are at a relatively stationary state due to the nonslip condition imposed by the copper ring, which limits the collision and merge of water droplets and water droplets have relatively uniform size. The water droplets of relatively uniform size form a water-droplet-template, leading to the formation of well-ordered hexagonal network in zone 2.

Effect of film thickness

Figure 11 shows the variation of the size of the hexagonal unit with the thickness of the PMMA film. The size of the hexagonal unit decreases with the increase of the film thickness when other experimental conditions remain the same. Generally, the size of a water droplet is determined by the nucleation size and the growth rate. From the theory of thermodynamics, the critical radius for the formation of a water droplet is [201]

$$R_{cr} = \frac{2\Omega\gamma}{kT_s \ln(p_s / p_\infty)} \tag{7.1}$$

where R_{cr} is the critical droplet radius, γ is the surface tension, Ω is the volume per one water molecule, k is the Boltzmann constant, T_s is the surface temperature of the toluene droplet, p_s is the vapor pressure on the surface of the toluene droplet, p_∞ is the vapor pressure of environment. The growth rate of a droplet is dependent on the absorption and

diffusion of water molecules, which can be expressed as

$$\frac{dR}{dt} = A(T_\infty - T_s)^n \tag{7.2}$$

where R is the radius of the water droplet, t is time, T_∞ is the temperature of the environment, n(>0) is a power index, and A is a coefficient. Note that Beysens et al. [202] suggested n=1, and Xu et al. [94] suggested n=0.8. Generally, the PMMA concentration near the toluene surface is higher for a thicker film due to the fast diffusion of toluene into the PMMA film. The solvent (toluene) in a more concentrated solution has lower vapor pressure, resulting in slower evaporation and a higher temperature on the surface of the toluene surface over a thicker PMMA film than that of a thinner PMMA film. Note that the surface temperatures of PMMA films at local equilibrium state were 8.0±0.1, 8.0±0.2 and 8.2±0.2 for the PMMA films with thicknesses of ~90, ~140, and ~290 nm, respectively, which indirectly supports that the surface of the toluene droplet over a thicker PMMA film might have a slightly higher temperature. According to Eqs. 7.1 and 7.2, both the critical radius for the formation of water droplets and the growth rate of water droplets on the surface of the toluene droplet over a thicker PMMA film thus are smaller than those on a thinner PMMA film. As we observed, there is no significant difference in the total evaporation time of toluene droplets of the same size on PMMA films of different thicknesses. One can conclude from Eqs. 7.1 and 7.2, smaller water droplets will be formed on a thicker PMMA film, which leads to the formation of a hexagonal network with hexagonal unit of smaller size in accord with the experimental observation.

Effect of the copper ring size

As shown in Fig. 7.11b, the size of the hexagonal unit increases with the increase of the

copper ring size. The mechanism for this phenomenon is very complicated, and it might be closely related to the geometry of the toluene droplet limited by the template (copper ring). Without any templates, the toluene droplet can wet a PMMA film well and form a very thin liquid film. With the presence of a copper ring, the liquid film will curve up in the area near the copper ring due to the confinement effect [203]. A decreasing gradient of the thickness of the toluene liquid film from the copper wire to the copper ring center is introduced, leading to a concave surface of the toluene film inside the copper ring, as shown in schematic illustration in Fig. 7.10. The thickness of the toluene film inside a larger copper ring is expected to be smaller than that within a smaller copper ring of the same wire size, especially for the region near the center, due to a larger distance to the copper ring. As the toluene liquid film is placed between the warmer air and the cooler substrate, there is a temperature gradient within the toluene in the direction parallel to the surface normal. For a thinner toluene film, the temperature of the top surface T_s is lower than that of a thicker toluene film since the surface is closer to the cold substrate. Thus, the toluene film confined by a larger copper ring has a cooler surface. According to Eq. 7.1, the critical radius for the formation of a water droplet is larger for the case with a larger copper ring, which partially contributes to the larger sizes of the units formed with a larger copper ring. In addition, the size of the copper ring also affects the growth behavior of water droplets, the evaporation of the toluene droplet, the micro-flow inside the toluene droplet etc., which determine the geometrical characteristics of the surface patterns. Due to the limit of experimental conditions, we will address the effects of some other factors in the future work.

Effect of temperature

As shown in Fig. 7.7, the morphology of the surface patterns is significantly dependent on the surface temperature of the toluene droplet (or the temperature of the cooling stage). Lower temperatures caused the formation of irregular patters with wider distribution of hole sizes, and relatively high temperature led to the formation of hexagonal networks. Such behavior likely is associated with the temperature dependence of the water condensation. A lower temperature will lead to a higher condensation (nucleation) rate and a higher growth rate of water droplets. This trend will increase the random migration of water droplets on the surface of a toluene droplet and the frequency of collision between water droplets, which will result in the formation of water droplets of different sizes. The sinking of water droplets of different sizes into the deformable PMMA film leads to the formation of the honeycomb structure with a wider distribution of hole sizes at lower temperatures. A water-droplet-template of uniform size results in the formation of a hexagonal network on a PMMA film.

7.5 Conclusion

In summary, we constructed honeycomb structures on pre-cast PMMA films via the evaporation of a toluene droplet on a PMMA film at low temperatures. Using a copper ring, we confined the spreading and evaporation of the toluene droplet on the surface of the PMMA films. Honeycomb structures with various topologies, including hexagonal network, were formed in different regions due to the formation of water-droplet-templates during the evaporation, which were dependent on the evaporation kinetics, micro-flow, and the interaction between water droplets. Near the center of the copper ring, holes with a broad size distribution were formed due to the coalescence of the water droplets. In the

area away from the center inside the copper ring, regular hexagon networks were formed at the temperature of ~8 ºC. The average size of the hexagonal units increases with the decrease of the film thickness and with the decrease of the copper ring size, and the height of the polymer ridge increases with the increase of the film thickness. More regular patterns were obtained when the temperature of the cooling stage was relatively higher. A significantly different honeycomb structures was formed on a PS film from the PMMA films, which is likely due to that the interaction between PMMA and toluene is different from that between PS and toluene.

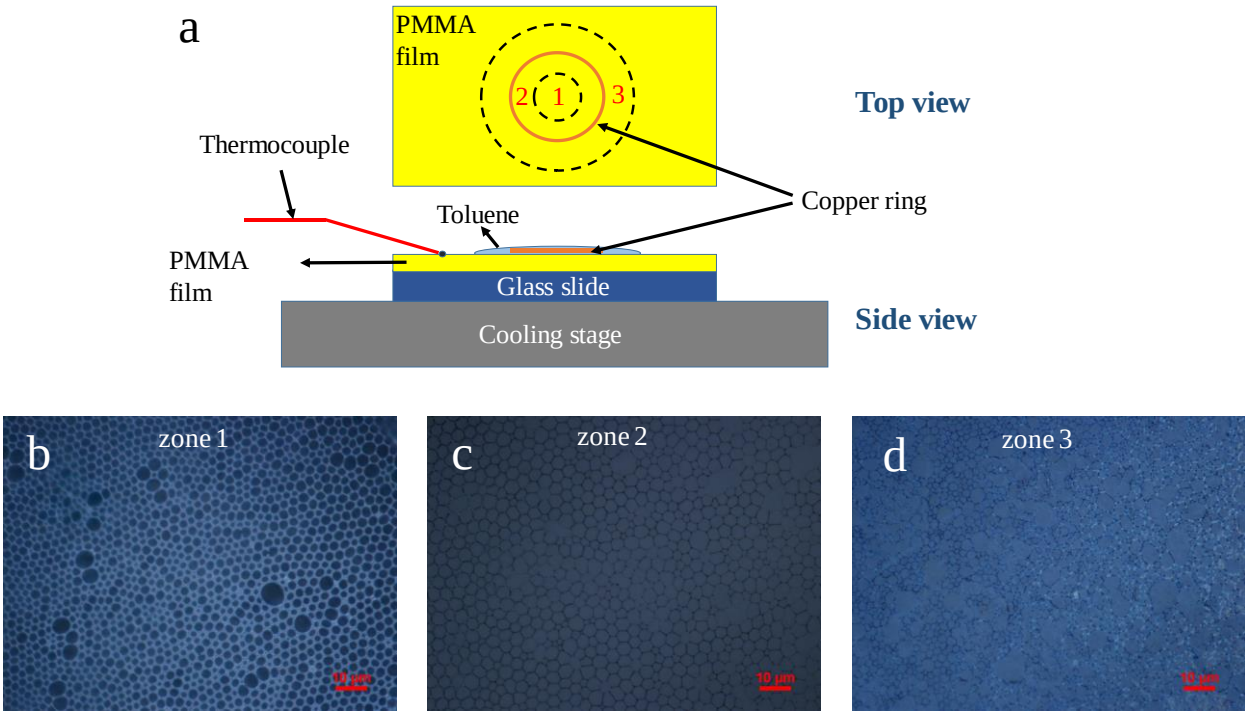

Figure 7.1 (a) Schematic of the experimental setup; (b-d) surface patterns formed in the zones of 1-3 as labeled in Fig. 1a, respectively (film thickness: ~140 nm, the diameter of the copper ring is 1.45 mm, surface temperature of the film at equilibrium: 8 ºC)

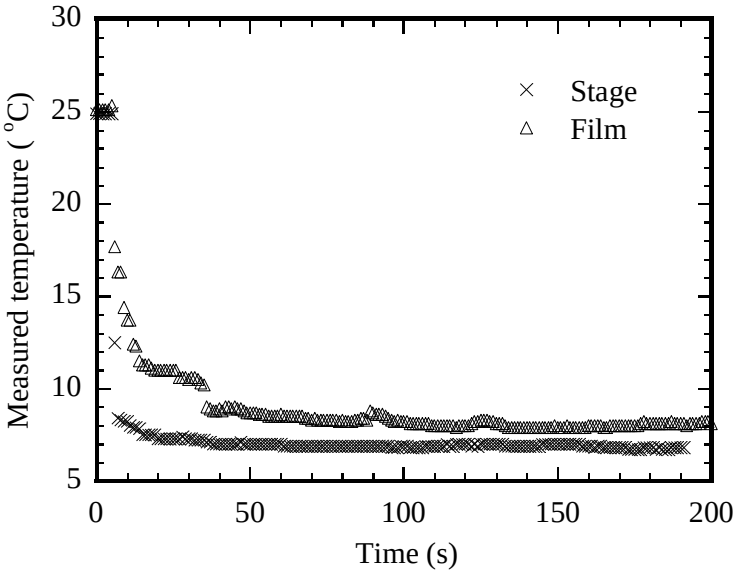

Figure 7.2 Temporal evolution of the temperature of the cooling stage and the surface temperature of a pre-cast PMMA film of ~140 nm thickness

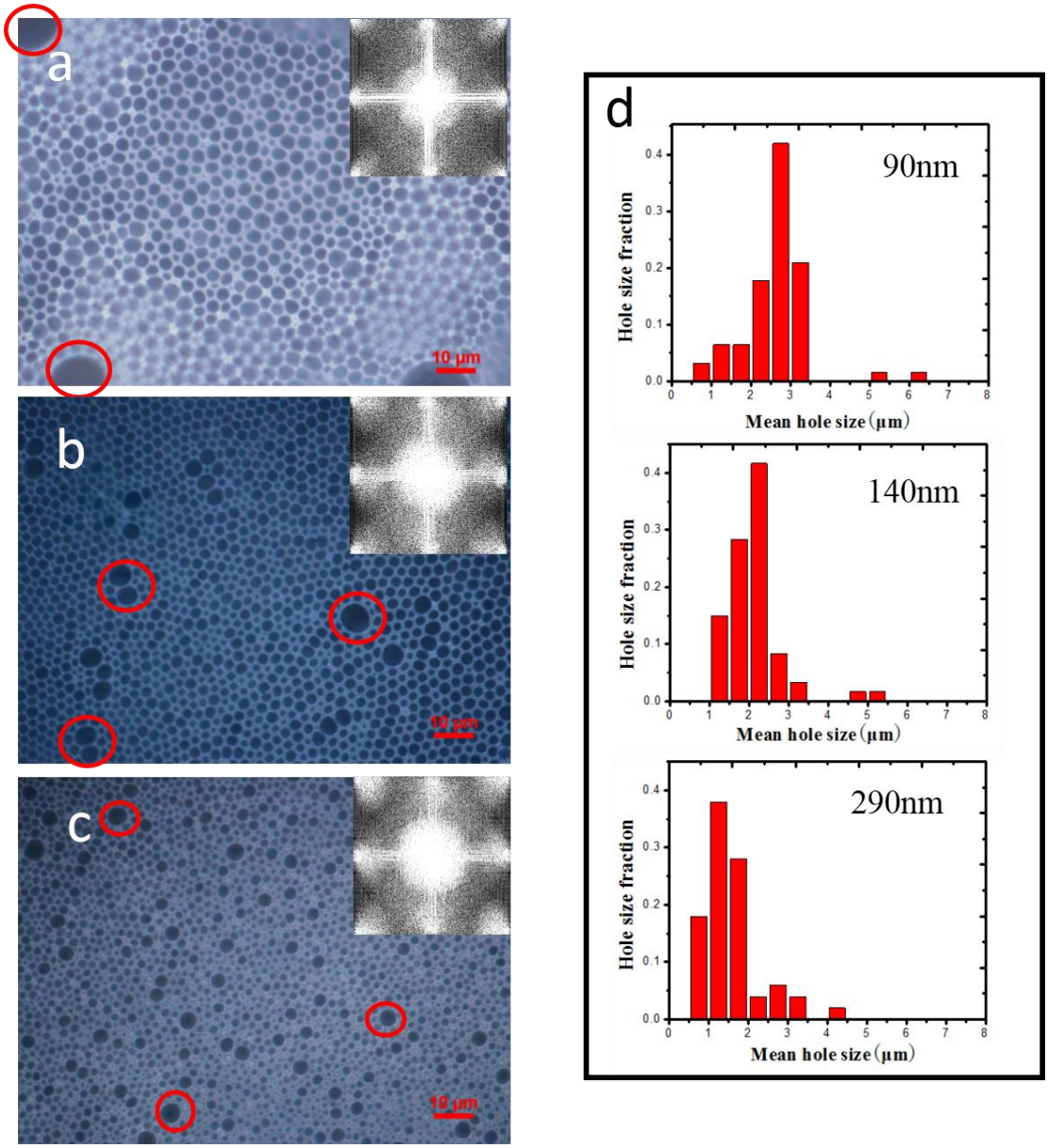

Figure 7.3 Surface patterns formed in zone 1 on different PMMA films; (a) ~90 nm in thickness, (b) ~140 nm in thickness and (c) ~290 nm in thickness; (d) size distribution of the holes formed on the PMMA films (surface temperature of the PMMA at equilibrium: ~8 ºC, the diameter of the copper ring is 1.45 mm). Inserted images are the Fast Fourier Transform (FFT) patterns of the corresponding surface patterns.

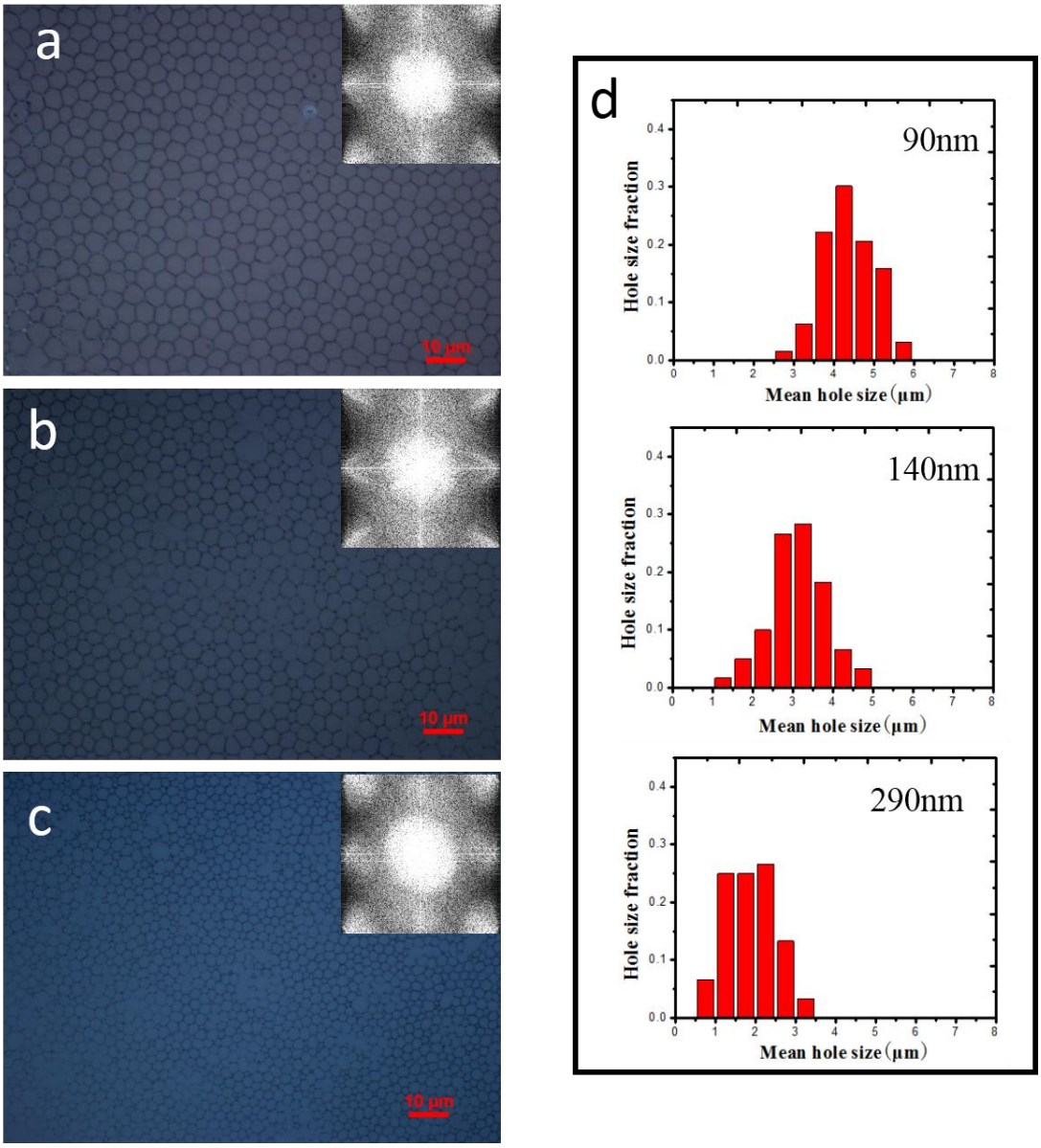

Figure 7.4 Patterns formed in zone 2 on different PMMA films; (a) ~90 nm in thickness, (b) ~140 nm in thickness and (c) ~290 nm in thickness; (d) size distribution of the holes formed on the PMMA films (surface temperature of the films at equilibrium: ~8 ºC, the diameter of the copper ring is 1.45mm). Inserted images are the FFT patterns of the corresponding surface patterns.

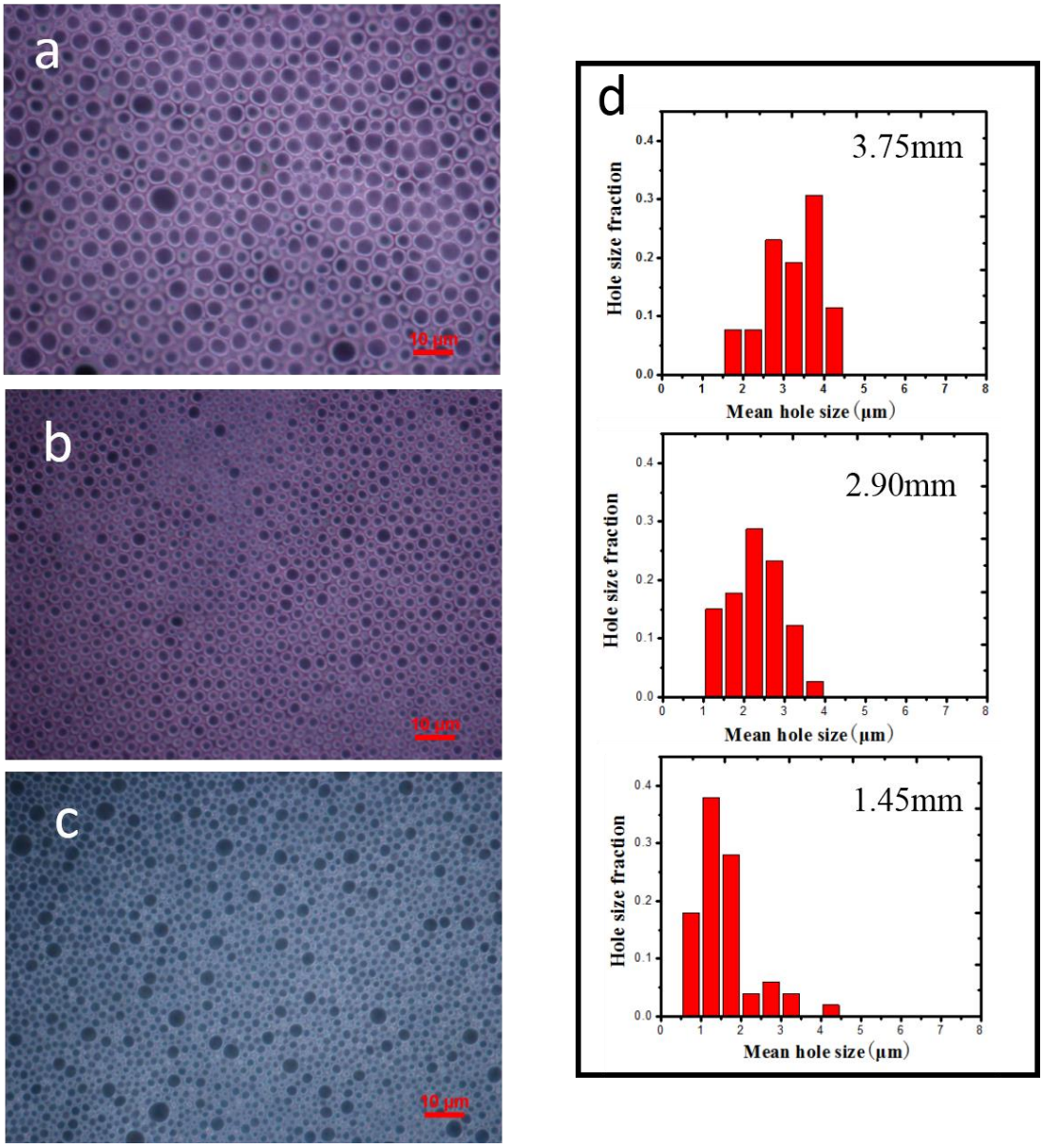

Figure 7.5 Surface patterns formed in zone 1 on PMMA films with copper rings of different sizes (a) ~3.75 mm in diameter, (b) ~2.90 mm in diameter, and (c) ~1.45 mm in diameter; (d) size distribution of the holes formed on the PMMA films (film thickness: 290 nm, surface temperature of the PMMA at equilibrium: ~8 ºC)

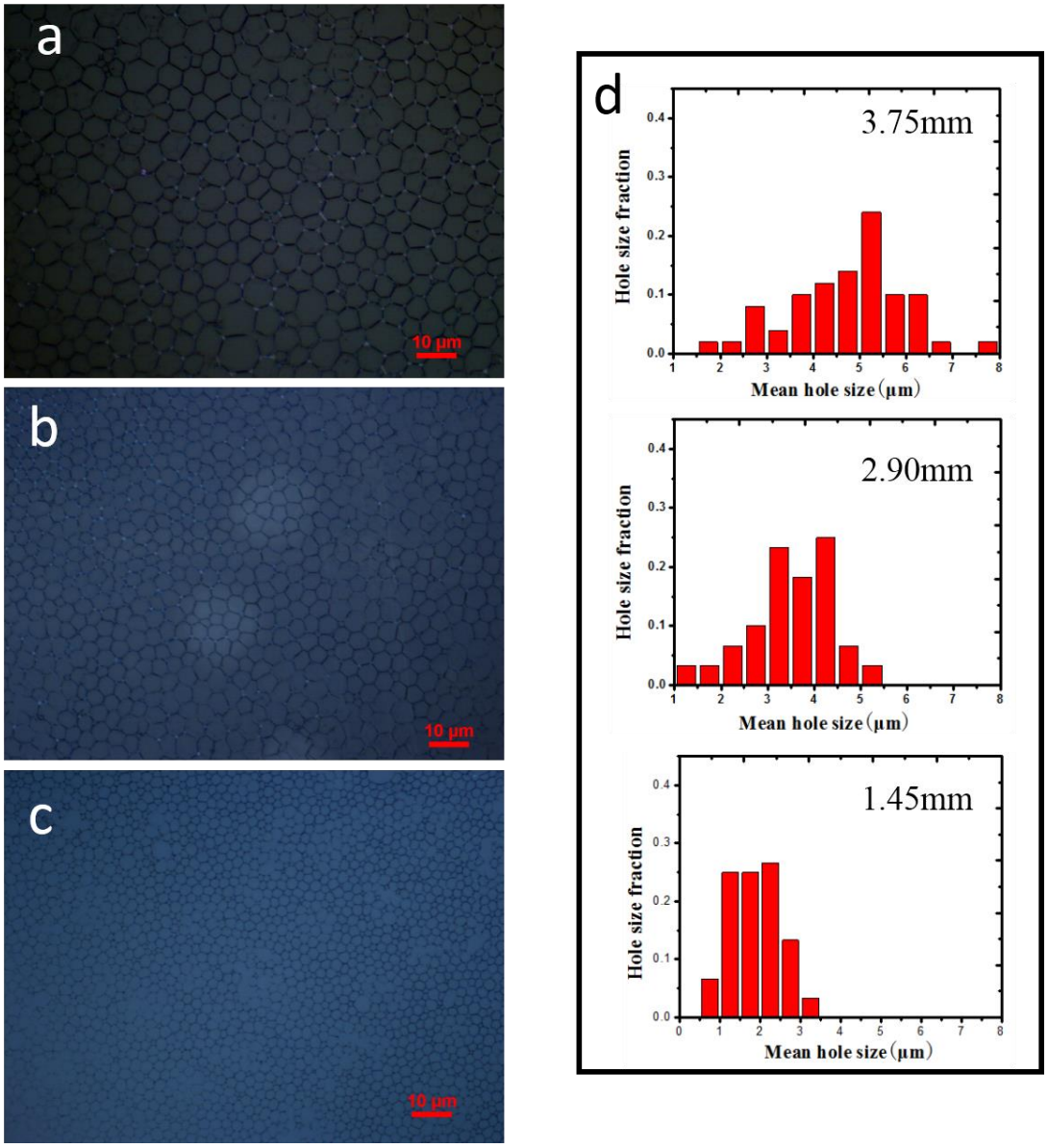

Figure 7.6 Surface patterns formed in zone 1 on PMMA films with copper rings of different sizes (a) ~3.75 mm in diameter, (b) ~2.90 mm in diameter, and (c) ~1.45 mm in diameter; (d) size distribution of the holes formed on the PMMA films (film thickness: 290 nm, surface temperature of the films at equilibrium: ~8 ºC)

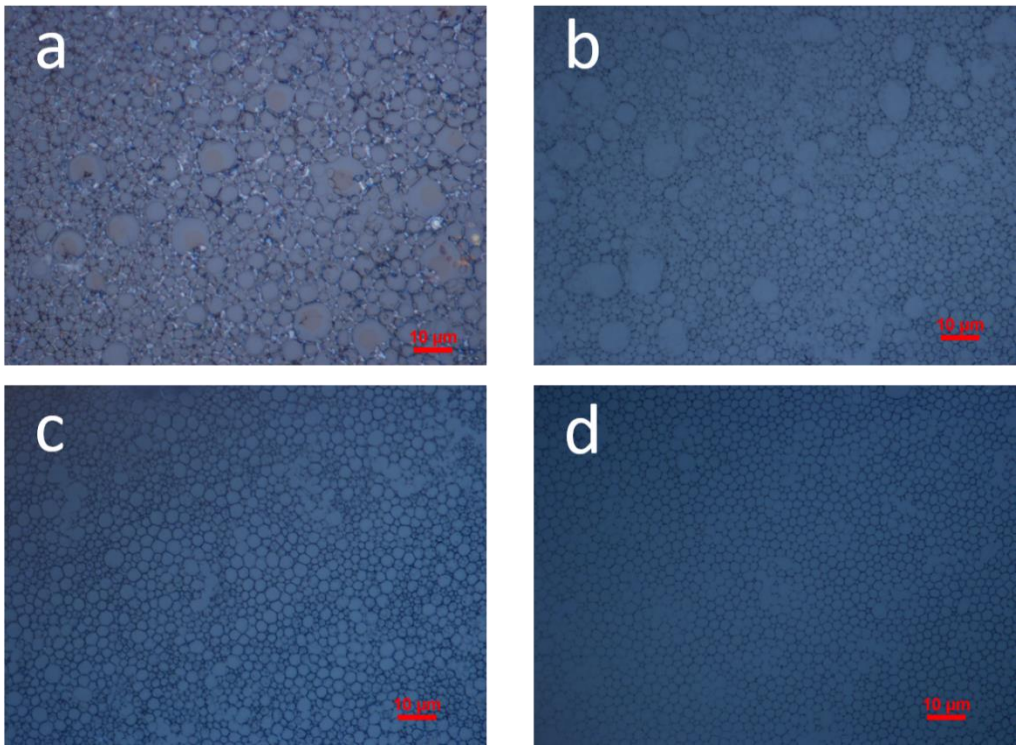

Figure 7.7 Surface patterns formed in zone 2 on the PMMA films of ~290 nm film thickness at four equilibrium temperatures; (a) -3.5 ºC, (b) ~1.8 ºC, (c) ~6.0 ºC and (d) ~8.0 ºC (copper ring size: 1.45 mm).

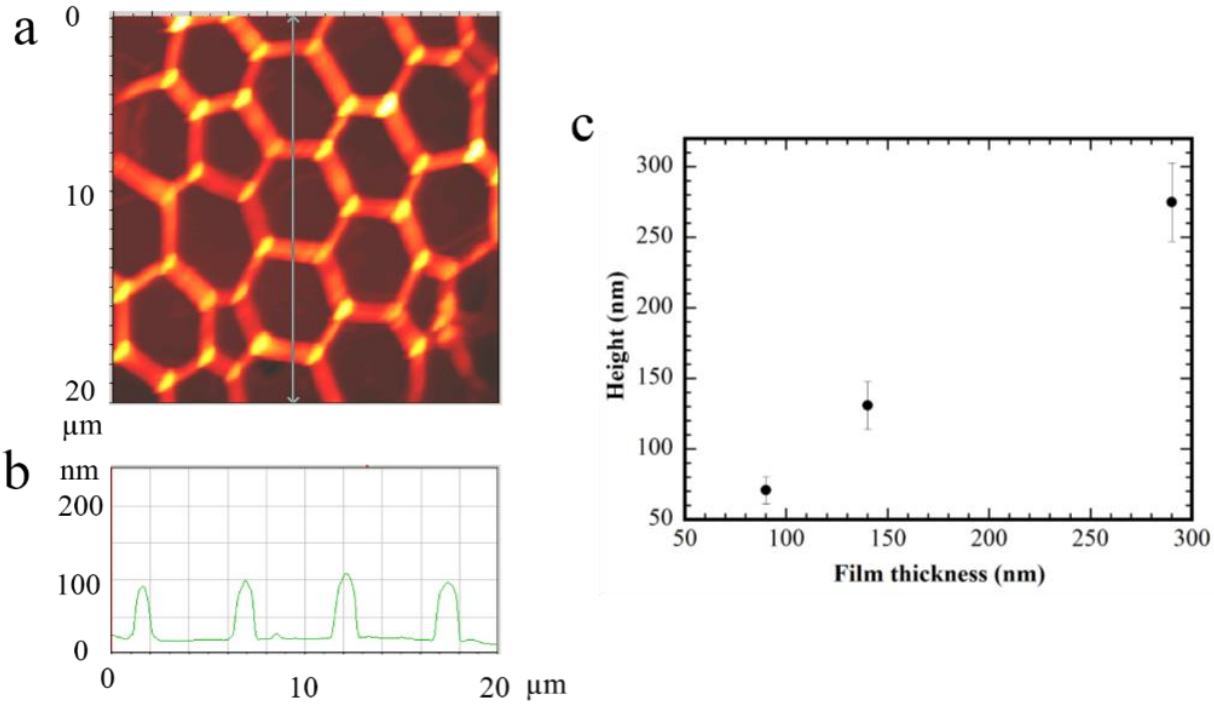

Figure 7.8 (a) A typical AFM image of the hexagon network formed in zone 2 on a PMMA film of ~90 nm thickness, (b) a line scan of the surface profile corresponding to the line in (a), and (c) variation of the wall height of the hexagon network with the film thickness (surface temperature of the film at equilibrium state: ~8.0 ºC)

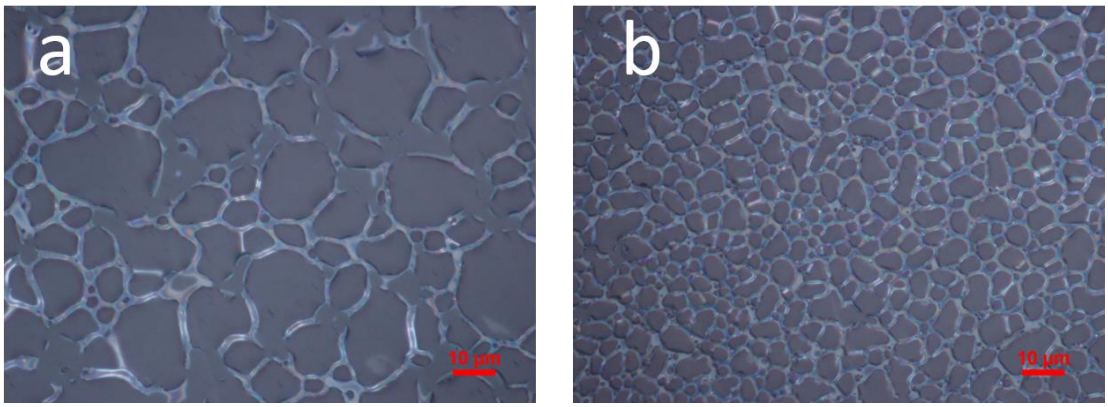

Figure 7.9 Surface patterns formed on a PS film via the evaporation of a toluene droplet: (a) in zone 1, and (b) in zone 2 (film thickness: ~290 nm, equilibrium temperature of the film surface: ~8.0 ºC, diameter of the copper ring: 1.45 mm)

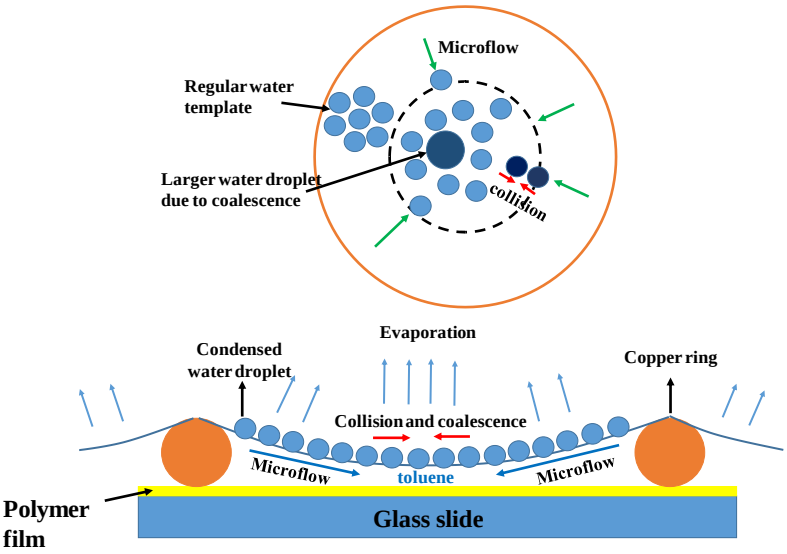

Figure 7.10 Schematic illustration of the formation of the breath figure template during the evaporation of a toluene droplet on a cooled PMMA film

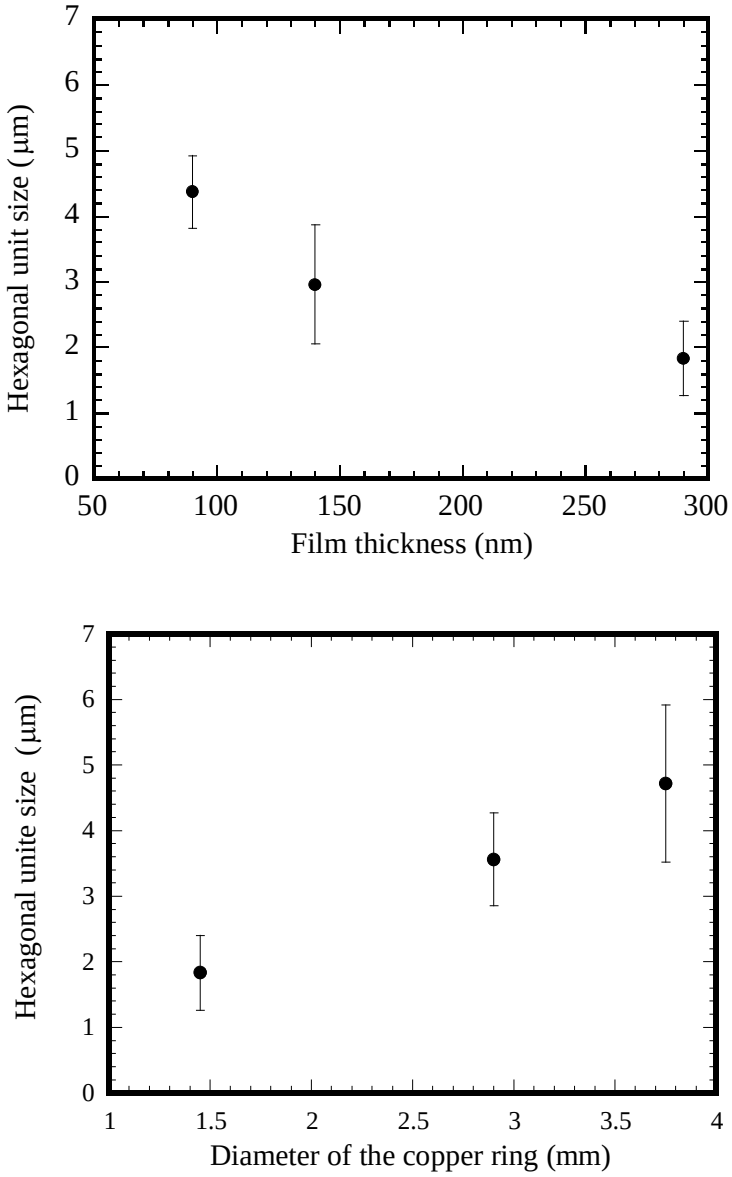

Figure 7.11 (a) Size variation of the hexagonal unit with the PMMA film thickness, and (b) size variation of the hexagonal unit with the copper ring diameter (film thickness: 290 nm, surface temperature of the film at equilibrium state: ~8.0 ºC).

Chapter 8. Dynamics of the evaporative dewetting of a volatile liquid film confined within a circular ring

8.1 Introduction

Dewetting, referring to the retraction of a liquid film from the surface of a substrate [99], is a common phenomenon that occurs in our daily life. The dewetting phenomenon is mainly controlled by two factors: thermodynamically instability (normal convective dewetting) and evaporation (evaporative dewetting). [108] A polymer film on a "hostile" substrate dewets from the substrate in order to minimize the surface energy at a temperature above the glass transition temperature of the polymer. [112, 113] Various patterns can be formed after dewetting, including dots, [204] worm-like ridge, [113] circular holes, [112, 114] etc. Most studies on evaporative dewetting have focused on the films of polymer solution or particle suspension and revealed that the evaporative dewetting can lead to the deposition or accumulation of non-volatile solute (polymer [115] or nanoparticles [116-118]) on the surface of substrate and the formation of various labyrinthine structures and polygonal networks. [108, 119-121] The dewetting patterns are generally associated with the formation and motion of three-phase contact lines and the instabilities in the vicinity of the contact lines during the dewetting.

In general, the motion of the contact line of a droplet is dependent on the wettability of the droplet on substrate. For a wettable system,[205] the contact line tends to be pinned, and the liquid film evaporates at the mode of constant contact radius (CCR). [123, 124] If a droplet cannot wet a substrate, a smooth contact line motion with a constant contact angle [126-128] is expected. The evaporation of solvent can lead to complicated "stick-slip" [23, 56, 130, 131] or "advancing-receding"[50, 51] motion of the contact line for a droplet of a polymer solution or a nanoparticle suspension and the formation of surface patterns [11, 22, 24, 66, 69, 189, 199].

Using various templates, one can control the dewetting behavior and the surface patterns formed during evaporation. Chen et al. [206] constructed a macroscopic gradient-concentric ring-like pattern via the evaporation of polystyrene solutions in a petri dish and studied the "stick-slip" motion of the contact line. Sun and Yang [197] developed a "ring-on-film" template to fabricate gradient concentric rings both inside and outside a copper ring via evaporating a pure toluene droplet on a pre-cast PMMA film. They observed a featureless zone formed at the center of the copper ring due to the smooth dewetting of the liquid film. They did not study the motion of the contact line which plays an important role in controlling the formation of the featureless zone. There are various reports on the droplet behavior and the evaporation-induced surface patterns [9, 161-163], and the formation of the surface patterns were also studied theoretically.[23, 207] Also, there are experimental and theoretical works on normal convective dewetting of polymer films induced by thermal [208, 209] or solvent annealing. [210] However, most studies have been focused on the evaporative dewetting behavior of a droplet on a rigid substrate without any confinement. There are seldom systematic studies on the evaporative dewetting behavior of a liquid film on a deformable substrate. This study is motivated from the work by Sun and Yang [197], where

they developed a “ring-on-film” template to construct gradient concentric rings both inside and outside a copper ring via evaporating a pure toluene droplet on a pre-cast PMMA film. They observed that a volatile droplet tended to dewet from the periphery to the center without any confinements, while the dewetting of the toluene droplet confined with a copper ring occurred from both the center and periphery towards the copper ring simultaneously. Moreover, the formation of the surface patterns inside the copper ring was associated with the dewetting behavior and the motion of the contact line. It is expected that templates play an important role in controlling the deweting of a droplet and the pattern formation.

It is known that toluene is a good solvent for PMMA. The evaporation of toluene can be significantly influenced by the penetration of toluene in a PMMA film and by the interfacial behaviors of the toluene/PMMA interface, and the evaporation can lead to the motion of the contact line and the formation of well-ordered surface patterns. Considering the important role of the evaporation of a toluene droplet in controlling the surface patterns on PMMA films, we focus on the template-controlled evaporative dewetting of a toluene film on a deformable PMMA film and study the dynamics of the smooth motion of the contact line for the formation of the featureless zone. The effects of the dimensions of the confinement (ring diameter and wire diameter) and the film thickness on the motion of the contact line are examined. A model based on the condition of mechanical equilibrium [51] is presented to qualitatively analyze the experimental results. This will help to understand the mechanisms for the formation of the evaporation-induced surface patterns.

8.2 Experimental

The pre-cast PMMA films were prepared via a spin-coating process at room

temperature. The substrate was glass slide with dimensions of 15×20×1 mm^3, which was cleaned in an acetone bath ultrasonically for three times and then dried with condensed air. The solution for spin-coating was PMMA (Mw=35000) (Fisher Scientific, Pittsburgh, PA) in toluene (Fisher Scientific, Pittsburgh, PA). The spin-coating was performed on a spin coater (WS-400B-6NPP/LITE, Laurell Technologies Corp., North Wales, PA) at 2000 rpm. PMMA thin films of different thicknesses were obtained, using different solution concentrations of 1–4 wt%. Copper rings used to confine the droplets were made of bare copper wires of different wire diameters (ARCOR, Northbrook, IL), which were ultrasonically cleaned in an acetone bath and dried.

The motion of the contact line was examined on pre-cast PMMA films by evaporating pure toluene droplets of 6 μL. The toluene droplets were confined by the copper rings at 298 K. The evaporation process was recorded, using a digital camera with a microscope (Dino-Lite Pro, Torrance, CA) from the bottom of the glass substrate. The position of instant contact lines was determined from the videos recorded by the digital camera. The surface patterns formed on the pre-cast films after complete evaporation were analyzed by an optical microscope (Nikon ECLIPSE LV100POL). All the dimensional measurements were performed with Image Pro plus (Media Cybernetics, Inc., Rockville, MD).

Copper rings of different sizes (1425, 2360, 2900 and 3750 μm) were used to study the size effect of the copper rings on the motion of the contact line. Bare copper wires of different diameters (~51, ~79, and ~102 μm) were used to study the effect of the wire diameter. The evaporation behavior of the droplets on PMMA films of different thicknesses (~90, ~140, ~190 and ~250 nm) were also investigated.

8.3 Results

Figure 8.1a shows the schematic of the evaporation of a toluene droplet confined by a copper ring on a PMMA film. The evaporation of the toluene droplet leads to the formation of a featureless zone around in the center of the ring via the smooth motion of the contact line. The featureless zone is defined as a circular area inside the innermost polymer ring, in which there are no typical structures (features). In the featureless zone, the contact line moves smoothly without any significant pinning. Concentric ring-like patterns induced by a series of "stick-slip" motion of the contact lines [197] are formed in the other region inside the copper ring, The motion of the contact line is controlled by the force balance among surface tensions and the resistance imposed by the PMMA film.

Figure 8.1b-c shows the surface pattern formed on a pre-cast PMMA film after the evaporation of a pure toluene droplet confined by a copper ring. The diameter of the copper wire is 79 μm, and the diameter of the copper ring is 2560 μm. The film thickness is ~140 nm. As shown in Fig. 1b, there are concentric ring-like patterns both inside and outside the copper ring, and there is a featureless zone around the center of the copper ring. The concentric rings formed outside the copper ring is similar to the gradient concentric rings formed via the "sphere-on-flat" geometry, of which both the wavelength and amplitude decrease as the size of the concentric rings decreases. [23, 56, 58] The enlarged view of the local concentric rings inside the copper ring is shown in Fig. 7.1c. The wavelength (distance between adjacent polymer rings) of the concentric rings inside the copper ring gradually decreases with the decrease of the distance to the copper ring, which can be attributed to the confinement of the copper ring on the evaporation of the toluene droplet.

Figure 8.2 shows a typical AFM image of the concentric rings formed on a ~90 nm

PMMA film inside a copper ring with a diameter of 2560 μm. Locally, the segments of concentric rings are parallel to each other. A line perpendicular to the segments, as shown in Fig. 8.2b, is drawn for determining the spatial wavelength of the concentric rings (distance between two adjacent ridges) and the amplitude of the rings. Generally, both the wavelength and the amplitude decrease as the rings approach to the copper ring. The concentric rings outside the copper ring also exhibit the decreasing gradient as the distance to the copper ring decreases. For more information on the features of the gradient concentric rings, see the work by Sun and Yang [197]. In the following, we mainly focus on the featureless zone and the corresponding motion of the contact line.

The featureless zone is formed when the internal contact line reaches the first dynamic "stick" state. As shown in Movie S1 in the supporting information, the evaporation leads to the depletion of the toluene film at the center of the droplet. An internal contact line is formed when the volume of the droplet decreases to a critical volume; the contact line recedes smoothly towards the copper ring until it is pinned to form the smallest internal polymer ring.

Figure 8.3a shows the variation of the size of the featureless zone on the size of the copper rings of three wire diameters. A linear dependence of the size of the featureless zone on the diameter of copper rings is observed. For the same ring size, the size of the featureless zone increases with the decrease of the wire diameter. Using the linear regression to fit the data in Fig. 3a, one obtains

$$D = kd + a, \tag{8.1}$$

with D being the diameter of the featureless zone, d being the size of the copper ring, and k and a being the fitting parameters. Figure 8.3b shows the dependence of k on the wire

diameter. The parameter *k* decreases with the increase of the wire diameter, demonstrating the size effect on the featureless zone. Such behavior is likely associated with the influential zone of a copper ring. Here, the "influential zone" as shown in Fig. 8.1a is defined geometrically as the region between the innermost polymer ring and the copper ring, within which the copper ring significantly influences the evaporative behavior of the droplet and the motion of the contact line and the contact line experiences a series of stick-slip motion. Beyond the influential zone, i.e. in the featureless zone, the copper ring has relatively little effect on the evaporation of the droplet and the contact line moves smoothly and continuously. The size of the "influential zone" is likely determined by the shape, dimensions of the template as well as the interfacial behavior between the toluene film and the PMMA film. Based on the results shown in Fig. 8.3, one can conclude that a copper ring of a larger wire diameter has a larger "influential zone" for the same conditions, i.e. the same ring size and the same thickness of PMMA films. Thus, a copper ring of a larger wire diameter leads to the formation of a featureless zone of a smaller size. The size of the featureless zone is independent of the film thickness for the experimental conditions used, in accord with the results observed by Sun and Yang. [197]

From the results shown in Fig. 8.3 and the above discussions, it is reasonable to infer that the copper ring plays an important role in controlling the dewetting behavior of the droplet. As pointed out by Sun and Yang [189], the resistance exerted on the contact line is dependent on the film thickness. One expects that the film thickness is another important factor determining the smooth motion of the contact line. Thus, the following discussions mainly focus on the effects of the three factors (diameter of copper ring, diameter of copper wire, and film thickness) on the motion of the contact line, respectively.

The temporal evolution of the internal contact line during the evaporation of a toluene droplet on a pre-cast PMMA film of ~250 nm in thickness is presented in Fig. 8.4. The diameter of the copper ring is 1430 μm, which is made of a copper wire of 79 μm in diameter. Before the appearance of the inner contact line, concentric rings already were formed outside the copper ring, as shown in Fig. 8.4a, due to the "stick-slip" motion of the external contact line. The internal contact line is formed when the volume of the droplet decreased to a critical volume, which is mainly determined by the dimensions of the copper ring (i.e. the wire diameter and the ring diameter) [197]. The internal contact line recedes continuously towards the copper ring (Fig. 8.4b-d) until it reaches the first "stick" state (Fig. 8.4d). The polymer ring indicated by the red arrow in Fig. 8.4e was formed at the first "stick" state. After reaching the first "stick" state, the internal contact line continuously receded in a mode of "stick-slip", which can be seen in Movie S1. The "stick-slip" motion leads to the formation of the gradient concentric rings.

Figure 8.5 shows the temporal variation of the internal contact line of a toluene droplet on a PMMA film of ~90 nm in thickness before reaching the first "stick" state. The copper wire diameter is 79 μm. The radius of the internal contact line increases linearly with the evaporation time. Note that the linear relation between the radius of the contact line and time has been observed in all experimental conditions used in this study. This result suggests that the internal contact line moved at a constant velocity. Using the linear regression to fit the experimental data shown in Fig. 8.5, one can calculate the average receding velocity of the contact line over the featureless zone as a function of the diameter of the copper rings.

Figure 8.6 shows the variation of the average receding velocity of the internal contact

line for the evaporation of the toluene droplets on PMMA films of ~90 nm in thickness with the diameter of the copper ring for three wire diameters. The average receding velocity of the contact line increases with the increase in the diameter of the copper ring. For the same diameter of copper rings, the average receding velocity increases with the decrease of the wire diameter. Such behavior suggests that there is an effect of the confinement of the copper ring on the motion of the contact line and the evaporation behavior due to the interaction between the copper wire and the toluene droplet. Toluene partially wets the surface of the bare copper wire, which limits local evaporation of toluene near the copper ring and the amount of toluene between the copper ring and the contact line. Without the presence of a copper ring, a toluene droplet can spread over a PMMA film, forming a thin liquid film with a small contact angle. The ability of confining a toluene droplet is a function of the dimensions of a copper ring (diameter of the copper ring and diameter of the copper wire).

During receding, the thickness of the liquid (toluene) film decreases gradually from the region near the copper ring to the edge of the contact line, and the film evaporates much faster in the vicinity of the contact line than that away from the contact line. The liquid film in the “influential zone” (near the copper ring), which is dependent on the wire diameter, can be considered as a reservoir to replenish the loss of the liquid near the contact line and resist the motion of the contact line. The dimensions of the copper ring (i.e. the wire diameter and the diameter of the ring) regulate the amount of the liquid confined between the copper ring and the contact line and the dynamic contact angle at the contact line, which determines the motion of the contact line. For the copper rings made of the same copper wire, there is less amount of liquid confined by the copper ring of a smaller ring diameter

and the influential zone of the copper ring occupies a larger portion of the space inside the copper ring. The confinement of the copper ring of a smaller diameter to the liquid flow imposes a larger resistance to the receding motion of the contact line and results in a smaller receding velocity. For the same ring size with different wire diameters, the copper ring with a larger wire diameter has a larger "influential zone" and the contact line experiences a larger resistance to its motion. As a result, a larger receding velocity is expected for a copper ring with a smaller wire diameter, in accord with the observation shown in Fig. 8.6.

To illustrate the effect of the confinement, several experiments were performed. Two bare copper wires of 500 and 102 μm in diameter were made into copper rings of the same diameter (3750μm). Two toluene droplets of different volumes were placed near the center of the copper rings on PMMA films of ~140 nm thickness: 15 μL for the copper wire of ~500 μm in diameter and 6 μL for the copper wire of 102 μm in diameter. As shown in Fig. 8.7a and 8.7c, the copper ring made of the larger copper wire (500 μm in diameter) holds the toluene droplet within a circular area of ~7.3 mm in diameter. The toluene droplet spreads to a slightly larger area with ~7.4 mm in diameter, using the copper ring of the smaller copper wire, even though the droplet volume is much smaller. Due to the limitation of the experimental conditions, it is impossible to observe the variation of the contact angle inside a copper ring. Indirectly, the contact angle outside the copper ring has been measured to demonstrate the effect of the size of copper wire on the contact angle and receding velocity inside the copper ring. For the same distance of 550 μm to the copper ring, the contact angle confined by the copper ring of the smaller copper wire is about ~11º (Fig. 8.7d), which is smaller than the contact angle of ~27º by the copper ring of the larger copper

wire (Fig. 6. 7b). This result is consistent with the previous discussion.

As pointed out above, it is impossible to measure the contact angle inside a copper ring. To evaluate the temporal variation of the contact angle during the motion of the contact line, a straight copper wire of 500 μm in diameter and 25 mm in length, which was placed on the surface of a ~140 nm PMMA film, was used to confine the evaporation of a toluene droplet and the motion of the contact line. A toluene droplet of ~60 μL was dripped on the PMMA film with the copper wire at the center. The droplet immediately wetted the copper wire and spread to a shape of a liquid finger with the copper wire at the center, of which the side-view images are shown in Fig. 8.8. It is evident that the contact angle increases with the decrease of the distance to the copper wire, which shows similar trend with the temporal variation of the contact angle outside a copper ring (Fig. 8.7). This result indirectly suggests that the dewetting of a toluene droplet starts at a smaller contact angle for a larger copper ring, resulting in a larger receding speed of the contact line.

Figure 8.9 shows the temporal variation of the radius of the contact line on the PMMA films of different thicknesses before reaching the first “stick” state. The copper ring of 79 μm in the wire diameter and 3750 μm in the ring diameter was used to confine the droplets on different PMMA films. For all the film thicknesses, the radius of the contact line linearly increases with the receding time. The final radii of the contact lines at the first “stick” state, which correspond to the sizes of the featureless zones, are almost the same, independent of the film thickness. However, it takes longer time for the contact line on a thicker film to move the same distance, suggesting that a thicker film has a higher resistance to the motion of the contact line.

Using the linear regression to fit the data shown in Fig. 8.9, one can obtain the average

receding velocity of the contact line before reaching the first "stick" state. Figure 7.10 shows the variation of the average receding velocity of the contact line with film thickness for four ring diameters and the wire diameter of 79 μm. The average receding velocity decreases with the increase of the film thickness. Such behavior likely is attributed to the increase of the viscosity of the toluene/PMMA layer formed at the toluene-PMMA interface. Due to low diffusion rate of PMMA to toluene, high diffusion rate of toluene to PMMA, and the short evaporation time period, the concentration of the PMMA is significantly high at the toluene-PMMA interface. [9] A soft, flowable, viscous layer is formed at the toluene-PMMA interface. The viscosity of the soft, flowable, viscous layer increases with the increase of the film thickness due to the increase of the PMMA concentration. This results in a large resistance to the motion of the contact line on a thick film and the decrease of the average receding velocity with the increase of the film thickness.

8.4 Discussion

Different mechanisms have been proposed to analyze the motion of a contact line, which can be divided into hydrodynamic theories [211-213] and molecular-kinetic theory [214-216]. In principle, it is the force imbalance on a contact line that determines the motion of the contact line. For a contact line experiencing slip motion, the forces acting on the contact line consist of capillary and gravitational forces and the resistance to the motion of the contact line [217]. For a droplet with the characteristic dimension less than the capillary length, the gravitational force is negligible. Accordingly, the equation of motion of the contact line can be expressed as [30]

$$\rho \frac{d^2 x}{dt^2} = \gamma_1 \cos\theta + \gamma_2 - \gamma_3 - \tau, \tag{8.2}$$

where x is the displacement of the contact line, ρ is the line density of mass for the contact line, t is time, γ_1, γ_2 and γ_3 are the surface tensions between toluene-air, toluene-PMMA and air-PMMA, respectively, θ is the nominal contact angle corresponding to the internal contact line, and τ is the resultant line friction (force per unit length). All the parameters are noted in Fig. 1a.

As discussed above, the diffusion of toluene into the PMMA film leads to the formation of a soft, flowable PMMA layer near the interface between the toluene and the PMMA film. The motion of the contact line causes the shear flow of the soft, flowable PMMA layer, which imposes a resistance to the contact line. Considering that the viscosity of toluene is much less than that of the soft, flowable PMMA layer, one can neglect the contribution of the flow in the toluene droplet to the resultant resistance. The line force of τ thus can be expressed as

$$\tau = 1 \cdot \left(\eta \frac{\partial v}{\partial z} \right)_{\text{interface}} \approx \frac{\eta}{h} \frac{dx}{dt}, \tag{8.3}$$

where 1 represents a unit length, η is the viscosity of the soft, flowable PMMA layer, h is the thickness of the soft, flowable layer, and v is tangential velocity. It is known that polymer melt [208] and polymer in solvent (some cases even in poor solvent) [210] are Newtonian fluid, when the polymer chain length is smaller than the entanglement length. In this study, toluene is a good solvent of PMMA with the PMMA chain likely being fully disentangled. Thus, it is reasonable to assume the flowable layer as a Newtonian fluid. Substituting Eq. (8.3) into Eq. (8.2) gives

$$\rho \frac{d^2x}{dt^2} + \frac{\eta}{h}\frac{dx}{dt} = \gamma_1 \cos\theta + \gamma_2 - \gamma_3 . \tag{7.4}$$

Assume that the contact angle can be approximated as a constant value of θ_0 during the smooth motion of the contact line. Using the initial conditions of x=0 and dx/dt=0 at t=0, one obtains the solution of Eq. (8.4) as

$$x(t) = \eta^{-2}[h\eta t - h^2\rho(1 - e^{-\eta t/h\rho})]\left(\gamma_1 \cos\theta_0 + \gamma_2 - \gamma_3\right). \tag{8.5}$$

The displacement of the contact line consists of two terms; one is an exponential function of time with a characteristic time of $\rho h / \eta$, and the other is a linear function of time. To analyze the contribution of the exponential term, consider two extreme cases with the following parameters: (a) h_{min} =90 nm (the thinnest film thickness), η_{max} = 3.16 Pa·s (the viscosity of the toluene-20wt%PMMA solution at 298 K [218]) and ρ_{min}= 0.865 g/ cm^3 (the density of toluene at 298 K), and (b) h_{max} =250 nm (the largest film thickness), η_{min} = 0.5866×10^{-3} Pa·s (the viscosity of pure toluene at 298 K) and ρ_{max}=1.18 g/cm^3 (the density of pure PMMA). The characteristics time is 0.503 s for the parameters of group (a) and 2.46×10^{-5} s for the parameters of group (b). Both are smaller than the time scale used in the experiments. This result suggests that one can neglect the exponential term, and the contact line moves at a constant velocity in accord with the experimental observation.

From Eq. (7.5), one obtains the receding velocity of the contact line as

$$V = \frac{h(\gamma_1 \cos\theta_0 + \gamma_2 - \gamma_3)}{\eta}, \tag{8.6}$$

after neglecting the exponential term. Equation (8.6) is similar to the result obtained from the molecular-kinetic theory [214, 215]. Note that the viscosity in Eq. (8.6) is the viscosity of the soft, flowable PMMA layer in contrast to that of the liquid droplet obtained by Cherry

and Holmes [40] and Blake and Haynes [41].

Effect of ring diameter and wire diameter

For a given film thickness, the soft layer thickness h, viscosity η and density ρ can be considered as constant. The parameters of γ_1, γ_2, and γ_3 are materials properties. According to Eq. (8.6), the nominal contact angle of θ_0 is the only parameter determining the receding velocity of the contact line. From Fig. 8.6, one notes that the average receding velocity of the contact line is a function of the diameter of the copper ring and the wire diameter. This result implies that the nominal contact angle during the slipping of the contact line is dependent on the diameter of the copper ring and the wire diameter. The nominal contact angle decreases with the decrease of the wire diameter and the increase of the diameter of the copper ring in consistent with the results shown in Figs. 8.7 and 8.8. The decrease of the wire diameter and the increase of the diameter of the copper ring have similar effect on increasing the receding velocity of the contact line.

Effect of film thickness

The effect of the film thickness is much more complicated. Both the thickness of the soft layer, h, and the viscosity, η, are dependent on the film thickness of the PMMA film, while they play opposite roles in controlling the motion of the contact line. From Fig. 8.8, the receding velocity decreases with the increase of the film thickness for the same ring diameter and the same wire diameter. This trend suggests that the ratio of h/η decreases with the increase of the film thickness. In general, the thickness of the soft layer, h, will increase with the film thickness. The decrease of the ratio of h/η with the increase of the film thickness indicates that the viscosity of η increases much more significantly. Note that it is very difficult, if not impossible, to individually measure the thickness and viscosity of

the soft layer. Thus, it would be reasonable to introduce the concept of an interface viscosity as $\eta_{int}=\eta/h$, and Eq. (8.6) can be rewritten as

$$V = \frac{\gamma_1 \cos\theta_0 + \gamma_2 - \gamma_3}{\eta_{int}} . \tag{8.7}$$

The receding velocity of the contact line is inversely proportional to the interface viscosity between the toluene and the PMMA substrate.

8.5 Conclusion

In summary, we have studied the dewetting behavior of a pure toluene film confined within a copper ring on a pre-cast PMMA thin film. The experimental results demonstrate the important role of the copper ring in controlling the evaporative dewetting. With the confinement of a copper ring, the toluene film dewets first at the center of the copper ring due to the evaporation, which resultes in the formation of an internal contact line. The internal contact line recedes smoothly towards the copper ring at a constant velocity until being pinned to form the smallest PMMA ring inside the copper ring in contrast to the free evaporative dewetting without any templates. The receding velocity is a function of the geometrical configuration of the copper ring (the ring diameter and the wire diameter) and the film thickness under the condition of constant evaporation rate. A transition of the internal dewetting from smooth dewetting into a “stick-slip” mode is observed, resulting in the formation of gradient concentric rings. The experimental results shed insight into the mechanisms controlling the motion of the contact line on deformable substrates and the important factors determining the dewetting kinetics.

In general, one can control the dewetting behavior of a liquid film via the use of a simple or complicated template to confine the evaporation behavior and the motion of the

contact line without altering the surface properties of substrates. This study reveals the potential of using templets to engineering surface structures on polymer films by using volatile liquids for potential applications in flexible electronics, micro and nao-fluidics, and bio-devices.

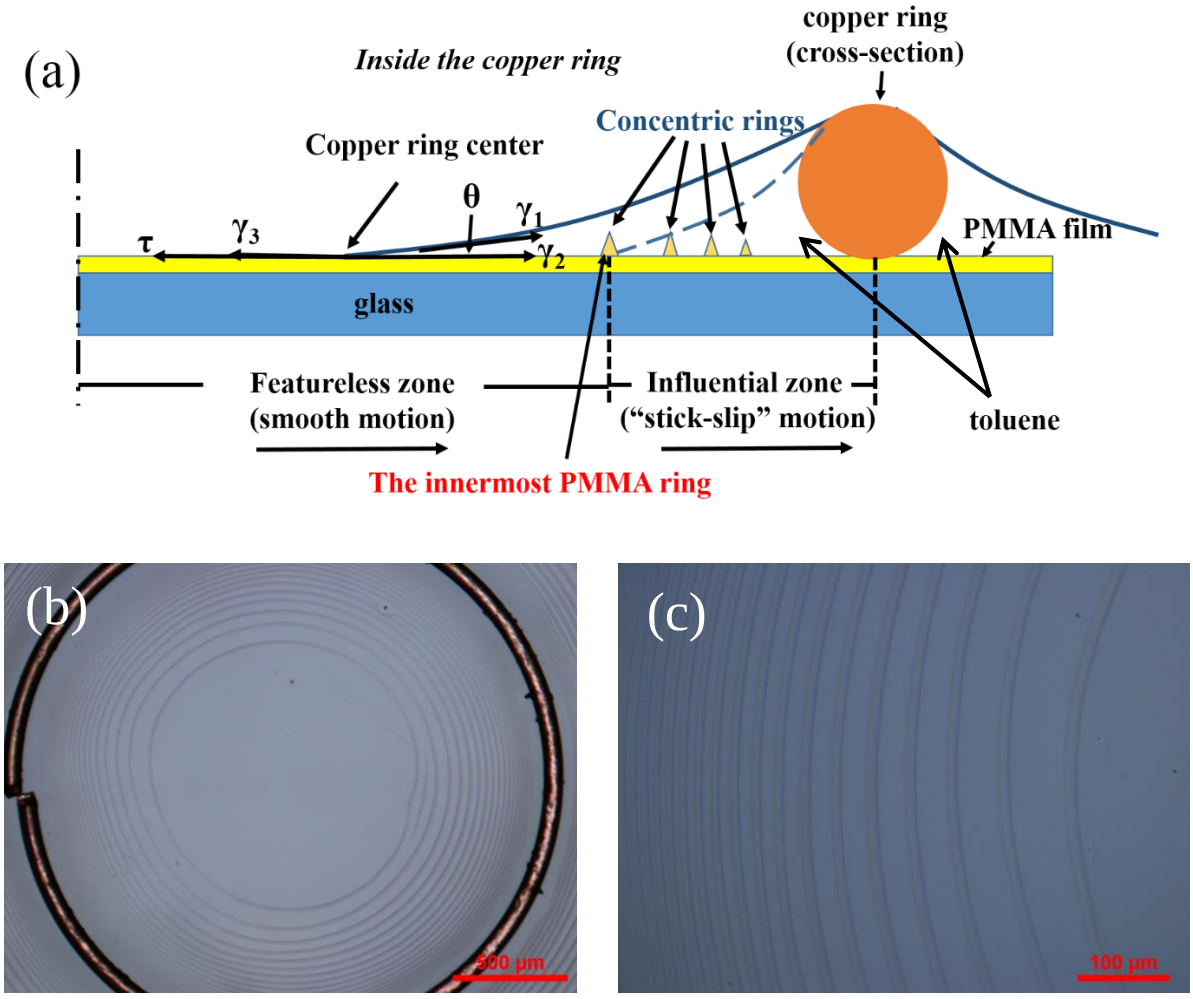

Figure 8.1 (a) Schematic of the cross section of a toluene droplet confined by a copper ring on a PMMA film; (b-c) Optical images of the evaporation–induced gradient concentric rings on a pre-cast PMMA film (film thickness: ~140 nm; diameter of the copper ring: 2560 μm); (b) a large view of the surface pattern, and (c) an enlarged view of the pattern inside the copper ring.

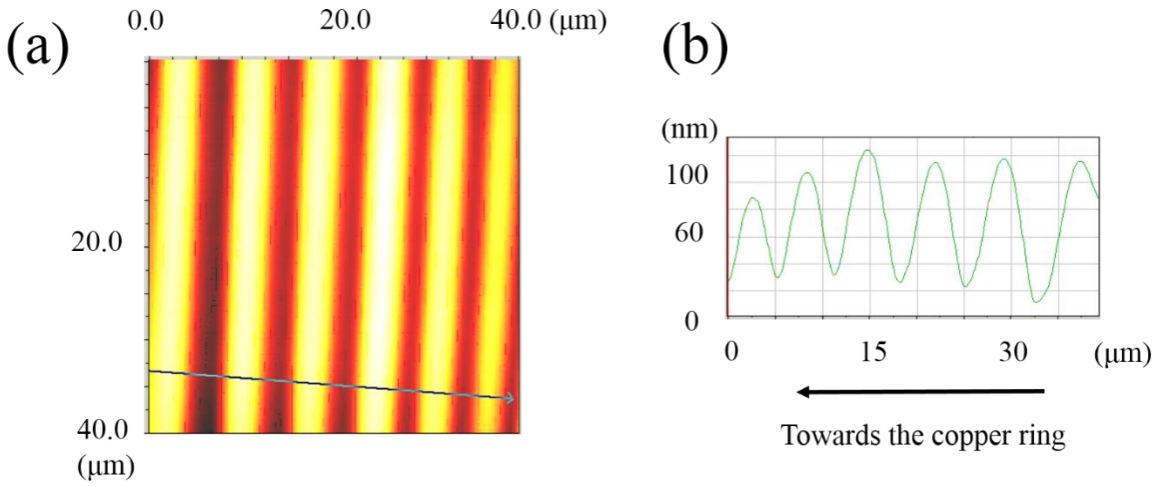

Figure 8.2(a) AFM image of the concentric rings over an area of 40×40 μm^2, and (b) surface profile of the concentric rings. (film thickness: ~90 nm; diameter of the copper ring: 2560 μm)

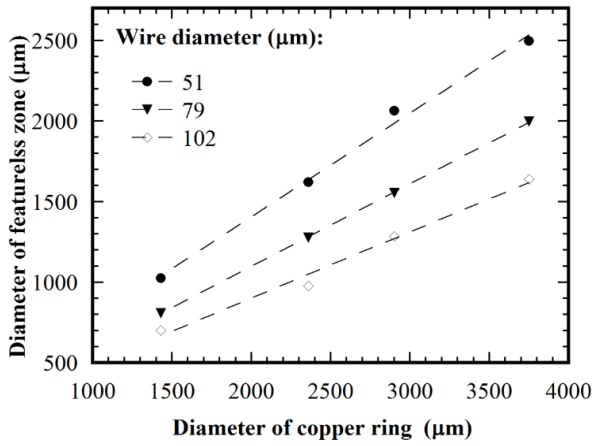

(a)

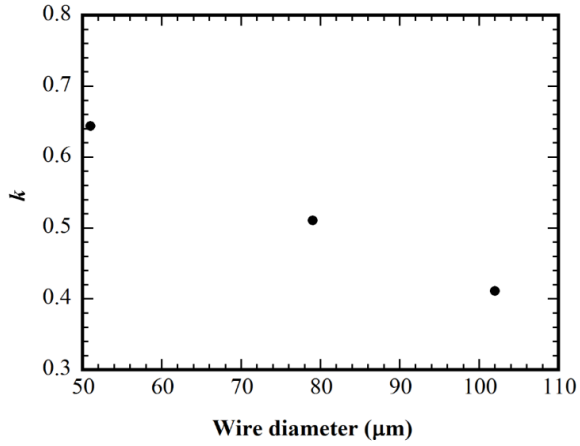

(b)

Figure 8.3(a) Variation of the size of the featureless zone with the diameter of the copper rings of three wire diameters for the patterns formed on the PMMA films of ~90 nm thickness, and (b) variation of the slope of the linear fitting of the results in (a) with the wire diameter.

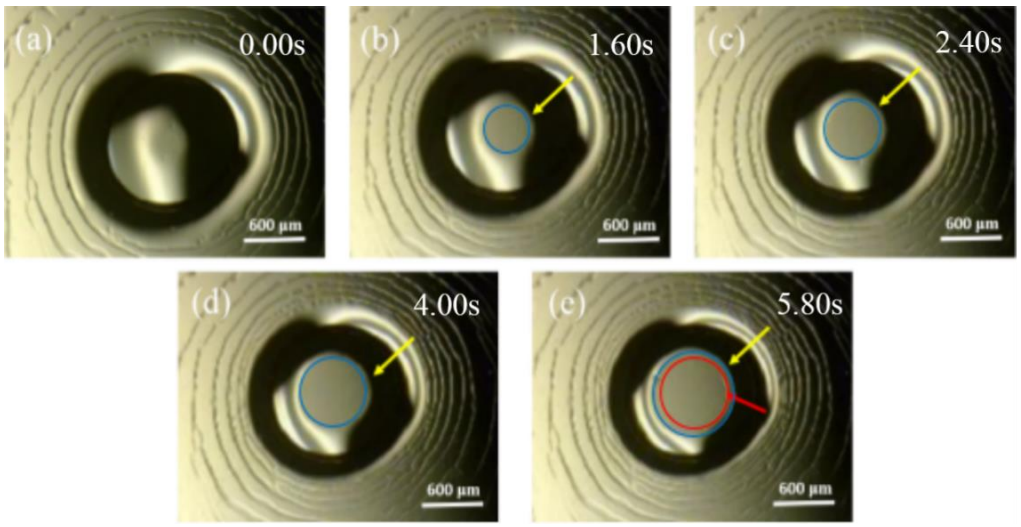

Figure 8.4 Temporal evolution of the contact line; (a) just before the appearance of the contact line; (b) 1.60 s after the appearance of the contact line; (c) 2.40 s after the appearance of the contact line; (d) 4 s after the appearance of the contact line (the contact line reached the first "stick" state); (e) 5.80 s after the appearance of the contact line. The yellow arrow indicates the contact line (blue circle), and the red arrow indicates the smallest polymer ring (red circle). (Copper ring diameter: 1430 μm; cross-sectional diameter of the copper wire: 79 μm; film thickness: ~250 nm)

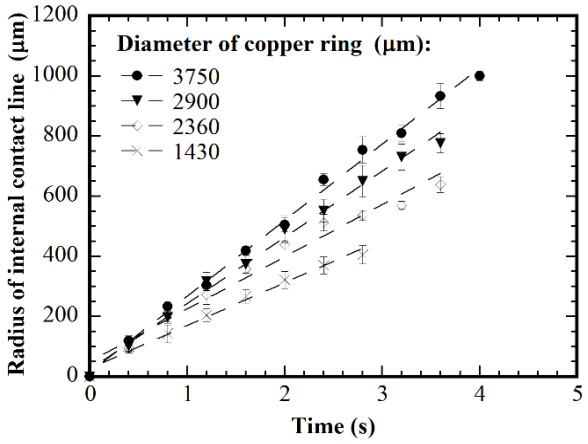

Figure 8.5 Temporal variation of the radius of the internal contact for four copper ring diameters (diameter of the copper wire: 79 μm; film thickness: ~90 nm). The time for the onset of the internal contact line is referred to as the reference time (0s).

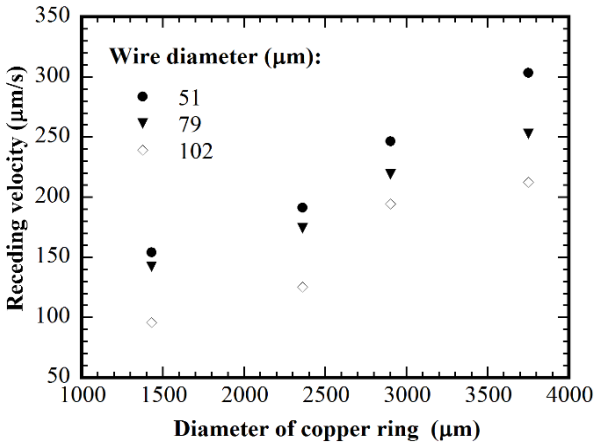

Figure 8.6 Variation of the average receding velocity of the contact line with the diameter of copper ring for three wire diameters (film thickness: ~90 nm)

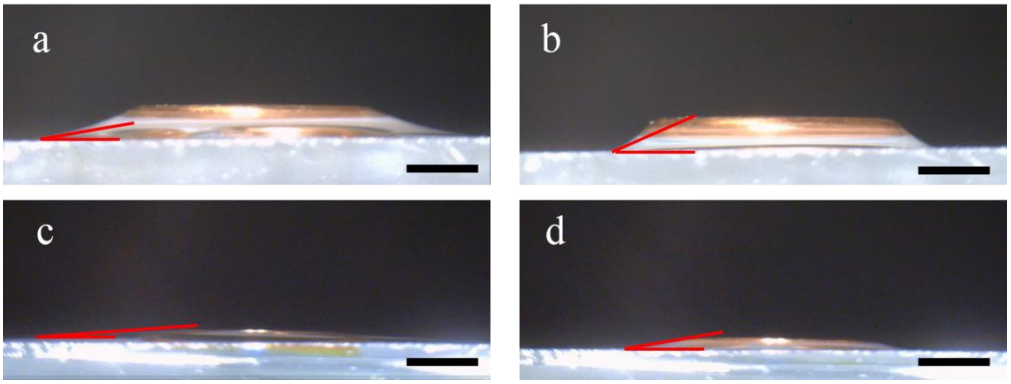

Figure 8.7 Side-view of the digital images of a toluene droplet confined by a copper ring of 3750 μm in diameter on a ~140 nm PMMA film: (a) a 15μL toluene droplet confined by a copper ring made of a copper wire of 500 μm in diameter (t=0 s); (b) side-view of the toluene film in (a) after ~70 s, the distance from the contact to the copper wire is 550 μm; (c) a 6μL toluene droplet confined by a copper ring made of a copper wire of 102 μm in diameter (t=0 s); (d) side-view of the toluene film in (c) after ~34 s, the distance from the contact to the copper wire is 550 μm. The nominal contact angle is noted by red lines. The scale bars in all the images represent 1 mm.

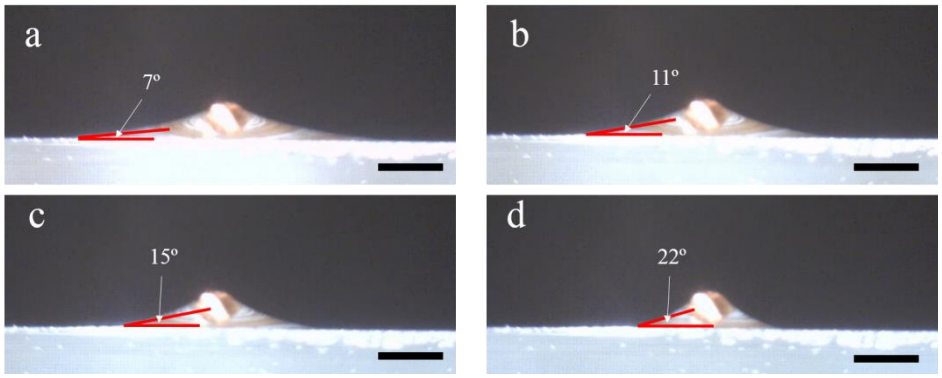

Figure 8.8 Side-view of the digital images of a toluene droplet confined by a straight copper wire of 25 mm in length and 500 μm in diameter. The distance from the contact line to the copper wire: (a) 1875 μm; (b) 1450 μm; (c) 1180 μm and (d) 715 μm. The nominal contact angle is noted by red line. The scale bars in all the images represent 1 mm.

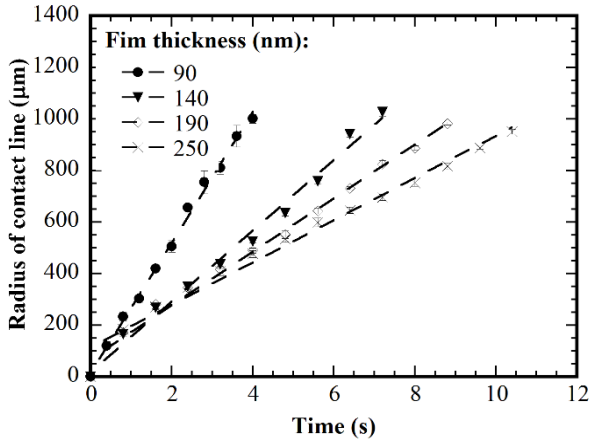

Figure 8.9 Variation of the radius of the internal contact line with time for four film thicknesses (diameter of copper wire: 79 μm; diameter of copper ring: 3750 μm). The time for the onset of the internal contact line is referred to as the reference time (0s).

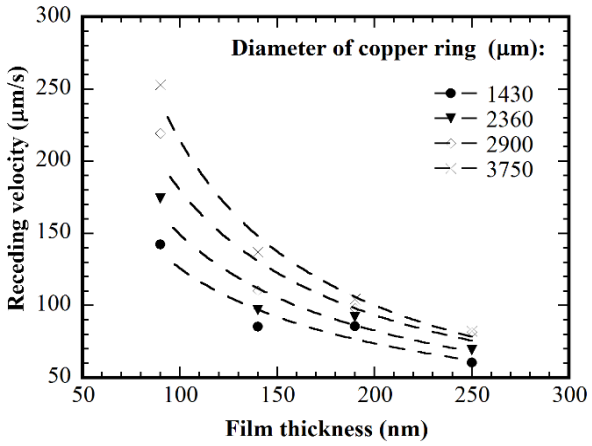

Figure 8.10 Variation of the average receding velocity of the contact line with film thickness for four ring diameters (wire diameter: 79 μm)

Chapter 9. Summary

9.1 Conclusion

With the potential applications of surface structures of small scales in various areas, including electronics, photonics, biosensors, optical devices, etc, more and more studies have been focused on the fabrication of well-ordered surface patterns. In this dissertation, we tried to construct various regular surface patterns in microscales via an efficient and economic strategy. We developed a “template-controlled-evaporation-induced” technique and fabricated polymer surface patterns with various geometries and controllable dimensional characteristics. The mechanisms behind the formation of the surface patterns and the kinetics of the dewetting of a liquid film on a deformable substrate have been investigated.

A “particle-on-film” template was developed, in which a SiC particle was placed on a pre-cast PMMA film. A toluene droplet was then placed onto the PMMA film with the particle at the center. Concentric-ring-like patterns were formed as the contact line experienced as series of the “advancing-receding” motions. Both the wavelength and amplitude decrease with the decrease of the distance to the particle. The surface patterns are found to significantly depend on the particle size and the film thickness. The wavelength formed with a larger SiC particle is larger than that with a smaller particle. The similar tendency is also found for the ratio of amplitude versus the wavelength. The wavelength and amplitude also increase with the increase of the film thickness. A simple model based on the force balance on the contact line is developed to analyze the motion of the contact line.

A straight copper wire was also used as a template for the fabrication of the evaporation-induced surface patterns on pre-cast PMMA film. By evaporating a toluene droplet on PMMA film with a straight copper wire, straight multiple stripe patterns were formed on both sides of the copper wire. Both the wavelength and amplitude increase with the increase of the distance to the copper wire. The dimensions of the stripes can be controlled by using copper wires of different cross-sectional diameters. When an additional copper wires with the same diameter is placed parallel to the original one with a distance between them, gradient multiple straight stripes can be formed along both the copper wires, with a featureless zone between the two copper wires. The size of the featureless zone increases with the distance between the two copper wires and decreases with the increase of the copper wire diameter.

A circular copper ring was used as a template for the fabrication of the evaporation-induced surface patterns on pre-cast PMMA film. Gradient concentric rings were formed both inside and outside the copper ring. The wavelength and amplitude decrease as the distance to the copper ring decreases for both the patterns formed inside and outside the copper ring. A circular featureless zone was formed at the center of the copper ring. The wavelength increases with the decrease of the copper ring size for concentric rings formed both inside and outside the copper ring. The ratio of the amplitude versus the wavelength increases with the decrease of the copper ring size for the patterns formed outside the copper ring, while the opposite tendency is observed for the patterns formed inside the copper ring. By increasing the film thickness, both the wavelength and amplitude can be increased.

Instead of using a droplet of pure solvent, a droplet of PMMA solution in toluene was

evaporated on a cleaned glass slide. The size of copper ring, solution concentration have similar effects on the characteristics of the concentric ring patterns formed to those in the previous studies. The effect of substrate temperature was also investigated. The wavelength increases with the increase of the substrate temperature from 21℃ to 55℃; the ratio of the amplitude to the wavelength decreases with the increase of the substrate temperature. Microscale patterns were observed in the trenches between two polymer ridges, which is dependent on the wavelength and the substrate temperature.

Finger-like patterns were constructed by confining a toluene bridge between a tilt carbon rod and a flat PMMA film. With the template-controlled evaporation, multiple arcs were formed in the middle area of the finger, while multiple stripes were formed in the side area parallel to the symmetric axis. Along the symmetric axis, the wavelength of the arcs decreases first to reach a minimum value and then increases. The dimensions of the fingers as well as the wavelength of the arcs is dependent on the droplet volume and tilt angle. Using this approach, a "cross-like" pattern, which consists of four finger-like patterns was constructed.

Hexagonal network was fabricated by a "breath figure" method at low humidity and low substrate temperature with a copper ring as a template. Irregular holes were formed in the centric area, and regular hexagonal network was formed in the circular area near the copper ring. The size of the holes increases with the decrease of the film thickness. The hole size formed by a copper ring with a larger wire diameter or ring diameter is larger than that formed with a copper ring with a smaller dimension. The regularity of the hexagonal network formed at a relatively higher substrate temperature is higher than that formed at lower temperatures.

The dewetting dynamics of a toluene film confined within a copper ring on a deformable PMMA film was studied. The toluene film experienced evaporation and dewetting, which led to the formation of a circular contact line near the center of the copper ring. The contact line receded smoothly toward the copper ring at a constant velocity until reaching a dynamic "stick" state to form the first circular polymer ridge. The average receding velocity is dependent on the dimensions of the copper ring (the copper ring diameter and the cross-sectional diameter of the copper wire) and the thickness of the PMMA films. The average receding diameter decreases with the increase of the cross-sectional diameter or decrease of the copper ring diameter. Increasing the film thickness led to the decrease of the average receding velocity. A model was presented to qualitatively explain the evaporative dewetting phenomenon.

9.2 Future work

In this work, various surface morphologies have been constructed on PMMA films by the evaporation of solvent with the use of simple templates. Several parameters have been changed to examine the variation of the geometry and dimensional characteristics. The following is a list of future works with can explore the potential applications of the techniques developed in this work.

9.2.1 Fabrication of evaporation-induced patterns with non-volatile materials

In this work, we developed several templates for the evaporation-induced surface patterns. It would be necessary to extend this technique to various other types of materials, including block copolymer, biomolecule, nanoparticles, carbon nanotubes, graphene, etc. The patterns formed with functional materials can have potential applications in various fields. Depending on the properties of materials, substrate, solvent, temperatures,

experimental conditions need to be properly controlled in order to construct well-ordered patterns.

9.2.2 Development of new templates

The patterns formed in this work vary from concentric rings, straight stripes to finger-like patterns and cover a relatively large area. However the patterns are always with gradients of wavelength and amplitude. In the future, we need to develop different templates to assist the fabrication of the surface patterns in various geometries with uniform dimensional characteristics. In addition, the surface patterning over a much larger area needs to be investigated for future applications.

9.2.3 Formation mechanisms of surface patterns

The evaporation-induced patterns is controlled by a series of "stick-slip" motion of the contact line. There are several mechanisms controlling the motion of the contact line, for example, the microflow inside the droplet in order to balance the mass loss, thermal Marangoni flow, solutal Marangoni flow, etc. In this work, we provided a qualitative model based on the force balance exerted on the contact line to explain the oscillation of the contact line. In the future, more quantitative work and simulation need to be done to further explain the motion of the contact line and formation of patterns. The effects of experimental parameters on the patterns would need to be quantitatively studied.

9.2.4 Applications of the surface patterns

The work in this dissertation focuses on the fabrication of surface patterns via the evaporation of a solvent droplet and on the control of the pattern geometries. In the future, we need to explore the application of the surface patterns in several fields, including optical devices, gas sensors, electronics and bio-devices. To realize practical applications, surface

patterns likely will be further developed. For example, the patterns should cover a larger area, the patterns should be functional (i.e. conductive and/or with functional groups on the surface), and be biocompatible (for biomedical applications).

References

(1) Sun, L., et al., 12-GHz Thin-Film Transistors on Transferrable Silicon Nanomembranes for High-Performance Flexible Electronics. Small, 2010. 6(22): p. 2553-2557.

(2) Kolaric, B., et al., In situ tuning the optical properties of a cavity by wrinkling. Applied Physics Letters, 2010. 96(4).

(3) Langer, R. and D.A. Tirrell, Designing materials for biology and medicine. Nature, 2004. 428(6982): p. 487-492.

(4) Lim, J.Y. and H.J. Donahue, Cell sensing and response to micro- and nanostructured surfaces produced by chemical and topographic patterning. Tissue Engineering, 2007. 13(8): p. 1879-1891.

(5) Chan, E.P., et al., Surface wrinkles for smart adhesion. Advanced Materials, 2008. 20(4): p. 711-716.

(6) Zhou, W.M., et al., Nanoimprint Lithography: A Processing Technique for Nanofabrication Advancement. Nano-Micro Letters, 2011. 3(2): p. 135-140.

(7) Walheim, S., et al., Structure formation via polymer demixing in spin-cast films. Macromolecules, 1997. 30(17): p. 4995-5003.

(8) Deegan, R.D., et al., Contact line deposits in an evaporating drop. Physical Review E, 2000. 62(1): p. 756-765.

(9) Gonuguntla, M. and A. Sharma, Polymer patterns in evaporating droplets on dissolving substrates. Langmuir, 2004. 20(8): p. 3456-3463.

(10) Hong, S.W., et al., Simple route to gradient concentric metal and metal oxide rings.

Chemistry of Materials, 2006. 18(22): p. 5164-5166.

(11) Han, W., et al., Large‐Scale Hierarchically Structured Conjugated Polymer Assemblies with Enhanced Electrical Conductivity. Angewandte Chemie International Edition, 2013.

(12) Khang, D.Y., et al., A stretchable form of single-crystal silicon for high-performance electronics on rubber substrates. Science, 2006. 311(5758): p. 208-212.

(13) Koo, W.H., et al., Light extraction from organic light-emitting diodes enhanced by spontaneously formed buckles. Nature photonics, 2010. 4(4): p. 222-226.

(14) Lin, P.-C., et al., Mechanically tunable dry adhesive from wrinkled elastomers. Soft Matter, 2008. 4(9): p. 1830-1835.

(15) Hatakeyama, H., et al., Patterned biofunctional designs of thermoresponsive surfaces for spatiotemporally controlled cell adhesion, growth, and thermally induced detachment. Biomaterials, 2007. 28(25): p. 3632-3643.

(16) Fukuhira, Y., et al., Biodegradable honeycomb-patterned film composed of poly(lactic acid) and dioleoylphosphatidylethanolamine. Biomaterials, 2006. 27(9): p. 1797-1802.

(17) Kikuchi, A. and T. Okano, Nanostructured designs of biomedical materials: Applications of cell sheet engineering to functional regenerative tissues and organs. Journal of Controlled Release, 2005. 101(1-3): p. 69-84.

(18) Pease, L.F., et al., Self-formation of sub-60-nm half-pitch gratings with large areas through fracturing. Nature Nanotechnology, 2007. 2(9): p. 545-548.

(19) Liang, P.-Y., F. Yang, and S. Lee, Fracture-induced formation of semi-concentric

patterns on polymeric films. Materials Chemistry and Physics, 2012. 135(1): p. 168-173.

(20) Uchiyama, H., D. Shimaoka, and H. Kozuka, Spontaneous pattern formation based on the coffee-ring effect for organic-inorganic hybrid films prepared by dip-coating: effects of temperature during deposition. Soft Matter, 2012. 8(44): p. 11318-11322.

(21) Zhang, X.H., J.F. Douglas, and R.L. Jones, Influence of film casting method on block copolymer ordering in thin films. Soft Matter, 2012. 8(18): p. 4980-4987.

(22) Deegan, R.D., Pattern formation in drying drops. Physical Review E, 2000. 61(1): p. 475-485.

(23) Xu, J., et al., Self-assembly of gradient concentric rings via solvent evaporation from a capillary bridge. Physical Review Letters, 2006. 96(6).

(24) Deegan, R.D., et al., Capillary flow as the cause of ring stains from dried liquid drops. Nature, 1997. 389(6653): p. 827-829.

(25) Poulard, C. and P. Damman, Control of spreading and drying of a polymer solution from Marangoni flows. Epl, 2007. 80(6).

(26) Beattie, D., et al., Honeycomb-structured porous films from polypyrrole-containing block copolymers prepared via RAFT polymerization as a scaffold for cell growth. Biomacromolecules, 2006. 7(4): p. 1072-1082.

(27) Thomas, K.R., et al., Wetting induced instabilities in miscible polymer blends. Soft Matter, 2010. 6(15): p. 3517-3523.

(28) Cavallini, M., et al., Ordered patterning of nanometric rings of single molecule magnets on polymers by lithographic control of demixing. Journal of Physical Chemistry B, 2006. 110(24): p. 11607-11610.

(29) Ton-That, C., et al., Effects of annealing on the surface composition and morphology of PS/PMMA blend. Macromolecules, 2000. 33(22): p. 8453-8459.

(30) Dekeyser, C.M., et al., Submicrometer-scale heterogeneous surfaces by PS-PMMA demixing. Polymer, 2004. 45(7): p. 2211-2219.

(31) Geldhauser, T., et al., Generation of Surface Energy Patterns by Single Pulse Laser Interference on Self-Assembled Monolayers. Langmuir, 2008. 24(22): p. 13155-13160.

(32) Minelli, C., et al., Organization of nanoscale objects via polymer demixing. Colloid and Polymer Science, 2004. 282(11): p. 1274-1278.

(33) Chou, S.Y., P.R. Krauss, and P.J. Renstrom, Nanoimprint lithography. Journal of Vacuum Science & Technology B, 1996. 14(6): p. 4129-4133.

(34) Chou, S.Y., P.R. Krauss, and P.J. Renstrom, IMPRINT OF SUB-25 NM VIAS AND TRENCHES IN POLYMERS. Applied Physics Letters, 1995. 67(21): p. 3114-3116.

(35) Schift, H., Nanoimprint lithography: An old story in modern times? A review. Journal of Vacuum Science & Technology B, 2008. 26(2): p. 458-480.

(36) Torres, C.S., *Alternative lithography: unleashing the potentials of nanotechnology*. 2003: Springer.

(37) Peng, C., et al., High fidelity fabrication of microlens arrays by nanoimprint using conformal mold duplication and low-pressure liquid material curing. Journal of Vacuum Science & Technology B, 2007. 25(2): p. 410-414.

(38) Khang, D.Y., et al., Low-pressure nanoimprint lithography. Nano Letters, 2004. 4(4): p. 633-637.

(39) Xia, Q.F. and S.Y. Chou, Applications of excimer laser in nanofabrication. Applied

Physics a-Materials Science & Processing, 2010. 98(1): p. 9-59.

(40) Wu, W., et al., Room-temperature Si single-electron memory fabricated by nanoimprint lithography. Applied Physics Letters, 2003. 83(11): p. 2268-2270.

(41) Dai, S.X., et al., Fabrication of surface-patterned ZnO thin films using sol-gel methods and nanoimprint lithography. Journal of Sol-Gel Science and Technology, 2011. 60(1): p. 17-22.

(42) Genzer, J. and J. Groenewold, Soft matter with hard skin: From skin wrinkles to templating and material characterization. Soft Matter, 2006. 2(4): p. 310-323.

(43) Zhao, Y., W.M. Huang, and Y.Q. Fu, Formation of micro/nano-scale wrinkling patterns atop shape memory polymers. Journal of Micromechanics and Microengineering, 2011. 21(6).

(44) Bowden, N., et al., Spontaneous formation of ordered structures in thin films of metals supported on an elastomeric polymer. Nature, 1998. 393(6681): p. 146-149.

(45) Huck, W.T.S., et al., Ordering of spontaneously formed buckles on planar surfaces. Langmuir, 2000. 16(7): p. 3497-3501.

(46) Bowden, N., et al., The controlled formation of ordered, sinusoidal structures by plasma oxidation of an elastomeric polymer. Applied Physics Letters, 1999. 75(17): p. 2557-2559.

(47) Lin, T.-C., et al., Alignment control of liquid crystal molecules using crack induced self-assembled grooves. Soft Matter, 2009. 5(19): p. 3672-3676.

(48) Cai, Y.J. and B.M.Z. Newby, Fracture-induced formation of parallel silicone strips. Journal of Materials Research, 2010. 25(5): p. 803-809.

(49) Liang, P.Y., F.Q. Yang, and S. Lee, Fracture-induced formation of semi-concentric

patterns on polymeric films. Materials Chemistry and Physics, 2012. 135(1): p. 168-173.

(50) Bi, W.G., X.Y. Wu, and E.K.L. Yeow, Unconventional Multiple Ring Structure Formation from Evaporation-Induced Self-Assembly of Polymers. Langmuir, 2012. 28(30): p. 11056-11063.

(51) Adachi, E., A.S. Dimitrov, and K. Nagayama, STRIPE PATTERNS FORMED ON A GLASS-SURFACE DURING DROPLET EVAPORATION. Langmuir, 1995. 11(4): p. 1057-1060.

(52) Vivero‐Escoto, J.L., et al., Mesoporous silica nanoparticles for intracellular controlled drug delivery. Small.

(53) Kajiya, T., D. Kaneko, and M. Doi, Dynamical Visualization of "Coffee Stain Phenomenon" in Droplets of Polymer Solution via Fluorescent Microscopy. Langmuir, 2008. 24(21): p. 12369-12374.

(54) Palberg, T. and K. Streicher, RESONANT STICK-SLIP MOTION IN A COLLOIDAL CRYSTAL. Nature, 1994. 367(6458): p. 51-54.

(55) Baumberger, T., F. Heslot, and B. Perrin, CROSSOVER FROM CREEP TO INERTIAL MOTION IN FRICTION DYNAMICS. Nature, 1994. 367(6463): p. 544-546.

(56) Lin, Z.Q. and S. Granick, Patterns formed by droplet evaporation from a restricted geometry. Journal of the American Chemical Society, 2005. 127(9): p. 2816-2817.

(57) Hong, S.W., J. Xia, and Z. Lin, Spontaneous formation of mesoscale polymer patterns in an evaporating bound solution. Advanced Materials, 2007. 19(10): p. 1413-+.

(58) Byun, M., et al., Evaporative Organization of Hierarchically Structured Polymer Blend Rings. Macromolecules, 2008. 41(23): p. 9312-9317.

(59) Byun, M., et al., Self-assembling semicrystalline polymer into highly ordered, microscopic concentric rings by evaporation. Langmuir, 2008. 24(7): p. 3525-3531.

(60) Hong, S.W., et al., Directed self-assembly of gradient concentric carbon nanotube rings. Advanced Functional Materials, 2008. 18(14): p. 2114-2122.

(61) Byun, M., et al., An Unconventional Route to Hierarchically Ordered Block Copolymers on a Gradient Patterned Surface through Controlled Evaporative Self‐Assembly. Angewandte Chemie International Edition, 2013. 52(4): p. 1122-1127.

(62) Li, B., et al., Flow‐Enabled Self‐Assembly of Large‐Scale Aligned Nanowires. Angewandte Chemie International Edition, 2015. 54(14): p. 4250-4254.

(63) Xiao, L., et al., Formation of Gradient Multiwalled Carbon Nanotube Stripe Patterns by Using Evaporation-Induced Self-Assembly. ACS Applied Materials & Interfaces, 2012. 4(8): p. 3811-3817.

(64) KyuáPark, W., et al., Large-scale patterning by the roll-based evaporation-induced self-assembly. Journal of Materials Chemistry, 2012. 22(43): p. 22844-22847.

(65) Kim, T., et al., Large-scale graphene micropatterns via self-assembly-mediated process for flexible device application. Nano letters, 2012. 12(2): p. 743-748.

(66) Yabu, H. and M. Shimomura, Preparation of self-organized mesoscale polymer patterns on a solid substrate: Continuous pattern formation from a receding meniscus. Advanced Functional Materials, 2005. 15(4): p. 575-581.

(67) Zhang, Z., et al., Controlled Inkjetting of a Conductive Pattern of Silver

Nanoparticles Based on the Coffee‐Ring Effect. Advanced Materials, 2013. 25(46): p. 6714-6718.

(68) Lin, Y., et al., Self-Assembly of Virus Particles on Flat Surfaces via Controlled Evaporation†. Langmuir, 2010. 27(4): p. 1398-1402.

(69) Majumder, M., et al., Overcoming the "Coffee-Stain" Effect by Compositional Marangoni-Flow-Assisted Drop-Drying. Journal of Physical Chemistry B, 2012. 116(22): p. 6536-6542.

(70) Uchiyama, H., M. Hayashi, and H. Kozuka, Spontaneous pattern formation on silica and titania dip-coating films prepared at extremely low substrate withdrawal speeds. Rsc Advances, 2012. 2(2): p. 467-473.

(71) Soltman, D. and V. Subramanian, Inkjet-printed line morphologies and temperature control of the coffee ring effect. Langmuir, 2008. 24(5): p. 2224-2231.

(72) Tirumkudulu, M.S. and W.B. Russel, Role of capillary stresses in film formation. Langmuir, 2004. 20(7): p. 2947-2961.

(73) Hu, H. and R.G. Larson, Marangoni effect reverses coffee-ring depositions. Journal of Physical Chemistry B, 2006. 110(14): p. 7090-7094.

(74) Hu, H. and R.G. Larson, Analysis of the microfluid flow in an evaporating sessile droplet. Langmuir, 2005. 21(9): p. 3963-3971.

(75) Reiter, G., UNSTABLE THIN POLYMER-FILMS - RUPTURE AND DEWETTING PROCESSES. Langmuir, 1993. 9(5): p. 1344-1351.

(76) Fondecave, R. and F.B. Wyart, Polymers as dewetting agents. Macromolecules, 1998. 31(26): p. 9305-9315.

(77) Vuilleumier, R., et al., TEARS OF WINE - THE STATIONARY STATE. Langmuir,

1995. 11(10): p. 4117-4121.

(78) Silvi, N. and E.B. Dussan, ON THE REWETTING OF AN INCLINED SOLID-SURFACE BY A LIQUID. Physics of Fluids, 1985. 28(1): p. 5-7.

(79) Huppert, H.E., FLOW AND INSTABILITY OF A VISCOUS CURRENT DOWN A SLOPE. Nature, 1982. 300(5891): p. 427-429.

(80) Melo, F., J.F. Joanny, and S. Fauve, FINGERING INSTABILITY OF SPINNING DROPS. Physical Review Letters, 1989. 63(18): p. 1958-1961.

(81) Sharma, A. and G. Reiter, Instability of thin polymer films on coated substrates: Rupture, dewetting, and drop formation. Journal of Colloid and Interface Science, 1996. 178(2): p. 383-399.

(82) Nishikawa, T., et al., Honeycomb-patterned thin films of amphiphilic polymers as cell culture substrates. Materials Science and Engineering: C, 1999. 8–9(0): p. 495-500.

(83) Li, L., et al., Robust and hydrophilic polymeric films with honeycomb pattern and their cell scaffold applications. Journal of Materials Chemistry, 2009. 19(18): p. 2789-2796.

(84) Heng, L., et al., Enhancement of photocurrent generation by honeycomb structures in organic thin films. ChemPhysChem, 2006. 7(12): p. 2520-2525.

(85) Yabu, H. and M. Shimomura, Simple fabrication of micro lens arrays. Langmuir, 2005. 21(5): p. 1709-1711.

(86) Campbell, M., et al., Fabrication of photonic crystals for the visible spectrum by holographic lithography. Nature, 2000. 404(6773): p. 53-56.

(87) Davis, M.E., Ordered porous materials for emerging applications. Nature, 2002.

417(6891): p. 813-821.

(88) Ma, C.-Y., et al., Patterned carbon nanotubes with adjustable array: a functional breath figure approach. Chemistry of Materials, 2010. 22(7): p. 2367-2374.

(89) Widawski, G., M. Rawiso, and B. François, Self-organized honeycomb morphology of star-polymer polystyrene films. 1994.

(90) Karthaus, O., et al., Water-assisted formation of micrometer-size honeycomb patterns of polymers. Langmuir, 2000. 16(15): p. 6071-6076.

(91) Connal, L.A. and G.G. Qiao, Honeycomb coated particles: porous doughnuts, golf balls and hollow porous pockets. Soft Matter, 2007. 3(7): p. 837-839.

(92) Karthaus, O., et al., Mesoscopic 2-D ordering of inorganic/organic hybrid materials. Materials Science and Engineering: C, 1999. 10(1–2): p. 103-106.

(93) Yu, Y. and Y. Ma, Breath figure fabrication of honeycomb films with small molecules through hydrogen bond mediated self-assembly. Soft Matter, 2011. 7(3): p. 884-886.

(94) Xu, Y., B. Zhu, and Y. Xu, A study on formation of regular honeycomb pattern in polysulfone film. Polymer, 2005. 46(3): p. 713-717.

(95) Cong, H., et al., Preparation of a highly permeable ordered porous microfiltration membrane of brominated poly (phenylene oxide) on an ice substrate by the breath figure method. Soft Matter, 2012. 8(34): p. 8835-8839.

(96) Jiang, X., et al., Surfactant-induced formation of honeycomb pattern on micropipette with curvature gradient. Langmuir, 2011. 27(9): p. 5410-5419.

(97) Wang, Z., et al., Condensed solute droplets templated honeycomb pattern on polymer films. Journal of colloid and interface science, 2014. 436: p. 16-18.

(98) Nishikawa, T., et al., Fabrication of honeycomb film of an amphiphilic copolymer at the air-water interface. Langmuir, 2002. 18(15): p. 5734-5740.

(99) De Gennes, P.-G., F. Brochard-Wyart, and D. Quéré, *Capillarity and wetting phenomena: drops, bubbles, pearls, waves*. 2004: Springer.

(100) Nakajima, A., K. Hashimoto, and T. Watanabe, Recent studies on super-hydrophobic films. Monatshefte für Chemie/Chemical Monthly, 2001. 132(1): p. 31-41.

(101) Feng, L., et al., Super‐hydrophobic surfaces: from natural to artificial. Advanced materials, 2002. 14(24): p. 1857-1860.

(102) Feng, L., et al., Super‐hydrophobic surface of aligned polyacrylonitrile nanofibers. Angewandte Chemie, 2002. 114(7): p. 1269-1271.

(103) Guo, Z., et al., Stable biomimetic super-hydrophobic engineering materials. Journal of the American Chemical Society, 2005. 127(45): p. 15670-15671.

(104) Hoult, D.P., Oil spreading on the sea. Annual Review of Fluid Mechanics, 1972. 4(1): p. 341-368.

(105) Langmuir, I., Oil lenses on water and the nature of monomolecular expanded films. Journal of Chemical Physics, 1933. 1(11): p. 756-776.

(106) Burton, J.C., et al., Experimental and Numerical Investigation of the Equilibrium Geometry of Liquid Lenses. Langmuir, 2010. 26(19): p. 15316-15324.

(107) David, R., et al., Investigation of the Neumann triangle for dodecane liquid lenses on water. Colloids and Surfaces a-Physicochemical and Engineering Aspects, 2009. 333(1-3): p. 12-18.

(108) Thiele, U., et al., Modelling approaches to the dewetting of evaporating thin films

of nanoparticle suspensions. Journal of Physics: Condensed Matter, 2009. 21(26): p. 264016.

(109) Wyart, F.B. and J. Daillant, Drying of solids wetted by thin liquid films. Canadian Journal of Physics, 1990. 68(9): p. 1084-1088.

(110) Jacobs, K., S. Herminghaus, and K.R. Mecke, Thin liquid polymer films rupture via defects. Langmuir, 1998. 14(4): p. 965-969.

(111) Stange, T., D. Evans, and W. Hendrickson, Nucleation and growth of defects leading to dewetting of thin polymer films. Langmuir, 1997. 13(16): p. 4459-4465.

(112) Reiter, G., Dewetting of thin polymer films. Physical Review Letters, 1992. 68(1): p. 75.

(113) Xie, R., et al., Spinodal dewetting of thin polymer films. Physical Review Letters, 1998. 81(6): p. 1251.

(114) Redon, C., F. Brochard-Wyart, and F. Rondelez, Dynamics of dewetting. Physical review letters, 1991. 66(6): p. 715.

(115) Gu, X., et al., Hole‐growth instability in the dewetting of evaporating polymer solution films. Journal of Polymer Science Part B: Polymer Physics, 2002. 40(24): p. 2825-2832.

(116) Ge, G. and L. Brus, Evidence for spinodal phase separation in two-dimensional nanocrystal self-assembly. The Journal of Physical Chemistry B, 2000. 104(41): p. 9573-9575.

(117) Maillard, M., et al., Rings and hexagons made of nanocrystals: a Marangoni effect. The Journal of Physical Chemistry B, 2000. 104(50): p. 11871-11877.

(118) Zhang, L., et al., Evaporative self-assembly from complex DNA-colloid

suspensions. Langmuir, 2008. 24(8): p. 3911-3917.

(119) Karthaus, O., et al., Formation of ordered mesoscopic polymer arrays by dewetting. Chaos: An Interdisciplinary Journal of Nonlinear Science, 1999. 9(2): p. 308-314.

(120) Vancea, I., et al., Front instabilities in evaporatively dewetting nanofluids. Physical Review E, 2008. 78(4): p. 041601.

(121) Stannard, A., et al., Dual-scale pattern formation in nanoparticle assemblies. The Journal of Physical Chemistry C, 2008. 112(39): p. 15195-15203.

(122) Pauliac-Vaujour, E., et al., Fingering instabilities in dewetting nanofluids. Physical review letters, 2008. 100(17): p. 176102.

(123) Zhang, C., X. Zhu, and L. Zhou, Morphology tunable pinning force and evaporation modes of water droplets on PDMS spherical cap micron-arrays. Chemical Physics Letters, 2011. 508(1-3): p. 134-138.

(124) Birdi, K., D. Vu, and A. Winter, A study of the evaporation rates of small water drops placed on a solid surface. The Journal of physical chemistry, 1989. 93(9): p. 3702-3703.

(125) Cui, L.-F., et al., Crystalline-amorphous core− shell silicon nanowires for high capacity and high current battery electrodes. Nano Letters, 2008. 9(1): p. 491-495.

(126) McHale, G., et al., Analysis of droplet evaporation on a superhydrophobic surface. Langmuir, 2005. 21(24): p. 11053-11060.

(127) Liu, C.J., E. Bonaccurso, and H.J. Butt, Evaporation of sessile water/ethanol drops in a controlled environment. Physical Chemistry Chemical Physics, 2008. 10(47): p. 7150-7157.

(128) Shi, L.X., et al., Wetting and evaporation behaviors of water-ethanol sessile drops

on PTFE surfaces. Surface and Interface Analysis, 2009. 41(12-13): p. 951-955.

(129) Picknett, R.G. and R. Bexon, EVAPORATION OF SESSILE OR PENDANT DROPS IN STILL AIR. Journal of Colloid and Interface Science, 1977. 61(2): p. 336-350.

(130) Zhang, W.B., et al., Ring formation from a drying sessile colloidal droplet. Aip Advances, 2013. 3(10).

(131) Stauber, J., et al., Strathprints Institutional Repository. J. Fluid Mech, 2014. 744: p. R2.

(132) Yang, S.M., et al., Nanomachining by colloidal lithography. Small, 2006. 2(4): p. 458-475.

(133) Chen, T., et al., Colloidal lithography for fabricating patterned polymer-brush microstructures. Beilstein Journal of Nanotechnology, 2012. 3: p. 397-403.

(134) Lin, C.C., F.Q. Yang, and S. Lee, Surface Wrinkling of an Elastic Film: Effect of Residual Surface Stress. Langmuir, 2008. 24(23): p. 13627-13631.

(135) Buckingham, E., On physically similar systems, illustrations of the use of dimensional equations. Physical Review, 1914. 4(4): p. 345-376.

(136) Taylor, G., The Instability of Liquid Surfaces When Accelerated in a Direction Perpendicular to Their Planes .1. Proceedings of the Royal Society of London Series a-Mathematical and Physical Sciences, 1950. 201(1065): p. 192-196.

(137) Rayleigh, L., Investigation of the character of the equilibrium of an incompressible heavy fluid of variable density Proc. Lond. Math. Soc., 1883 14: p. 170-177

(138) de Gennes, P.-G., F. Brochard-Wyart, and D. Quere, Capillary and wetting phenomena, Springer, New York, 2010.

(139) Tanaka, H., Viscoelastic phase separation. Journal of Physics: Condensed Matter, 2000. 12(15): p. R207.

(140) Fruhner, H. and K.-D. Wantke, A new instrument for measuring the viscoelastic properties of dilute polymer solutions. Colloid and Polymer Science, 1996. 274(6): p. 576-581.

(141) Takahashi, Y., et al., Viscoelastic properties of polyelectrolyte solutions. III. Dynamic moduli from terminal to plateau regions. Journal of non-crystalline solids, 1994. 172: p. 911-916.

(142) Abdessamad, Z., et al., Homogenization of thermo-viscoelastic Kelvin–Voigt model. Comptes Rendus Mécanique, 2007. 335(8): p. 423-429.

(143) Hekmat, D., et al., Modeling of transient flow through a viscoelastic preparative chromatography packing. Biotechnology progress, 2013. 29(4): p. 958-967.

(144) Bajpai, S., et al., Semidiscrete Galerkin method for equations of motion arising in Kelvin‐Voigt model of viscoelastic fluid flow. Numerical Methods for Partial Differential Equations, 2013. 29(3): p. 857-883.

(145) Wei, Z. and N. Simizu, Damping Properties of the Viscoelastic Material Described by Fractional Kelvin-Voigt Model. JSME International Journal Series C, 1999. 42(1): p. 1-9.

(146) Falconnet, D., et al., A novel approach to produce protein nanopatterns by combining nanoimprint lithography and molecular self-assembly. Nano Letters, 2004. 4(10): p. 1909-1914.

(147) Tsujioka, T., Metal-vapor deposition modulation on polymer surfaces prepared by the coffee-ring effect. Soft Matter, 2013.

(148) Maki, K.L. and S. Kumar, Fast Evaporation of Spreading Droplets of Colloidal Suspensions. Langmuir, 2011. 27(18): p. 11347-11363.

(149) De Gans, B.-J. and U.S. Schubert, Inkjet printing of well-defined polymer dots and arrays. Langmuir, 2004. 20(18): p. 7789-7793.

(150) Han, W., et al., A Simple Route to Hierarchically Assembled Micelles and Inorganic Nanoparticles. Angewandte Chemie, 2012. 124(50): p. 12756-12760.

(151) Li, B., et al., Macroscopic Highly Aligned DNA Nanowires Created by Controlled Evaporative Self-Assembly. ACS nano, 2013. 7(5): p. 4326-4333.

(152) Sun, W. and F. Yang, Evaporation-induced formation of self-organized gradient concentric rings on sub-micron pre-cast PMMA films. Soft Matter, 2014.

(153) Yu, Y.-S. and Y.-P. Zhao, Elastic deformation of soft membrane with finite thickness induced by a sessile liquid droplet. Journal of colloid and interface science, 2009. 339(2): p. 489-494.

(154) Yu, Y.-S., Z.-Q. Wang, and Y.-P. Zhao, Experimental study of evaporation of sessile water droplet on PDMS surfaces. Acta Mechanica Sinica, 2013. 29(6): p. 799-805.

(155) Yu, Y.-S. and Y.-P. Zhao, Deformation of PDMS membrane and microcantilever by a water droplet: Comparison between Mooney–Rivlin and linear elastic constitutive models. Journal of colloid and interface science, 2009. 332(2): p. 467-476.

(156) Pericet-Camara, R., et al., Solid-supported thin elastomer films deformed by microdrops. Soft Matter, 2009. 5(19): p. 3611-3617.

(157) Taylor, G., The instability of liquid surfaces when accelerated in a direction perpendicular to their planes. I. Proceedings of the Royal Society of London. Series A. Mathematical and Physical Sciences, 1950. 201(1065): p. 192-196.

(158) de Gans, B.J. and U.S. Schubert, Inkjet printing of well-defined polymer dots and arrays. Langmuir, 2004. 20(18): p. 7789-7793.

(159) Orejon, D., K. Sefiane, and M.E.R. Shanahan, Evaporation of nanofluid droplets with applied DC potential. Journal of Colloid and Interface Science, 2013. 407: p. 29-38.

(160) Xia, D. and S. Brueck, Strongly anisotropic wetting on one-dimensional nanopatterned surfaces. Nano letters, 2008. 8(9): p. 2819-2824.

(161) Cordeiro, R.M. and T. Pakula, Behavior of evaporating droplets at nonsoluble and soluble surfaces: Modeling with molecular resolution. The Journal of Physical Chemistry B, 2005. 109(9): p. 4152-4161.

(162) Li, G., H.-J. Butt, and K. Graf, Microstructures by solvent drop evaporation on polymer surfaces: Dependence on molar mass. Langmuir, 2006. 22(26): p. 11395-11399.

(163) Li, G. and K. Graf, Microstructures formation by deposition of toluene drops on polystyrene surface. Physical Chemistry Chemical Physics, 2009. 11(33): p. 7137-7144.

(164) Li, G., et al., Evaporation structures of solvent drops evaporating from polymer surfaces: Influence of molar mass. Macromolecular Chemistry and Physics, 2007. 208(19‐20): p. 2134-2144.

(165) Muralidhar, P., et al., Fast dynamic wetting of polymer surfaces by miscible and immiscible liquids. Colloid and polymer science, 2011. 289(14): p. 1609-1615.

(166) Lopes, M.C. and E. Bonaccurso, Evaporation control of sessile water drops by soft viscoelastic surfaces. Soft Matter, 2012. 8(30): p. 7875-7881.

(167) Lee, K.-H., et al., Spontaneous nanoscale polymer solution patterning using solvent evaporation driven double-dewetting edge lithography. Soft Matter, 2012. 8(2): p. 465-471.

(168) Yabu, H., et al., Superhydrophobic and lipophobic properties of self-organized honeycomb and pincushion structures. Langmuir, 2005. 21(8): p. 3235-3237.

(169) Li, Y.-F., Y.-J. Sheng, and H.-K. Tsao, Solute concentration-dependent contact angle hysteresis and evaporation stains. Langmuir, 2014. 30(26): p. 7716-7723.

(170) Hong, S.W., J. Xia, and Z. Lin, Spontaneous formation of mesoscale polymer patterns in an evaporating bound solution. Advanced Materials, 2007. 19(10): p. 1413-1417.

(171) Bao, R., et al., Large‐Scale Controllable Patterning Growth of Aligned Organic Nanowires through Evaporation‐Induced Self‐Assembly. Chemistry-A European Journal, 2012. 18(3): p. 975-980.

(172) Olgun, U. and V. Sevínç, Evaporation induced self-assembly of zeolite A micropatterns due to the stick–slip dynamics of contact line. Powder Technology, 2008. 183(2): p. 207-212.

(173) Sun, W. and F. Yang, Self-organization of unconventional gradient concentric rings on precast PMMA films. The Journal of Physical Chemistry C, 2014. 118(19): p. 10177-10182.

(174) Bodiguel, H., F. Doumenc, and B. Guerrier, Stick-Slip Patterning at Low Capillary Numbers for an Evaporating Colloidal Suspension. Langmuir, 2010. 26(13): p. 10758-10763.

(175) Xu, J., et al., Self-assembly of gradient concentric rings via solvent evaporation

from a capillary bridge. Physical review letters, 2006. 96(6): p. 066104.

(176) Huggins, M.L., The viscosity of dilute solutions of long-chain molecules. IV. Dependence on concentration. Journal of the American Chemical Society, 1942. 64(11): p. 2716-2718.

(177) Sun, W. and F. Yang, Evaporation-induced formation of self-organized gradient concentric rings on sub-micron pre-cast PMMA films. Soft matter, 2014. 10(25): p. 4451-4457.

(178) Yoshitake, Y., et al., Structure of Circulation Flows in Polymer Solution Droplets Receding on Flat Surfaces. Langmuir, 2010. 26(6): p. 3923-3928.

(179) Hu, H. and R.G. Larson, Analysis of the effects of Marangoni stresses on the microflow in an evaporating sessile droplet. Langmuir, 2005. 21(9): p. 3972-3980.

(180) De Gennes, P.-G., *Scaling concepts in polymer physics*. 1979: Cornell university press.

(181) Edward, J.T., Molecular volumes and the Stokes-Einstein equation. Journal of Chemical Education, 1970. 47(4): p. 261.

(182) Santos, F.J., et al., Standard reference data for the viscosity of toluene. Journal of physical and chemical reference data, 2006. 35(1): p. 1-8.

(183) Berteloot, G., et al., Evaporation of a sessile droplet: Inside the coffee stain. Journal of Colloid and Interface Science, 2012. 370: p. 155-161.

(184) Lin, Y., et al., Self‐Assembly of Rodlike Bio‐nanoparticles in Capillary Tubes. Angewandte Chemie International Edition, 2010. 49(5): p. 868-872.

(185) Sun, W. and F.Q. Yang, Evaporation-induced formation of self-organized gradient concentric rings on sub-micron pre-cast PMMA films. Soft Matter, 2014.

DOI:10.1039/C4SM00245H.

(186) Sun, W. and F.Q. Yang, Self-Organization of Unconventional Gradient Concentric Rings on Precast PMMA Films. Journal of Physical Chemistry C, 2014. DOI: 10.1021/jp502304m.

(187) Sun, W. and F.Q. Yang, Formation of Self-Organized Gradient Stripes on Precast Poly(methylmethacrylate) Films. Langmuir, 2014. 30(22): p. 6548–6555.

(188) Lambooy, P., et al., Dewetting at the liquid-liquid interface. Physical Review Letters, 1996. 76(7): p. 1110.

(189) Sun, W. and F.Q. Yang, Evaporation-induced formation of self-organized gradient concentric rings on sub-micron pre-cast PMMA films. Soft Matter, 2014. 10(25): p. 4451-4457.

(190) Yabu, H. and M. Shimomura, Preparation of Self‐Organized Mesoscale Polymer Patterns on a Solid Substrate: Continuous Pattern Formation from a Receding Meniscus. Advanced Functional Materials, 2005. 15(4): p. 575-581.

(191) Sun, W. and F. Yang, Formation of Self-Organized Gradient Stripes on Precast Poly (methyl methacrylate) Films. Langmuir, 2014. 30(22): p. 6548-6555.

(192) Karthaus, O., et al., Mesoscopic 2-D ordering of inorganic/organic hybrid materials. Materials Science and Engineering: C, 1999. 10(1): p. 103-106.

(193) Srinivasarao, M., et al., Three-Dimensionally Ordered Array of Air Bubbles in a Polymer Film. Science, 2001. 292(5514): p. 79-83.

(194) Peng, J., et al., The influencing factors on the macroporous formation in polymer films by water droplet templating. Polymer, 2004. 45(2): p. 447-452.

(195) Li, J., et al., Highly ordered microporous films containing a polyolefin segment

fabricated by the breath-figure method using well-defined polymethylene-b-polystyrene copolymers. Polymer Chemistry, 2010. 1(2): p. 164-167.

(196) Maruyama, N., et al., Mesoscopic patterns of molecular aggregates on solid substrates. Thin Solid Films, 1998. 327–329(0): p. 854-856.

(197) Sun, W. and F.Q. Yang, Self-Organization of Unconventional Gradient Concentric Rings on Precast PMMA Films. Journal of Physical Chemistry C, 2014. 118(19): p. 10177-10182.

(198) Thomas, E.L., et al., Ordered packing arrangements of spherical micelles of diblock copolymers in two and three dimensions. Macromolecules, 1987. 20(11): p. 2934-2939.

(199) Sun, W. and F.Q. Yang, Formation of Self-Organized Gradient Stripes on Precast Poly(methyl methacrylate) Films. Langmuir, 2014. 30(22): p. 6548-6555.

(200) Rayleigh, L., Breath figures. Nature, 1911. 86(2169): p. 416-417.

(201) Kaptay, G., The Gibbs Equation versus the Kelvin and the Gibbs-Thomson Equations to Describe Nucleation and Equilibrium of Nano-Materials. Journal of Nanoscience and Nanotechnology, 2012. 12(3): p. 2625-2633.

(202) Beysens, D., et al., How does dew form? Phase Transitions: A Multinational Journal, 1991. 31(1-4): p. 219-246.

(203) Sun, W. and F. Yang, Dynamics of the evaporative dewetting of a volatile liquid film confined within a circular ring. Langmuir, 2015.

(204) Gabriele, S., et al., Viscoelastic dewetting of constrained polymer thin films. Journal of Polymer Science Part B: Polymer Physics, 2006. 44(20): p. 3022-3030.

(205) Picknett, R. and R. Bexon, The evaporation of sessile or pendant drops in still air.

Journal of Colloid and Interface Science, 1977. 61(2): p. 336-350.

(206) Chen, Y.-J., et al., Quasi-logarithmic spacing law in dewetting patterns from the drying meniscus of a polymer solution. Chemical Physics Letters, 2012. 529: p. 74-78.

(207) Frastia, L., A.J. Archer, and U. Thiele, Dynamical model for the formation of patterned deposits at receding contact lines. Physical review letters, 2011. 106(7): p. 077801.

(208) Kostourou, K., et al., Interface morphologies in liquid/liquid dewetting. Chemical Engineering and Processing: Process Intensification, 2011. 50(5): p. 531-536.

(209) Bommer, S., et al., Droplets on liquids and their journey into equilibrium. Eur. Phys. J. E, 2013. 36: p. 87.

(210) Xu, L., A. Sharma, and S.W. Joo, Dewetting of Stable Thin Polymer Films Induced by a Poor Solvent: Role of Polar Interactions. Macromolecules, 2012. 45(16): p. 6628-6633.

(211) Cox, R.G., The Dynamics of the Spreading of Liquids on a Solid-Surface .1. Viscous-Flow. Journal of Fluid Mechanics, 1986. 168: p. 169-194.

(212) Huh, C. and L.E. Scriven, Hydrodynamic Model of Steady Movement of a Solid/Liquid/Fluid Contact Line. Journal of Colloid and Interface Science, 1971. 35(1): p. 85-&.

(213) Cherry, B.W. and C.M. Holmes, Kinetics of Wetting of Surfaces by Polymers. Journal of Colloid and Interface Science, 1969. 29(1): p. 174-&.

(214) Blake, T.D. and J.M. Haynes, Kinetics of Liquid/Liquid Displacement. Journal of Colloid and Interface Science, 1969. 30(3): p. 421-&.

(215) Ruckenstein, E. and C.S. Dunn, Slip Velocity during Wetting of Solids. Journal of Colloid and Interface Science, 1977. 59(1): p. 135-138.

(216) Wang, F.C. and Y.P. Zhao, Slip boundary conditions based on molecular kinetic theory: The critical shear stress and the energy dissipation at the liquid-solid interface. Soft Matter, 2011. 7(18): p. 8628-8634.

(217) Ramiasa, M., et al., Contact Line Friction in Liquid-Liquid Displacement on Hydrophobic Surfaces. Journal of Physical Chemistry C, 2011. 115(50): p. 24975-24986.

(218) Vashishtha, S.R., N. Chand, and S.A.R. Hashmi, Morphology of PS/PMMA blends and their solution rheology. Indian Journal of Chemical Technology, 2002. 9(4): p. 316-323.

Vita

Wei Sun was born in the city of Fushun, Liaoning Province, P. R. China.

Education

Master, Materials Science and Engineering, Shanghai Jiao tong University, Shanghai, 2012

Bachelor, Polymer Science and Engineering, Jiangnan University, Wuxi, 2009

Publication

(1) **Wei Sun** and Fuqian Yang, Cooling-induced formation of honeycomb patterns on pre-cast PMMA films at low temperatures, *RSC Advances*, 2015, DOI: 10.1039/C5RA09579D

(2) **Wei Sun** and Fuqian Yang, Dynamics of the evaporative dewetting of a volatile liquid film confined within a circular ring, *Langmuir* 31 (2015) 4024-4031

(3) **Wei Sun** and Fuqian Yang, Fabrication of asymmetric-gradient-concentric ring patterns via evaporation of droplets of PMMA solution at different substrate temperatures, *RSC Advances* 5 (2015) 29850-29858

(4) **Wei Sun**, Kathleen Yang, Fuqian Yang, Formation of self-organized surface structures on poly(methyl methacrylate) films: effect of two contacting metallic wires, *Journal of Polymer Research* 22(2015) 90: DOI10.1007/s10965-015-0739-x

(5) **Wei Sun** and Fuqian Yang, Formation of well-ordered finger-like structures on pre-cast thin films, *RSC Advances* 4 (2014) 45535 - 45539

(6) **Wei Sun**, and Fuqian Yang. "Evaporation-induced formation of self-organized gradient concentric rings on sub-micron pre-cast PMMA films." *Soft matter*10.25

(2014): 4451-4457.

(7) **Wei Sun**, and Fuqian Yang. "Formation of self-organized gradient stripes on pre-cast poly (methyl methacrylate) films." *Langmuir* 30 (22) (2014): 6548–6555.

(8) **Wei Sun,** and Fuqian Yang. "Self-organization of Unconventional Gradient Concentric Rings on Pre-cast PMMA Films." *The Journal of Physical Chemistry C* 118 (19) (2014): 10177–10182.

(9) Wang, Yao, Wenli Zhang, Jixi Zhang, **Wei Sun**, Ruiyan Zhang and Hongchen Gu "Fabrication of a novel polymer-free nanostructured drug-eluting coating for cardiovascular stents." *ACS applied materials & interfaces*5.20 (2013): 10337-10345.

(10) Qian Liu, Jixi Zhang, **Wei Sun**, Qian R. Xie, Hongchen Gu and Weiliang Xia, Delivering Hydrophilic and Hydrophobic Chemotherapeutics Simultaneously by Mesoporous Silica Nanoparticles to Inhibit Cancer Cells. *International journal of nanomedicine*,, 7 (2012): 999

(11) Jixi Zhang, **Wei Sun**, Lotta Bergman, Jessica M. Rosenholm, Mika Linden, Guojun Wu, Hong Xu, Hong-chen Gu, Magnetic mesoporous silica nanospheres as DNA/drug carrier. *Materials Letters*, 67.1 (2012): 379-382.

(12) Jessica M. Rosenholm, Jixi Zhang, **Wei Sun**, Hongchen Gu, Large-pore mesoporous silica-coated magnetite core-shell nanocomposites and their relevance for biomedical application. *Microporous and Mesoporous Materials*, 145.1 (2011): 14-20.

Conference Presentations:

(1) **Wei Sun** and Fuqian Yang, Thin Film Block Copolymer Self-Assembly and Morphology, AIChE Annual Meeting 2014, Atlanta, November 2014

(2) **Wei Sun,** Stephen Lipka, and Fuqian Yang, Oral presentation: Activated Carbon Derived from Hemp and Its Use in Electrochemical Capacitors, ECS meeting 2015, Phoenix City, October 2015

Professional Affiliations

Student Member in AICHE, 2014 – present